ALMA MATER STUDIORUM
UNIVERSITA' DI BOLOGNA

SCHOOL OF ENGINEERING AND ARCHITECTURE
- Forlì Campus -

SECOND CYCLE MASTER'S DEGREE in
INGEGNERIA AEROSPAZIALE/ AEROSPACE ENGINEERING
Class LM-20

GRADUATION THESIS
In Aerospace Structures

Modelling of Pencil-Lead Break Acoustic Emission Sources using the Time Reversal Technique

CANDIDATE
Francesco Falcetelli

SUPERVISOR
Professor *Enrico Troiani*

CO-SUPERVISOR
Professor *Marcias Martinez*

Academic Year 2017/2018

ABSTRACT

In Acoustic Emissions (AE), Hsu-Nielsen Pencil-Lead Breaks (PLB) are used to generate sound waves enabling the characterization of acoustic wave speed in complex structures. The broadband signal of a PLB represents a repeatable emission, which can be applied at different regions of the structure, and therefore can be used to calibrate the localization algorithms of the AE system. In recent years, the use of Finite Element Method (FEM) has flourished for modelling acoustic Lamb wave propagation, which is present in thin plate-like structures. The primary challenge faced by the AE community is the lack of a well-known mathematical function of a PLB signal that can be applied in numerical simulations. This study makes use of a Time Reversal (TR) approach to identify the emission source of the PLB on a 7075-T651 aluminum plate. An ABAQUS CAE™ model with piezoelectric actuators and sensors was developed. In order to avoid edge reflections, absorbing boundaries based on the Stiffness Reduction Method (SRM) were considered. The captured PLB signals were used as input to the FEM and was time-reversed. Furthermore, a band-limited white noise signal was used to calibrate the contribution of the broadband frequencies found in the transmitted wave packet. Preliminary results indicate that the TR approach can be used to understand the shape and function of the original transmitted signal.

ACKNOWLEDGMENTS

I would first like to thank my supervisor Professor Troiani of the University of Bologna for giving me the possibility to do my thesis abroad in the United States. He encouraged me in this challenge putting me in contact with his colleagues at Clarkson University.

A special thank goes to Professor Martinez of Clarkson University. He has been more than a co-supervisor for me. He was always present from the first day when he came to pick me up at the Syracuse airport to the last one at Clarkson University. His door was always open whenever I ran into a trouble spot or had a question about my research project. He was really demanding with me and was hard to complete all the tasks assigned, but, at the same time he was a guide and a true friend. I owe him a lot and this thesis would not have been possible without his precious support.

I would like to thank Dott. Alessandro Baldassarre and for being such kind with me for all the period I spent in the US. We were lab mates at the university and good friends outside. He introduced me to his friends and his wonderful family helping me every time I needed.

My gratitude goes to my parents who always helped me and were there when I needed. They always tried to give me the maximum they could to make me realize my dreams.

I would like to thank also my lovely girlfriend. It has been a hard decision to leave her for such a long time, but she encouraged me not giving up in the though moments.

Finally, I would like to thank my grandmother. She passed away during those six months I was overseas, and she will not see me graduating. She always supported me before every exam I took and will be in my heart forever.

ABBREVIATIONS

AE – Acoustic Emission

NRB – Non-Reflective Boundaries

PLB – Pencil Lead Break

RMSS – Status variable corresponding to the root-mean square value of the noise

SHM – Structural Health Monitoring

STR - Signal-to-Threshold Ratio

TNR – Threshold-to-Noise Ratio

TOA – Time of Arrival

LUCY – Localization Uncertainty algorithm

ALID – Absorbing Layers using Increasing Damping

SRM – Stiffness Reduction Method

BLWN – Band-Limited White Noise

GLW – Guided Lamb Waves

NDE – Non-Destructive Evaluation

FREQUENTLY USED SYMBOLS

A_0 – Antisymmetric Lamb wave mode

S_0 – Symmetric Lamb wave mode

c_g – Group velocity

c_p – P-Wave velocity (longitudinal)

c_{ph} – Phase velocity

c_s – S-Wave velocity (shear)

λ – Wavelength

E – Young's Modulus

d – Plate thickness

ρ – Density

α – Proportional mass damping coefficient

β – Proportional stiffness damping coefficient

TABLE OF CONTENTS

LIST OF FIGURES

LIST OF TABLES

CHAPTER 1

1 INTRODUCTION

1.1 THESIS OBJECTIVES AND RESEARCH QUESTIONS

A primary challenge in Acoustic Emission (AE), is its inability to inform the user the size of the damage. AE at present time is only able to provide the location of an emission captured by a series (minimum of 2) of sensors. However, the characteristic features generated by the acoustic wave do not provide any information about the damage size or type. In this thesis it is hypothesized that each emission contains a unique set of features, like a fingerprint, which reflect the type and size of damage being generated. As such, the main objective of this thesis is to determine the characteristic features produced by an original emission. Due to the complexity of the problem in question, a series of Hanning Windows with well characterized propagation behavior will be used in the development of a Finite Element Model. Further work will lead to the utilization of a Pencil Lead Break (PLB) signal to mimic the random behavior of a metal fatigue crack propagation. In order to achieve this goal, a computational and experimental techniques based on Time Reversal will be used. The final aim is to develop a methodology that would allow AE users to obtain a representative PLB signal (broadband) to be implemented in complex structures.

As such, the scientific question being addressed in this M.Sc. thesis is:

Is it possible to make use of Time Reversal in order to determine the original emission emanating from a Pencil Lead Break, a Broadband signal?

1.2 RESEARCH APPROACH

The main objective of this thesis is to answer the previously stated scientific question. As many research studies, the first step consisted in a deep literature review, concerning SHM in general and more specifically, GLW propagation. Referring to Figure 1, two main paths were followed simultaneously: the green one, representing the experimental setup, and the blue one related to the numerical modeling.

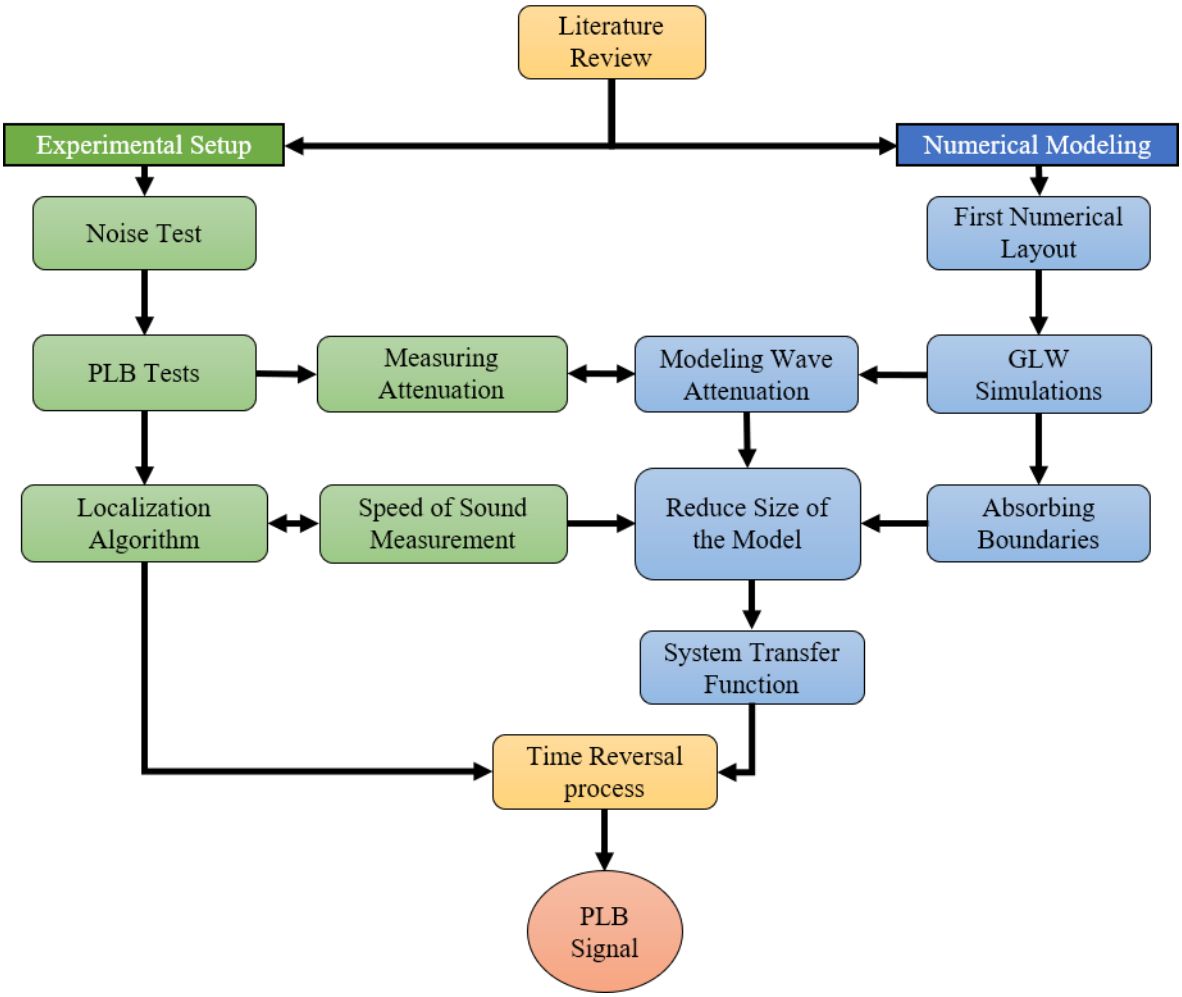

Figure 1 – Research approach

The experimental and computational activities in this study were strictly interconnected. For example, the first experimental data gave important insights and suggestions for the development of the numerical model. Then, the numerical model results highlighted important phenomena as wave reflections that were not considered in the first experimental setup. The interaction between the two approaches led to a successful model of wave attenuation, an ongoing challenge faced by the AE community. The development of a localization algorithm, crucial for many SHM applications, led to a more accurate assessment of the speed of the Lamb waves in the considered structure. Once the speed of the waves computation was refined, it automatically improved the performance of the localization algorithm and vice-versa. Those experimental achievements,

together with the development of absorbing boundaries, gave the possibility to build a reduced size model, in order to lessen the computational cost. Finally, a system transfer function was derived numerically and was used to apply, with a new methodology, the TR method. The previously mentioned localization algorithm, even if not directly used in this research step, can generalize this application for unknown source locations.

1.3 THESIS STRUCTURE

This thesis is subdivided in seven chapters and it is suggested to read them in the order they are presented.

In Chapter 1 the motivations of this study are presented together with the scientific question to be answered. Chapter 2 provides to the reader a background on Structural Heath Monitoring and a literature review with the main concepts regarding Guided Lamb Waves (GLW). If the reader is confident with the topics of SHM and GLW, it is also possible to skip this Chapter 2. The discussion continues in Chapter 3 where the experimental methodology is presented. Chapter 4 describes the development of a numerical model for the simulation of GLW. Chapter 5 starts with a short description of Time Reversal (TR) method. Followed by the description of a new methodology for the reconstruction of the broadband signals. In Chapter 6, the reconstruction of the Pencil Lead Break (PLB) signal is carried out exploiting the previously derived methodology. Chapter 7 discusses the obtained results leading to a series of interesting conclusions. Finally, potentially future research activity is also presented.

CHAPTER 2

2 LITERATURE REVIEW

2.1 STRUCTURAL HEALTH MONITORING

In recent years, technology is making great strides in many engineering applications leading to increasingly complex structures. The aerospace industry, driven by an increasing demand for mobility, is trying to manufacture increasingly lighter and safer structures to reduce fuel consumption (minimizing the costs) and keeping sufficiently high safety levels. Structural Health Monitoring (SHM) finds its natural place in this contest, where the capability to detect a damage as soon as possible is a crucial point. It seems worthwhile at this point to give a rigorous definition for SHM as:

"*The process of implementing a damage identification strategy for aerospace, civil and mechanical engineering infrastructure is referred to as structural health monitoring (SHM)*" [1].

A common SHM system develops in four main stages [2]:

I. Operational evaluation;
II. Data acquisition (or Sensing);
III. Feature extraction;
IV. Diagnosis and Prognosis.

In the first step, engineers have to determine what is worth to monitor and which is the best approach to achieve that result.

Data acquisition depends of course on the used technique. Depending on the case, the data acquisition system collects from the structure information of different nature (acceleration, velocity, displacement, vibration, and so on) and organize those data for the next step.

The third stage is feature extraction. Here, there is a multitude of different techniques, all with the same objective to extract damage related feature from the previously collected data. It is common

to start removing noise from the acquired signals before to apply whatever method (Fourier transform, Wavelet transform, etc.).

Finally, in the last phase engineers have to perform the diagnosis and the prognosis of the monitored structure, in order to assess the residual operational life. In the last decades, the aid of artificial intelligence techniques like Artificial neural networks, Support Vector Machine and many other similar methodologies, enhanced the capability to produce efficiently the right diagnosis and prognosis.

The main purpose of SHM is to evaluate continuously over time the state of a structure until the end of its operational life [3]. As previously stated, the full history database of the structure can be examined making it possible to provide, not only a diagnosis, but also a prognosis. Therefore, the time-dimension of monitoring allows to predict the damage evolution that is strictly connected with the residual useful life of the structure [4].

2.1.1 Historical background and motivations for SHM development

The evolution of design principles in the aerospace industry began in the early 1930s with the *safe-life* philosophy. Safety was guaranteed by replacing the aircraft components at the end of their design life. This approach assumes that there is not any crack growth due to a fatigue process during the operational life of the component. Over the years, the introduction of stronger alloys with poor fatigue properties combined with longer design lives, led to the two famous Comets accidents in 1954. The investigation of these crashes highlighted the limits of the *safe-life* approach and the need for new design principles.

Therefore, the *fail-safe* philosophy was introduced by aeronautical engineers in an attempt of replacing the concept of "safety by retirement" linked to the *safe-life* approach with the concept of "safety by design". With this new approach particular emphasis was posed in creating multiple load paths such that the failure of a main structural component does not compromise the flight safety. Service experience had shown that multiple site damage can occur, especially in aging aircrafts, making the use of a *fail-safe* philosophy inappropriate.

The *damage-tolerance* philosophy was adopted for the first time in 1978 [5] in response to the poor reliability of the fail-safe design principles evidenced by the Lusaka and the USAF F-111 accidents in the 1970's. Here, the fundamental principle is "safety by inspection" and can be considered a combination of the two previous approaches. The structure has to survive loads which

can generate fatigue crack growth up to the next scheduled inspection where potential damage is detected.

SHM aims to move a step forward, starting from the *damage-tolerance* approach. Behind the use of SHM there are remarkable safety and economic motivations. As an example, in the United States, the investments associated with the maintenance of plant facilities and equipment are estimated to be more than $200 billion each year. Regarding the aerospace industry, about a quarter of a commercial fleet's operating cost is related to repairs and maintenance [6]. It is clear and without any doubt that reducing the maintenance costs is an ongoing challenge of our time. SHM does not want to replace the *damage-tolerance* approach but simply to modify it, moving from the actual *time-based* maintenance to a *condition-based* maintenance [3]. The knowledge of the integrity of an aerospace or whatever structure in real time opens the possibility for engineers and manufacturers to exploit better the materials, reducing safety factors and at the same time increasing safety if a damage is detected before the scheduled inspection. Moreover, a reliable SHM system reduces the probability of a human error during the inspection phase leading to major safety.

2.1.2 SHM techniques

There are many different techniques within SHM. Many of them are similar to Non-Destructive Evaluation (NDE) methods, with the difference that the monitoring system in SHM is embedded within the structure or performed in-situ while in NDE this is not the case. The first important remark is that SHM techniques can be divided in two families: *passive* and *active* methods [4].

In the passive approach, the monitoring of the structure takes place by "listening" a change in a sensor signal induced by the damage being generated.

Acoustic Emissions (AE) is one of the most famous passive techniques. A mechanical failure in the material, or other kind of damage mechanisms, release energy in the structure under the form of elastic waves. Those waveforms are damage related and once recorded (for instance using piezoelectric transducers) can be used to provide relevant insights about the failure mechanism affecting the structure [7].

Another example of passive sensing type is a conductive paint technique. The main idea of this method is to print the sensor close to the expected damage location. Two layers of insulating and

conductive paint connected to a battery, are placed on the structure surface. Once the crack passes through those layers the circuit breaks leading to the information that a damage has occurred [8].
P. Cawley and R. D. Adams showed in [9] that the state of damage associated with a structure can be associated by the changing of physical parameters like a decrease in stiffness and a decrease in damping. Consequently, by analyzing the natural frequency changes of the structure under operational conditions is possible to assess the damage progression.
Moreover, it is possible to find a large use of fiber optics and strain gauges in the SHM community used as passive methods.
On the other hand, active approaches make use of both sensors and actuators. Hence, the structure is excited by the action of the actuators and its response is detected by the sensors. As such, a baseline of data representing the free-damage case is produced and then compared with the system response in presence of damage by means of a piezoelectric sensors network. A common SHM active technique is based on Guided Lamb waves (GLW). GLW are interesting from many points of views. They are elastic waves capable to travel for relatively long distances without losing a significant amount of amplitude, providing the user the possibility to monitor a wide area of the structure [10]. Moreover, they can be used both in active and passive SHM methodologies depending on the function that has been attributed to the piezoelectric sensors (actuators and sensors in the first case or just sensors in the latter).
In this study, the Time Reversal (TR) method will be discussed. This technique can be considered in between active and passive methodologies. Indeed, as typical of active methodologies, it uses piezoelectric sensors to generate input signals in the structure of interest, under the form of GLW. The waveforms are recorded, time reversed and sent back to the emitter, now behaving as an actuator. Then, the energy contained in the elastic waves refocus in the original source location. The TR method aims to compare the initial emitted signal with the reconstructed one trying to determine if any damage is present. Of course, in the case damage is present, the reconstructed signal will not match the sent one. Therefore, it can be considered also a passive method because, as Acoustic Emissions, it tries to create a free-damage baseline methodology. Moreover, TR can also be used to investigate the nature of unknown signals. For instance, in this thesis it is used to determine the characteristic emission generated by a PLB experiment.
Furthermore, the TR technique, being within the family of AE techniques, potentially allows to determine the damage location *a posteriori* as the waveforms refocus in the potential damage

location. Therefore, the knowledge of the damage position *a priori*, useful for many methods to place the sensors in the right place, here is not needed since can be derived applying the TR method itself.
The discussion continues giving to the reader a mathematical background about Lamb waves and more in general about elastic wave propagation in solid materials.

2.2 LAMB WAVES

This section aims to provide a basic background about Lamb waves propagation, hoping to lead to a clear understanding of the following chapters.

Sound waves in solids are, from a conceptual point of view, analogous to the well-known sound waves propagating in the atmosphere. Without going through the equations, it is possible to say that in both cases the problem is characterized by *longitudinal* waves propagating with a certain speed. The main difference is that solid materials can withstand shear forces, resulting in a second possible type of propagating waves, commonly called *transverse* waves. K. Worden in [11] summarizes three important properties of elastic waves propagating in an unbounded solid medium, also known as *bulk* waves:

i. The longitudinal and transverse waves do not interact with each other;
ii. They are non-dispersive, meaning that the propagation velocity is independent of the frequency;
iii. The geometry does not influence the propagation velocity that depends exclusively from the material properties.

The problem of elastic waves travelling in a solid material becomes more complex once a bounded medium is considered. A variety of different wave types can be generated depending on the considered geometry. In the case when only one side is bounded, elastic waves are referred to as *Rayleigh* waves, while if both sides are bounded (i.e. wave propagating in a plate, or a shell) elastic waves are referred to as *Lamb* waves.

Lamb waves take their name from Horace Lamb which was the first to discover those kinds of waves in 1917 in his famous work “On Waves in an Elastic Plate” [12]. They are also found in the literature under the name of *guided* waves in contrast with the aforementioned *bulk* waves. Those two waves families share the same set of partial differential equations despite of their important

differences. What makes the difference are the boundary conditions applied to the mathematical problem when dealing with guided waves. The necessity to satisfy those boundary conditions raises the difficulty of the problem, leading to extremely complex analytical solutions [13].

The derivation of the Lamb waves equations is out from the purposes of this thesis but can be found from the interested reader in reference [13]. Here, will be stated the governing equations associated with the propagation of guided waves in a plate which thickness is equal to $2h$, as depicted in Figure 2.

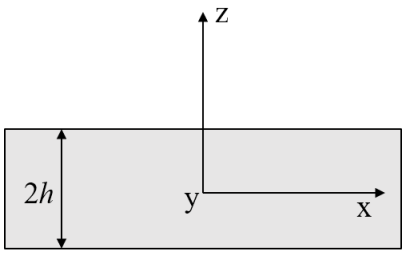

Figure 2 – Coordinate system related to Lamb waves propagating in a plate

It is possible to show that there are two kinds of solutions describing the propagation of Lamb waves: one in which the in-plane displacement is an even function and another where the in-plane displacement is an odd function. Those solutions are associated with the so-called *symmetric* and *antisymmetric* modes respectively [11]. Applying the boundary conditions (i.e. null value of the stress when $y = h$ or $y = -h$), it is possible to obtain the dispersion relations:

$$\frac{\tan(qh)}{\tan(ph)} = -\frac{4k^2pq}{(q^2-k^2)^2} \tag{2.1}$$

for the symmetric solution, and,

$$\frac{\tan(ph)}{\tan(qh)} = -\frac{4k^2pq}{(q^2-k^2)^2} \tag{2.2}$$

for the antisymmetric one, where,

$$p = -\frac{\omega}{\sqrt{({c_L}^2 - c^2)}}; \qquad q = -\frac{\omega}{\sqrt{({c_T}^2 - c^2)}} \tag{2.3}$$

As stated previously, h is half of the plate thickness. On the other hand, the wavenumber is denoted by k, the angular frequency with ω, while c_L and c_T represents the longitudinal and transverse wave velocities respectively for unbounded conditions [14]. Equations (2.1) and (2.2) show the link between the angular frequency and the associated possible velocities c related to the symmetric and the antisymmetric modes. More precisely, the velocity is linked to the so-called *frequency-thickness* product ωh. Therefore, those relationships have a physical meaning: Lamb waves, contrary to bulk waves, are strongly dispersive. Not surprisingly equations (2.1) and (2.2) are also referred as *dispersion* relations. Those equations can be solved only numerically and are transcendental, meaning that they can lead to many different real solutions which generate correspondingly different symmetric and antisymmetric modes. Plotting the dispersion relations, it is possible to obtain a graph like the one presented in Figure 3:

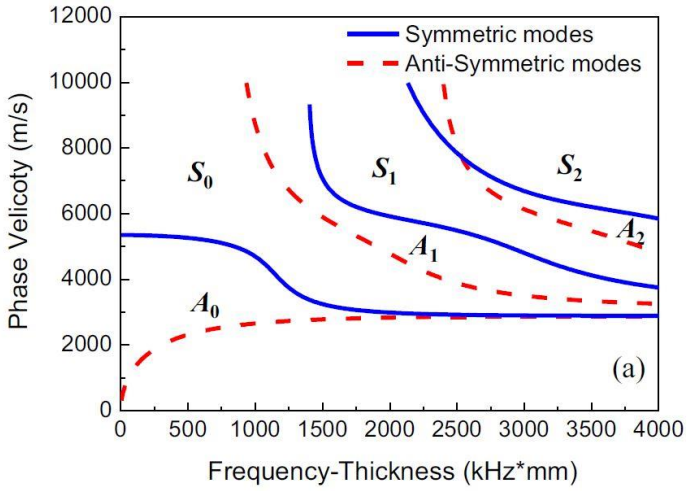

Figure 3 – Example of dispersion curves graph with phase velocities and frequency-thickness product [15]

The same kind of graph can be obtained plotting the group velocities of the different modes instead of the phase velocities. The group velocity c_g can be derived directly from the phase velocity c_p by simply exploiting the relation:

$$c_g = \frac{\partial \omega}{\partial k} \tag{2.4}$$

Indeed, the phase velocity c_p is linked to the wavenumber k and the angular frequency ω by the relation:

$$c_p = \frac{\omega}{k} \tag{2.5}$$

Thus, the corresponding dispersion plot is given by Figure 4:

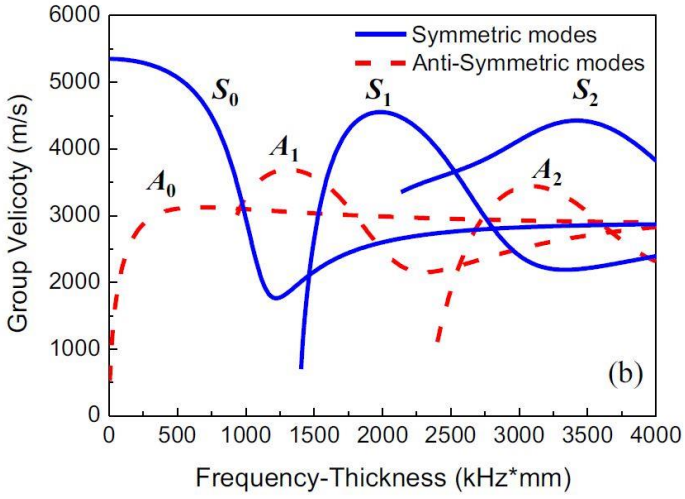

Figure 4 – Example of dispersion curves graph with group velocities and frequency-thickness product [15]

Often, the group velocity is taken as a reference because is what researchers are able to measure with piezoelectric sensors during experimental testing.

One may notice from the observation of Figure 3 and Figure 4 that below a certain value of the frequency-thickness product, only one symmetric and one antisymmetric mode are present. For this reason, particular interest is posed in the so-called *fundamental* modes, denoted commonly with S_0 and A_0, for the symmetric and antisymmetric modes respectively.

A schematic of these modes is represented in Figure 5.

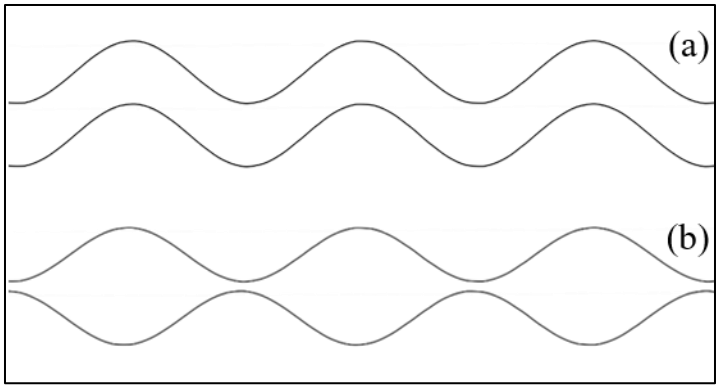

Figure 5 – Representation of the Antisymmetric (a) and Symmetric (b) Lamb waves modes

Figure 6 shows a preview of a numerical simulation carried out during the development of the numerical model (that will be discussed in Chapter 4), with a central frequency of the wave packets being equal to 50 kHz. The snapshot highlights the fundamental antisymmetric and symmetric modes, A_0 and S_0 respectively. Naturally, the displacements are exaggerated such that the two modes can be observed. In particular, the S_0 mode has typically a smaller amplitude with respect to the A_0 mode at 50 kHz, and this result is also confirmed by the authors in [16].

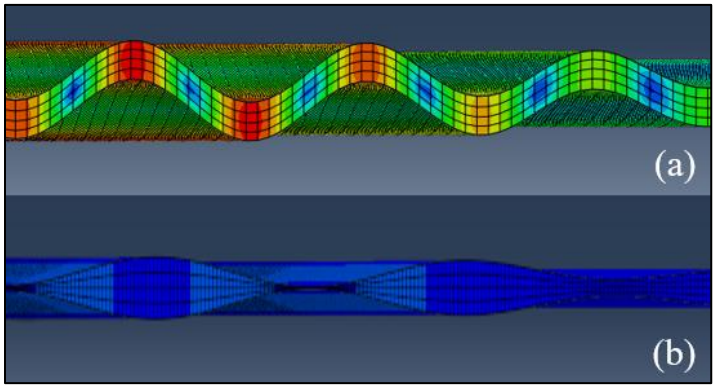

Figure 6 – Numerical results showing the Antisymmetric (a) and Symmetric (b) Lamb waves modes

CHAPTER 3

3 EXPERIMENTAL METHODOLOGY

In this chapter the methodology and performed experiments will be described. The obtained results will be used to develop and validate a numerical model, required for the application of the Time Reversal method, addressed in Chapter 5.

3.1 EXPERIMENTAL SETUP

The experiments were carried out at the Holistic Structural Integrity Process Laboratory at Clarkson University, NY, USA. The AE signals were analyzed by means of an AMSY-6 system, developed by Vallen Systeme GmbH™.

3.1.1 Hardware description

The AMSY-6 is an AE measurement system capable of processing information coming from several channels simultaneously. The measurement chain, representative of an AE channel, starts with a piezoelectric sensor that records an elastic wave at the surface of the monitored structure. The signal is transmitted through a preamplifier, which is connected to the ASIP-2 (double channel Acoustic Signal Processor). Finally, a USB connection transfers to the computer the AE features extracted by the ASIP-2. Moreover, the Vallen Systeme company provides several software to export the results in various formats and to further process the collected data.

Further specifications about the different AMSY-6 components are described in the following paragraphs.

3.1.1.1 Sensors and Preamplifiers

Figure 7 shows the first two elements of the AMSY-6 measurement chain. The VS900-M, represented in Figure 7 (a), is a piezoelectric sensor characterized by a broadband frequency response. It has a stainless-steel case and its weight is about 22 g. Since it does not support an integrated preamplifier, it is connected the AEP5H, shown in Figure 7 (b), in order to amplify the

signal. The AEP5H is a wide-band preamplifier with a gain that can be set to 34 dB or 40 dB by means of a switch located inside the preamplifier itself.

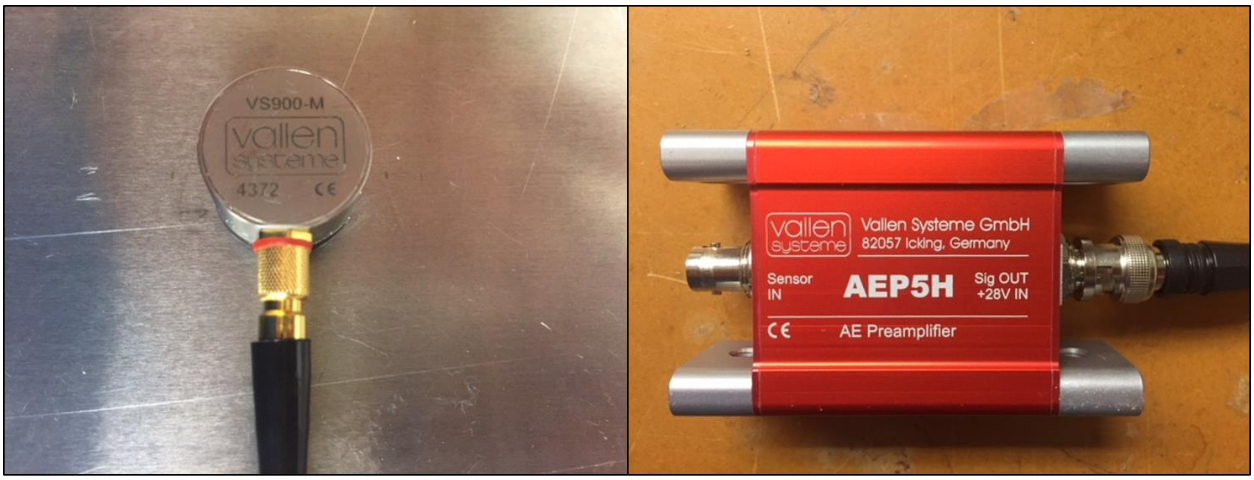

(a) (b)

Figure 7 – Piezoelectric sensor VS900-M, (a), and Preamplifier AEP5H, (b).

3.1.1.2 AE Signal Processor

Figure 8 shows the front view of the ASIP-2 together with the control panel, the parametric input channels. The MB6 chassis holds all the previously mentioned elements together, resulting in a compact configuration.

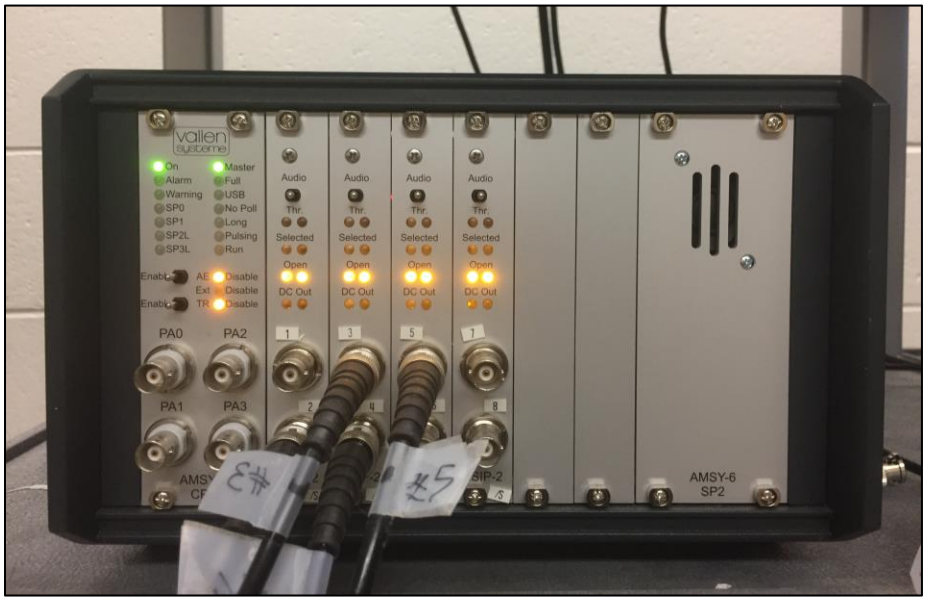

Figure 8 – Front view of the MB6 chassis containing the panel elements

3.1.2 Specimen and first sensor layout

A 7075-T651 aluminum plate, measuring 304.8 mm by 609.6 mm by 1.6 mm, was used in this study. According to the data sheet, the specimen density, ρ, and Young's Modulus, E, were 2810 kg/m^3 and 71.7 GPa respectively.

The material choice is justified by the fact that aluminum alloys are commonly used in aerospace structures. Moreover, it is an isotropic material, leading to circular propagating Lamb waves at the surface of the plate. In the literature, it is common to find Acoustic Emissions studies applied to anisotropic materials such as composites, but this increases the complexity of the problem. The changing of material properties with the direction leads to wave patterns of different shapes, that are difficult to model or to implement for a localization algorithm [17]. This thesis, which can be considered as the first part of a wider research project, tries to avoid unnecessary increments in complexity, without losing of generality.

Different sensor layouts will be used to accomplish different tasks. Table 1 gives the coordinates of the various piezoelectric transducers for this first part of the project. The sensor names were chosen arbitrarily, while the channels are numbered accordingly to their relative connection with the ASIP-2 board.

The corresponding layout configuration is represented in Figure 9, which shows also the origin of the used reference system.

Table 1 – Sensors coordinates for this initial experimental layout

General		Coordinates [mm]		Coordinates [in.]	
Sensor	Channel	X	Y	X	Y
1	1	152.4	304.8	6	12
2	2	76.2	457.2	3	18
3	3	228.6	406.4	9	16
4	4	228.6	152.4	9	6
5	5	76.2	203.2	3	8
6	8	152.4	549.7	6	21.6

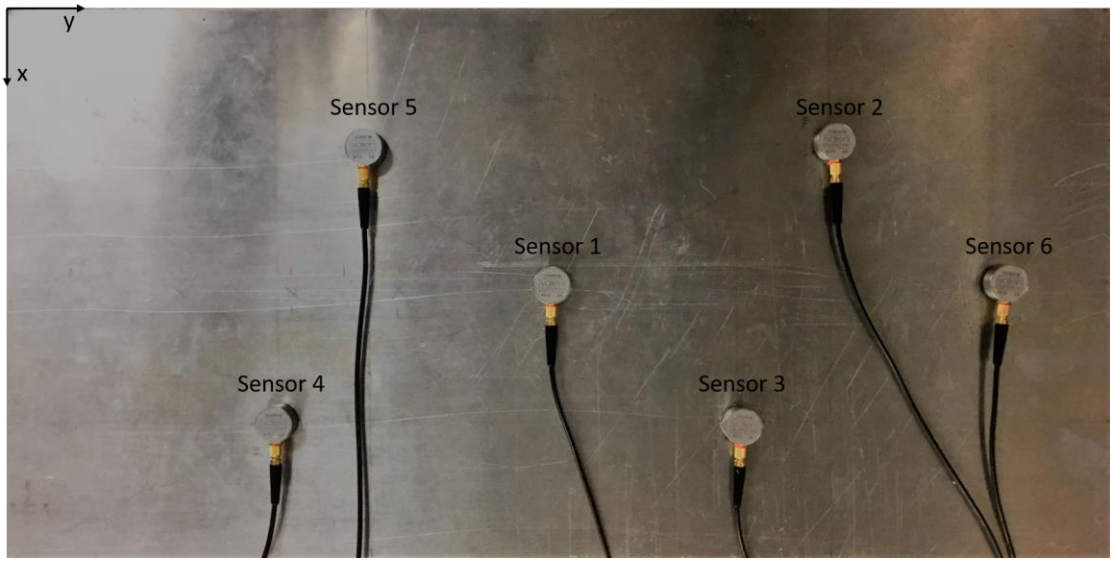

Figure 9 – First sensor configuration

3.2 NOISE TEST

Data acquisition is a crucial point to obtain accurate results. In particular, the selection of the proper threshold value allows the software to select the right time of arrival related to the AE. For this purpose, the noise level affecting the piezoelectric sensors has to be considered. A standard procedure to conduct a noise test is to set the detection threshold to a relatively low value and acquire data for a period of at least 5 minutes. Following this guideline, several noise tests have been performed with a threshold of 28.3 dB for each channel. The maximum peak amplitude recorded in the experiments was used as a reference in order to determine the proper threshold value as it is described by the following equation:

$$Th = N_{max} + X \tag{3.1}$$

Where Th is the detection threshold, N_{max} is the measured peak amplitude and X is a user defined parameter whose value has to be equal or greater than 6 dB.

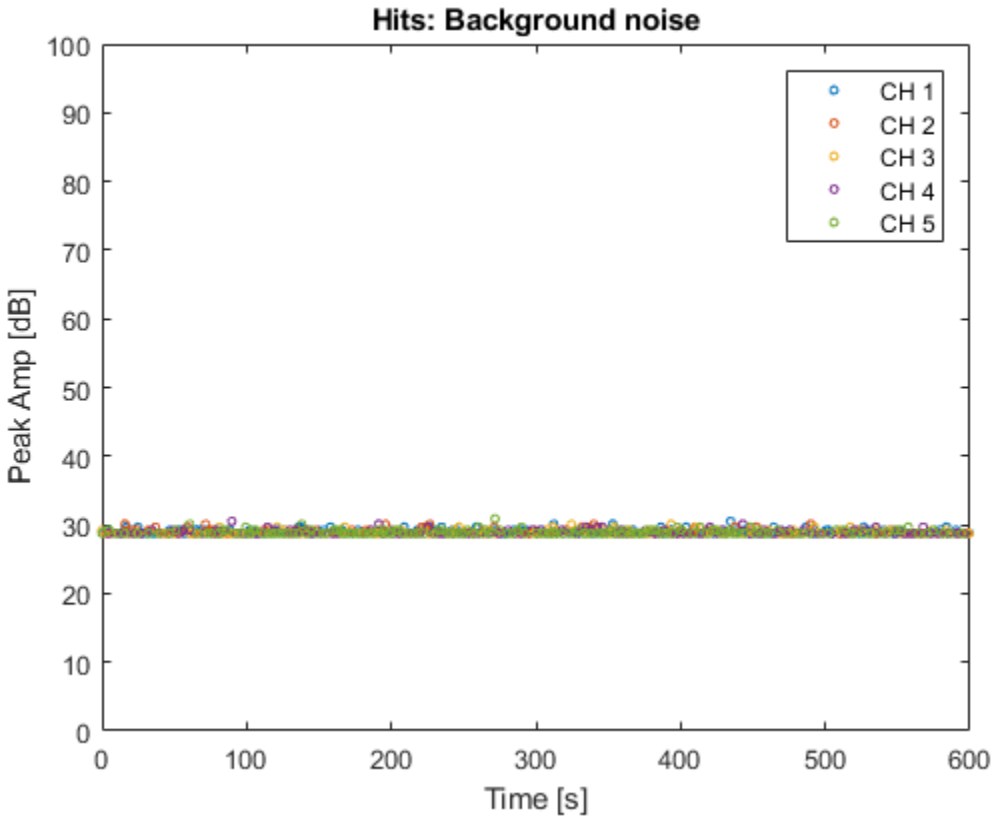

Figure 10 – Hits recorded in each channel over 10 minutes

The recorded hits in Figure 10 show a measured peak amplitude N_{max} slightly higher than 30 dB. Therefore, taking as a reference N_{max} and giving to X a value of 6 dB, Equation (3.1) provides a threshold value equal to 36 dB.

Another way to determine the detection threshold is to use as reference the root-mean square value of the noise in each channel (RMS-status). The RMS-status variable (or RMSS) represents the energy associated with the noise level and is computed by the Vallen software in $[\mu V]$. Data are stored in evenly spaced time intervals of 1 second, independently from the threshold crossing. The recorded data were imported in Matlab™ and plotted in dB using the following equation:

$$RMSS_{dB} = 20log\frac{RMSS_{\mu V}}{1\mu V} \tag{3.2}$$

Usually a minimum value of 20 dB above the steady RMSS value is recommended in order to avoid undesired threshold triggers [18]. In Figure 11 the RMS-status variable (RMSS) over 10 minutes of recording is shown:

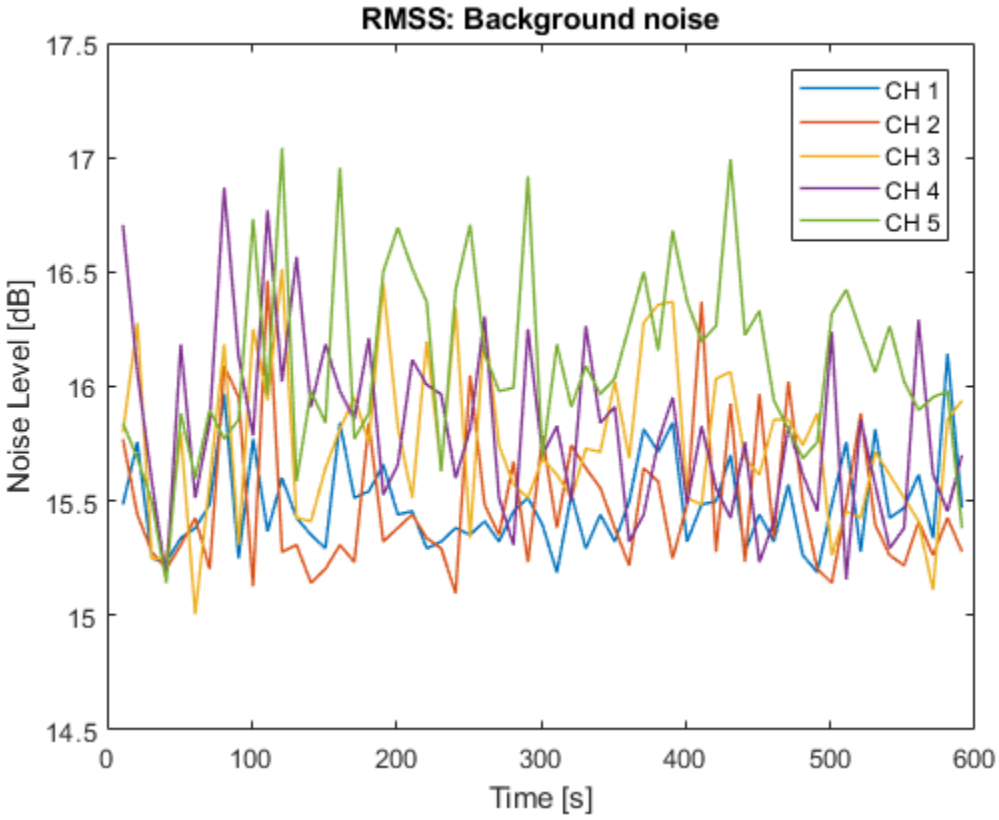

Figure 11 – Noise root-mean square value in each channel over 10 minutes

Adding 20 dB to the RMSS steady value, that can be considered around 16 dB (Figure 11), leads to a threshold value of 36 dB. It is interesting to note that the same result is obtained independently from the method applied, suggesting the reliability of the data. Therefore, 36 dB was taken as an initial threshold setting. After several experiments, with a trial and error approach, it was decided to increase this value up to 38.1 dB in order to avoid any possible undesired hit. A further increase of the value would lead to poor sensitivity of the sensors therefore affecting the quality of the data acquisition process.

3.3 PENCIL LEAD BREAK

A localization algorithm is based on the detection of multiple AE events by several piezoelectric transducers. From the knowledge of the recorded time of arrivals (TOA) and the wave speed, the AE source can be successfully identified using a triangulation technique. Nevertheless, even if the algorithm scheme is relatively simple, determining painstakingly those two parameters is an ongoing challenge for many researches. Therefore, there is the need for calibrating the system through experiments using a reproducible AE source. In 1981, Hsu and Nielsen introduced the so-called Pencil-Lead break technique in an attempt to reproduce a real AE source.

The lead of a mechanical pencil, (usually 2H hardness) is pushed against the structure at a defined angle between 20 and 60 degrees. The lead diameter is 0.3 mm but also 0.5 mm leads are accepted if there is the need for a higher amplitude signal. In order to be consistent, it is recommended to use always the same angle, lead diameter and length (typically between 2 and 3 mm) [19].

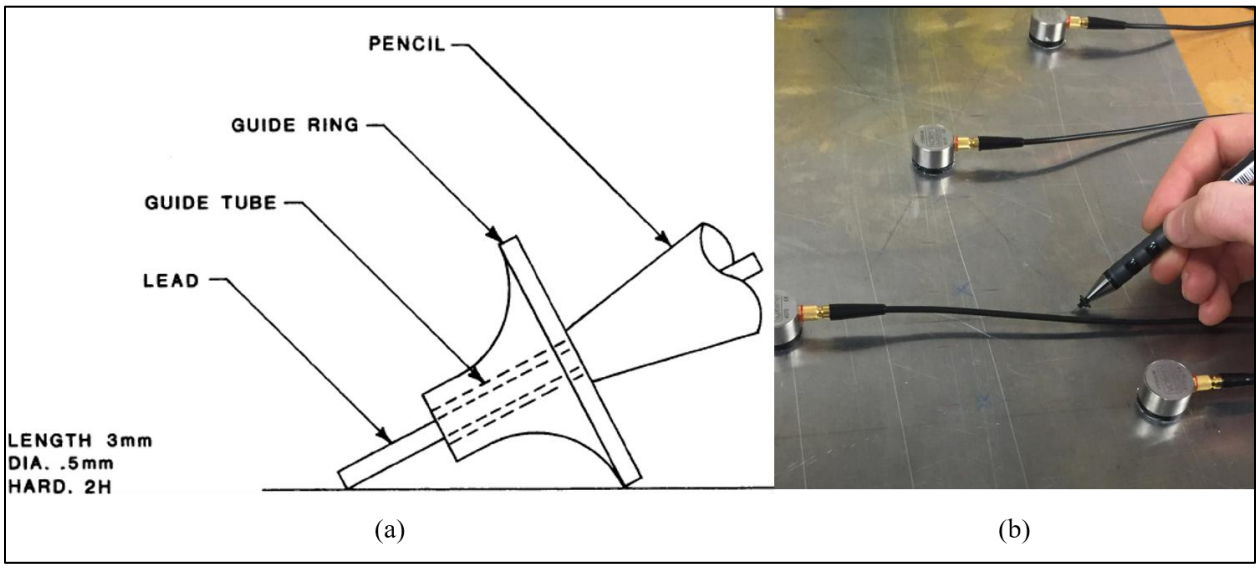

Figure 12 – Pencil Lead Break schematic [19], (a), and during an experiment, (b).

The elastic potential energy is released when the pencil lead breaks generating an AE. Since this experiment can be easily replicated in all common laboratory environments, PLB is a standard tool in many AE studies in order obtain a representative wave speed on that specific structure.

Researchers have been using PLB experiments to characterize the behaviour of AE signals along structures. The frequency and intensity of the different Lamb wave modes, the determination of

group velocities, the signal attenuation, the sensor tuning, and the assessment of the source location performance can be performed by means of a PLB test [20].

3.3.1 Spectrum characterization

A preliminary study about the PLB signal was carried out in order to assess its main characteristics. The Hsu-Nielsen source represents a repeatable acoustic emission, nevertheless each experiment is unique and slightly different from another one due to the many variables that can potentially affect the generated signal. For practical reasons, is almost impossible to perform experiments applying every time exactly the same pressure on the aluminum plate. Moreover, even using the same pressure the pencil lead could brake sooner or later due to internal defects which cannot be controlled. Applying precisely the same contact angle in each test is another challenging task of a PLB experiment.

Bearing in mind the aforementioned considerations, it was decided to perform the same experiment three times using a 2H 0.3 mm diameter lead[1] with a contact angle of 45 degrees. The locations of the PLB test and the chosen piezoelectric sensor are represented in Figure 13 by the red dot on the left-hand side and the red circle on the right-hand side respectively:

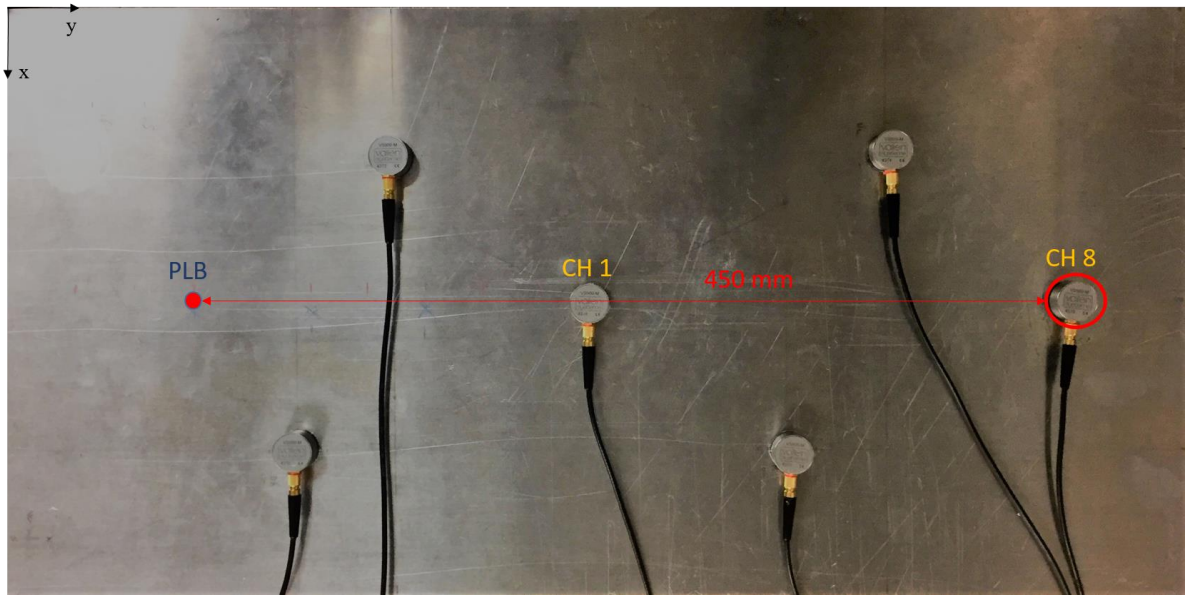

Figure 13 – Experimental layout for spectrum characterization and speed of sound testing

[1] The choice of using a 0.3 lead is due to the fact that the considered geometry is relatively small and a 0.5 lead would lead to a higher amplitude signal reaching the sensor saturation limit of 100 mV.

The relative distance between the acoustic emission source and the transducer (Channel 8) is 450 mm. The results of the three experiments are plotted in Figure 14. The signal is recorded starting from a user defined number of samples before the first hit by means of the "PreTrg" variable. In this case, the pre-trigger was set equal to 200 samples and since the sampling frequency, f_s, is equal to 5 MHz, as a consequence the TOA has to be necessarily of 40 μs. Therefore, in every experiment made with the Vallen Systeme the first TOA is always equal to 40 μs. In section 3.4.1 will be shown that the key parameter is not the TOA itself but the difference between the TOA recorded by different sensors. Moreover, according to the Nyquist-Shannon sampling theorem, with a sampling frequency of 5 MHz it is possible to characterize with no aliasing an analog signal with an upper band-limit of 2.5 MHz. In this study, the maximum frequency of interest is not higher than 500 kHz; therefore, the used sampling frequency is more than enough to avoid aliasing.

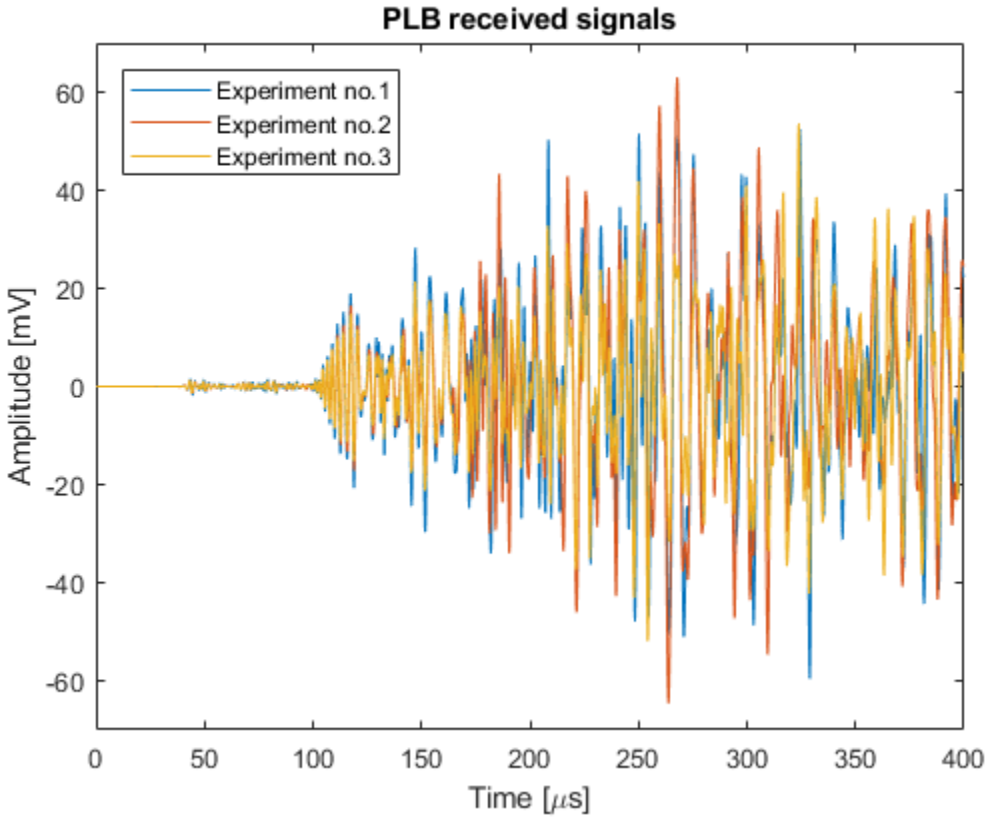

Figure 14 – Plot of the received PLB signals from 0 μs to 400 μs

In Figure 15 is reported a zoom view of the recorded signals in the time interval between 40 μs and 150 μs. The three experiments are quite similar at the beginning whereas they start to diverge after 120 μs. The chosen distance was great enough to appreciate the mode separation. Indeed, the threshold crossing at 40 μs is due to the S_0 mode while the A_0 mode arrives later at around 100 μs.

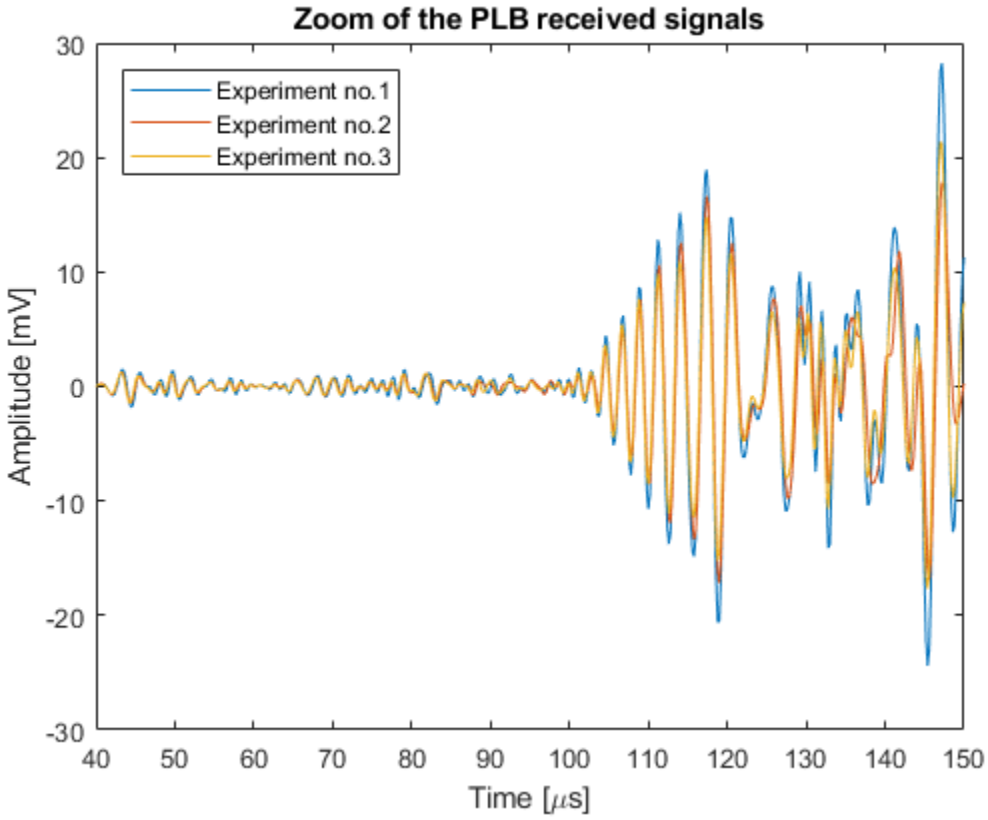

Figure 15 – Plot of the received PLB signals from 40 μs to 150 μs

The spectrum analysis has been performed doing the Fourier transform of the recorded signals and it is represented in Figure 16. The energy is not distributed in uniformly along all the frequencies but is concentrated mainly between 100 kHz and 150 kHz. Moreover, it is interesting to compare this spectrum with respect to the piezoelectric sensor response in Figure 17. The VS900-M is a broadband frequency sensor with characteristic anti-resonances at 200 kHz and 400 kHz. Therefore, the spectrum of the received signal is somehow filtered due to this sensor response. Indeed, the two anti-resonances are also visible in the frequency domain of the received signal.

Nevertheless, the low amount of energy in all the other frequencies greater than 150 kHz cannot be due to the sensor response that has peaks both at 190 kHz and 350 kHz.

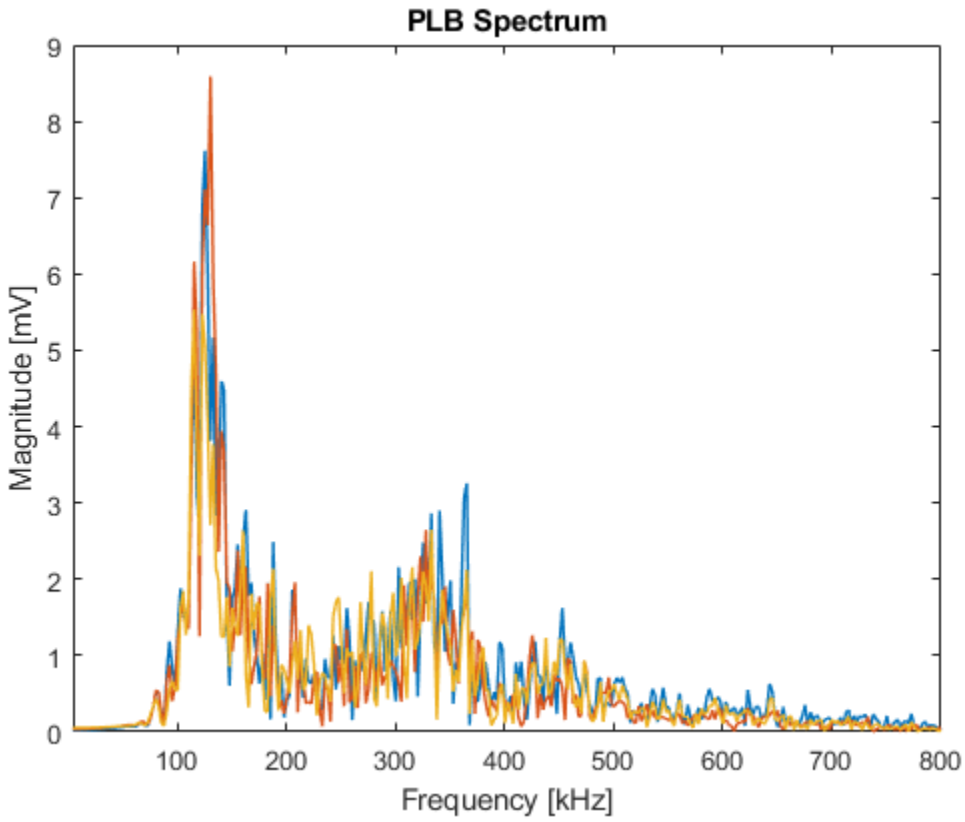

Figure 16 – Fourier transform of the three PLB tests

Actually, the spectrum is not filtered just by the sensor response, but more properly by the system plate-sensor. Anyway, in this phase of the research project, it was assumed that the energy associated to the PLB spectrum is mainly concentrated around 130 kHz, as Figure 18 shows:

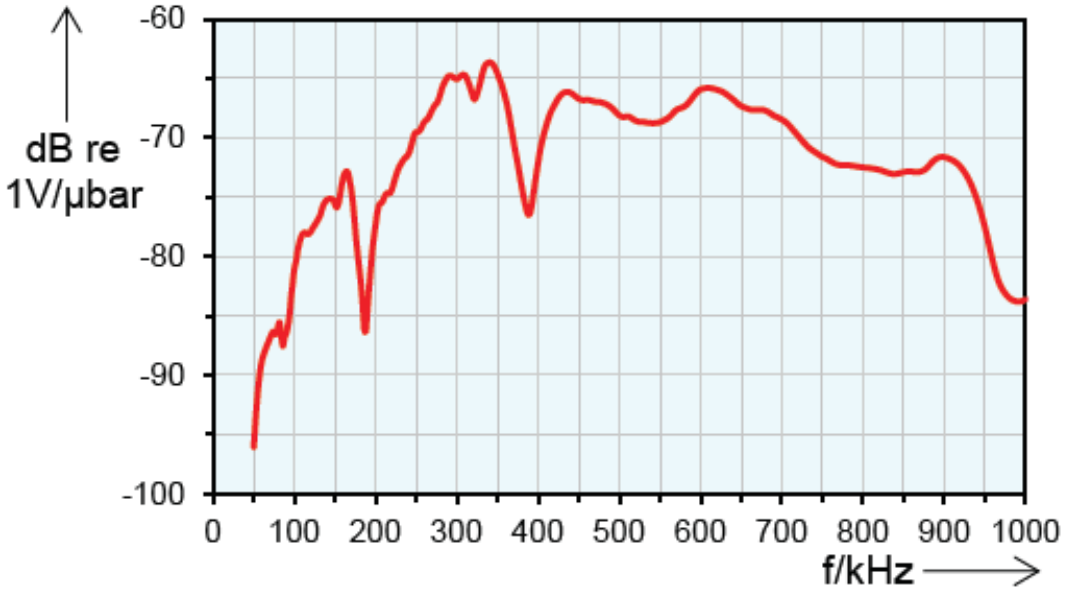

Figure 17 – Piezoelectric sensor VS900-M frequency response

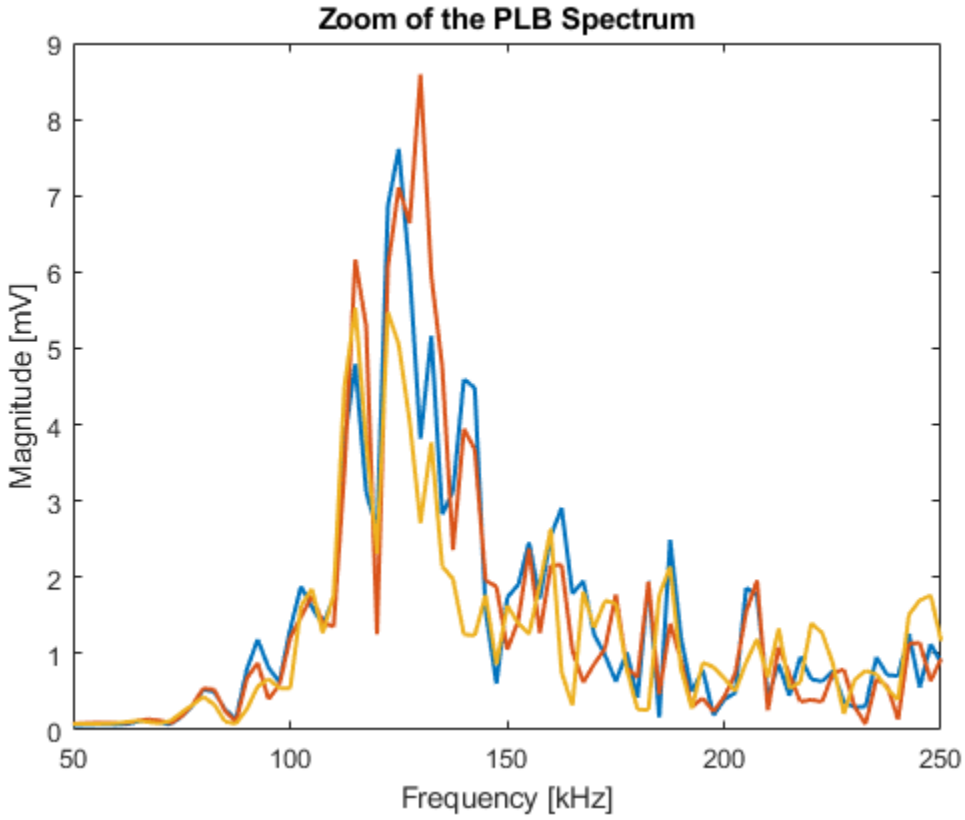

Figure 18 – Fourier transform of the three PLB tests between 50 and 250 kHz

Moreover, even if the actual PLB spectrum is slightly different, the localization algorithm has to be calibrated with the received filtered signal and not with the actual one. Indeed, a frequency component that is completely filtered cannot contribute to the threshold crossing required to determine the TOA.

3.4 LOCALIZATION ALGORITHM

Building an efficient localization algorithm is essential in the context of SHM. It can provide to engineers the source of the acoustic emission location generated by a crack or another kind of material failure mechanism. Typically, localization algorithms exploit triangulation techniques based on the TOA recorded at different transducers attached to the monitored structure. Moreover, it is a crucial aspect in the Time Reversal method, when the source of the signal to be reconstructed is unknown. Finally, it is common in the AE community to exploit the localization algorithm for the speed velocity characterization using active SHM techniques with known source locations. This concept is outlined in section 3.4.3 where an iterative approach will be adopted.

3.4.1 Determining Speed of Sound

The prediction of the source location is linked to the TOA at the different transducers and the characteristic wave velocity in the considered medium. While the TOA parameter is simply recorded by the sensors and directly available for the user, the speed of sound has to be determined.

One possibility is to refer to the analytical model of Lamb waves and then compare the results with the one obtained in the experiments.

3.4.1.1 Analytical approach

The Vallen Systeme provides a software able to plot the dispersion curves of Lamb waves given the longitudinal wave speed c_p, the shear wave speed c_s and plate thickness d. The following value have been used:

- $c_p = 6148\ m/s$
- $c_s = 3097\ m/s$
- $d = 1.59\ mm$

The results are shown in Figure 19:

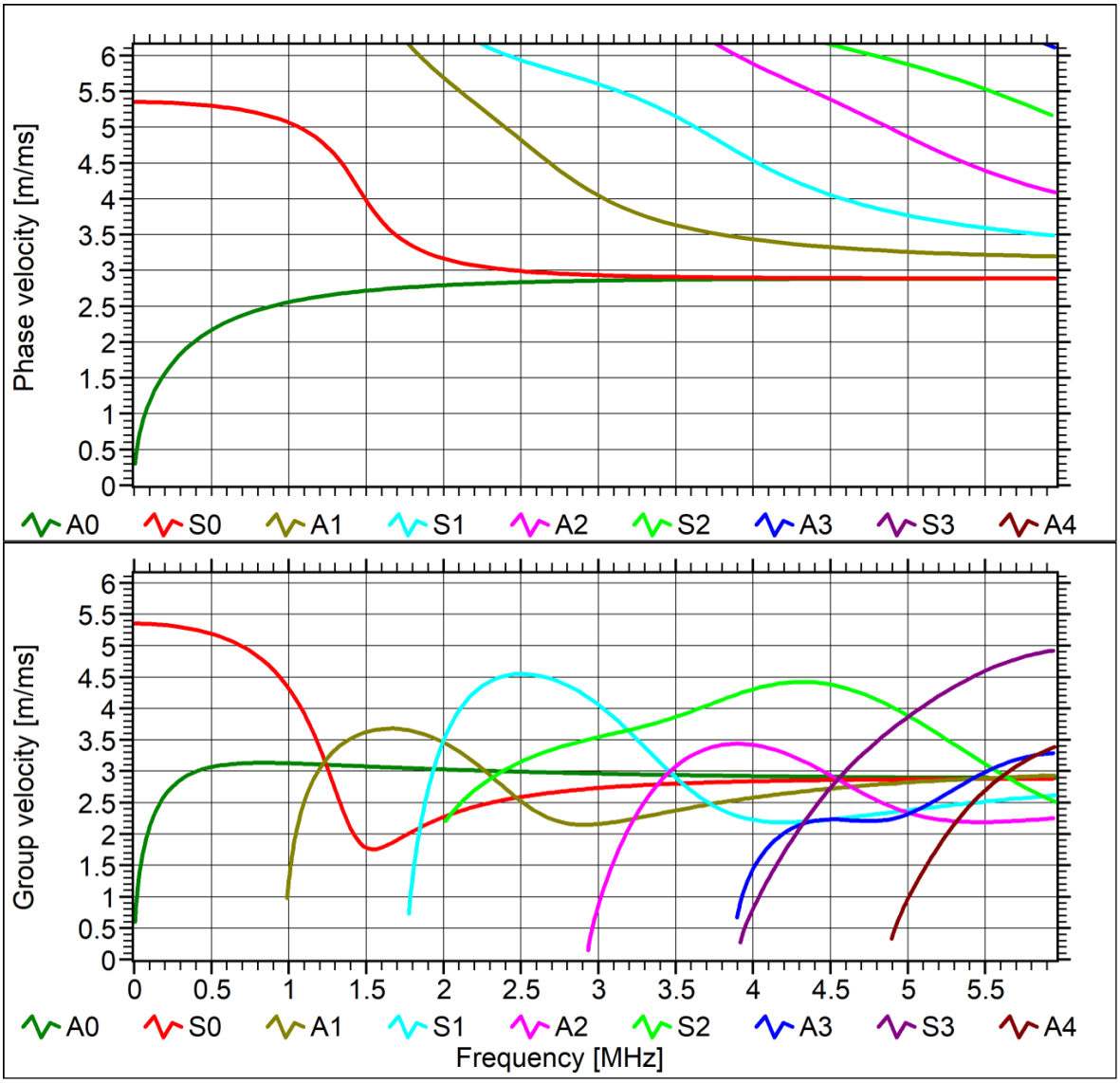

Figure 19 – Dispersion Curves

Considering the fact that the spectrum is characterized by a strong peak at 130 kHz, it is possible to use the dispersion curves of Figure 19 to assess the group velocities of the different modes at that frequency. Firstly, one can observe that only the fundamental symmetric and antisymmetric Lamb wave modes are present at 130 kHz.

The localization algorithm provided by the Vallen System uses as reference for the TOA the first threshold crossing. Therefore, with the selected threshold value, this TOA will be related to the fastest mode recorded by the piezoelectric sensor. From Figure 19 it is clear that the S_0 is much

faster with respect the A_0 in all the frequency range associated with a PLB experiment. In particular, at 130 kHz this analytical model associates a value for the S_0 equal to 5341 m/s. Moreover, the S_0 has a group velocity with a much more stable value, up to 500 kHz, with respect the A_0. The plateau in the range [0-500 kHz] of the S_0 mode group velocity, appreciable in Figure 19, makes it suitable for the localization algorithm even if the frequency is not purely constant since it would produce just a slight change in the estimated group velocity.

3.4.1.2 Experimental approach

The previous obtained result must find confirmation in the experimental results. The same experiment used for the spectrum characterization was also used to assess the S_0 velocity. As it is shown in Figure 13 Sensor 1, associated with Channel no.1, is aligned with the PLB source and Sensor 6, connected with Channel no. 8. This means that it is possible to determine the speed of the S_0 mode simply by dividing the TOA difference, recorded at two transducers, by the relative distance d between them. The latter can be computed from the reading of Table 1:

$$d = 549.7\,mm - 304.8\,mm = 244.9\,mm$$

The recorded TOA[2] are reported in Table 2, where the $\boldsymbol{S_0}$ mode velocity and the percentage error with respect to the result of 5341 m/s derived from the analytical model utilizing the Vallen software is also computed.

Table 2 – TOA and S_0 velocity computation

Exp. no.	TOA [μs]		Δ TOA [μs]	d [mm]	$\boldsymbol{S_0}$ Speed [m/s]	% Error
	CH. 1	CH. 8	CH. 8-1	CH. 8-1	CH. 8-1	CH. 8-1
1	21.2	67.9	46.7	244.9	5244.1	-1.85
2	21.7	68.2	46.5	244.9	5266.7	-1.41
3	21.1	67.7	46.6	244.9	5255.4	-1.63

Taking an average between the three experiments one obtains the following group velocity related to the S_0 mode.

[2] The TOA are related to the threshold crossing of the closest sensor to the AE source. Hence, in this case they are referred taking as zero TOA the threshold crossing in Sensor 4.

$$c_g = 5255.4\ m/s \ \ = 206.9\ in./\ ms$$

The speed derived from the experiment is slightly lower than the one computed analytically (5341 m/s), precisely 1.63% slower. Anyhow, this result is still consistent with the theory. Indeed, the analytical models does not consider the wave attenuation due to damping. A decrease in amplitude due to damping (both geometrical and structural) affects the threshold crossing, shifting the TOA of few microseconds and, consequently, only apparently decreasing the expected speed.

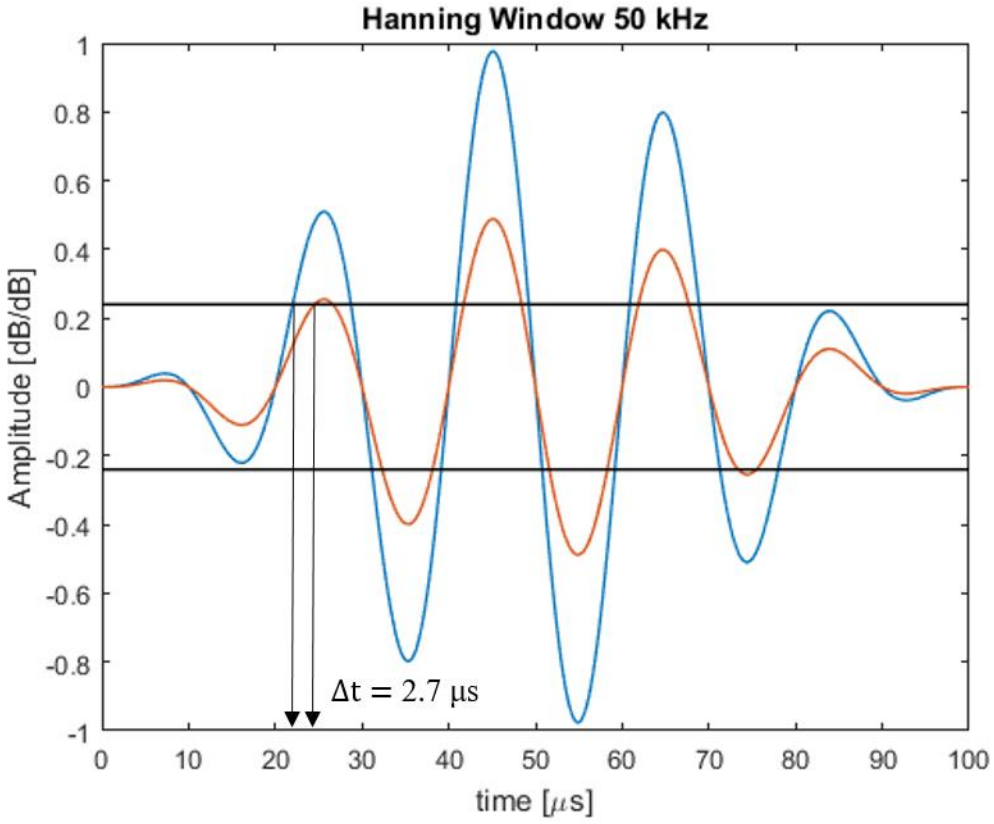

Figure 20 – TOA shift due to a decrease in amplitude

Figure 20 shows this concept, using normalized values. It highlights a delay of 2.7μs in the TOA comparing two Hanning Window functions with the same frequency of 50 kHz but different amplitudes. Decreasing the threshold crossing can reduce this error with the drawback to be more sensitive to background noise, as seen in paragraph 3.2.

3.4.2 Localization algorithm set-up

The computed S_0 velocity is now used in the localization algorithm set-up.

The layout of the experiments is reported in Figure 21, while Table 1 and Table 3 report the sensor and PLB locations respectively.

Table 3 – PLB test location layout

Test	Coordinates [mm]		Coordinates [in.]	
	X	Y	X	Y
PLB 1	76.2	152.4	3	6
PLB 2	101.6	406.4	4	16
PLB 3	228.6	457.2	9	18
PLB 4	203.2	203.2	8	8

The light green dots represent the chosen PLB AE sources. In each location, four PLB experiments with a 0.3 mm lead at 45 degrees where performed.

The recorded signals have been analyzed using the following algorithm structure sequence:

1. Location processor;
2. Cluster processor;
3. Polygon processor;
4. LUCY filter;
5. 2D plot of the results.

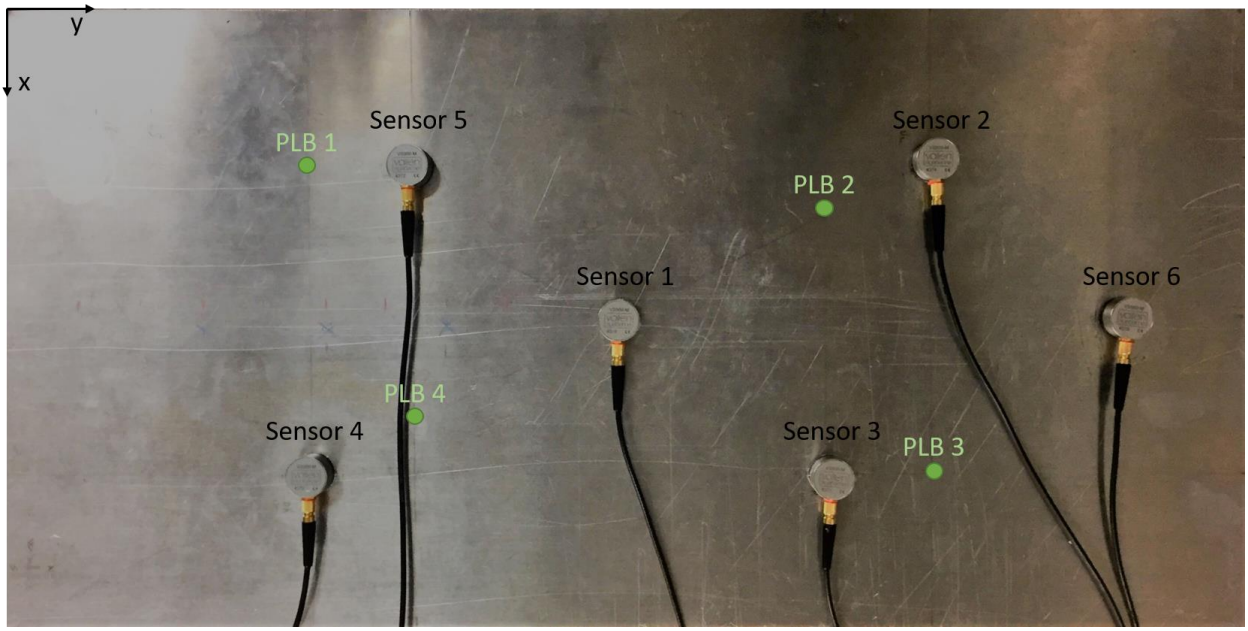

Figure 21 – Layout for the localization algorithm and PLB sources represented by the green dots

3.4.2.1 Location Processor

The Vallen System provides a localization algorithm based on the difference of the TOA related to each sensor. In particular, to every TOA difference, related to a pair of sensors, corresponds a certain distance computed multiplying that TOA difference by the user defined velocity which in this case is 206.9 in./ms. The result is the generation of a hyperbola for each couple of sensors. Indeed, a hyperbola is defined as the set of all points such that the difference of the distances between any point and the foci is constant. In this kind of application, the two foci are the pair of piezoelectric transducers. The source location could lie in every point belonging to the hyperbola. The intersection of different hyperbole produces the predicted source location. As an example, in Figure 22 the aforementioned processor is applied to identify one of the four sources (PLB 4) of the experiment. The hyperbole converges in one single point, the estimated AE source location. Of course, a certain uncertainty is present, and this is estimated with the LUCY processor that will be describe in section 3.4.2.4.

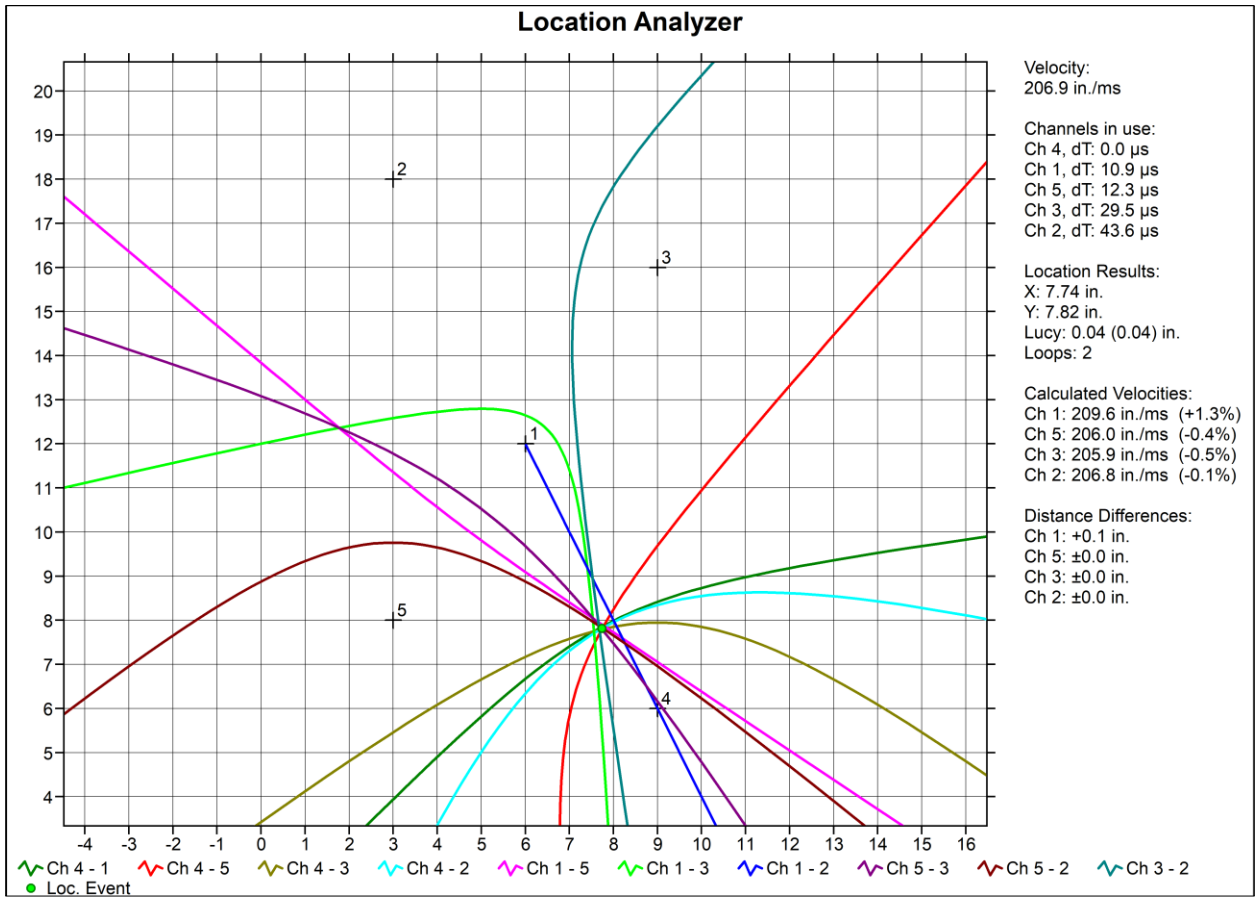

Figure 22 – Example of the Localization analyzer processor

3.4.2.2 Cluster processor

The Cluster processor is a tool used for a better visualization of the results. The user defines a certain radius for the cluster that groups the results by means of circles with different colors according to the number of AE sources present inside those circles. In this experiment, a radius of 0.4 inches (10.16 mm) has been chosen.

3.4.2.3 Polygon processor

The polygon processor filters all the results that fall outside the defined polygon. The latter has to be representative of the plate configuration, therefore having the same shape and dimension of the aluminum sheet used for the experiment.

3.4.2.4 LUCY filter

External disturbances, undesired reflection, poor accuracy in the experiment execution are all factors that can lead to potentially wrong results. Therefore, the data have to be further filtered and this is done by means of the LUCY filter.

The Localization Uncertainty (LUCY) can be considered a measure of the source position accuracy with respect the measured TOA differences. It consists in the standard deviation from a set of *measured* values D_i to a set of *calculated* values P_i. Its expression is represented by Equation (3.3):

$$LUCY = \sum_{i=1}^{n} (D_i - P_i)^2 / (n-1) \tag{3.3}$$

Where index "i" represents the i-th hit sensor. D_i is computed multiplying the *measured* TOA difference by the user defined speed of sound. On the other hand, P_i identifies the distance computed multiplying the *calculated* TOA difference by the previous defined speed of sound. In particular, the *calculated* TOA difference refers to the result of the computed source position.

The result of this algorithm, related to this experiment, is mapped in Figure 23 using a 3D plot with histograms.

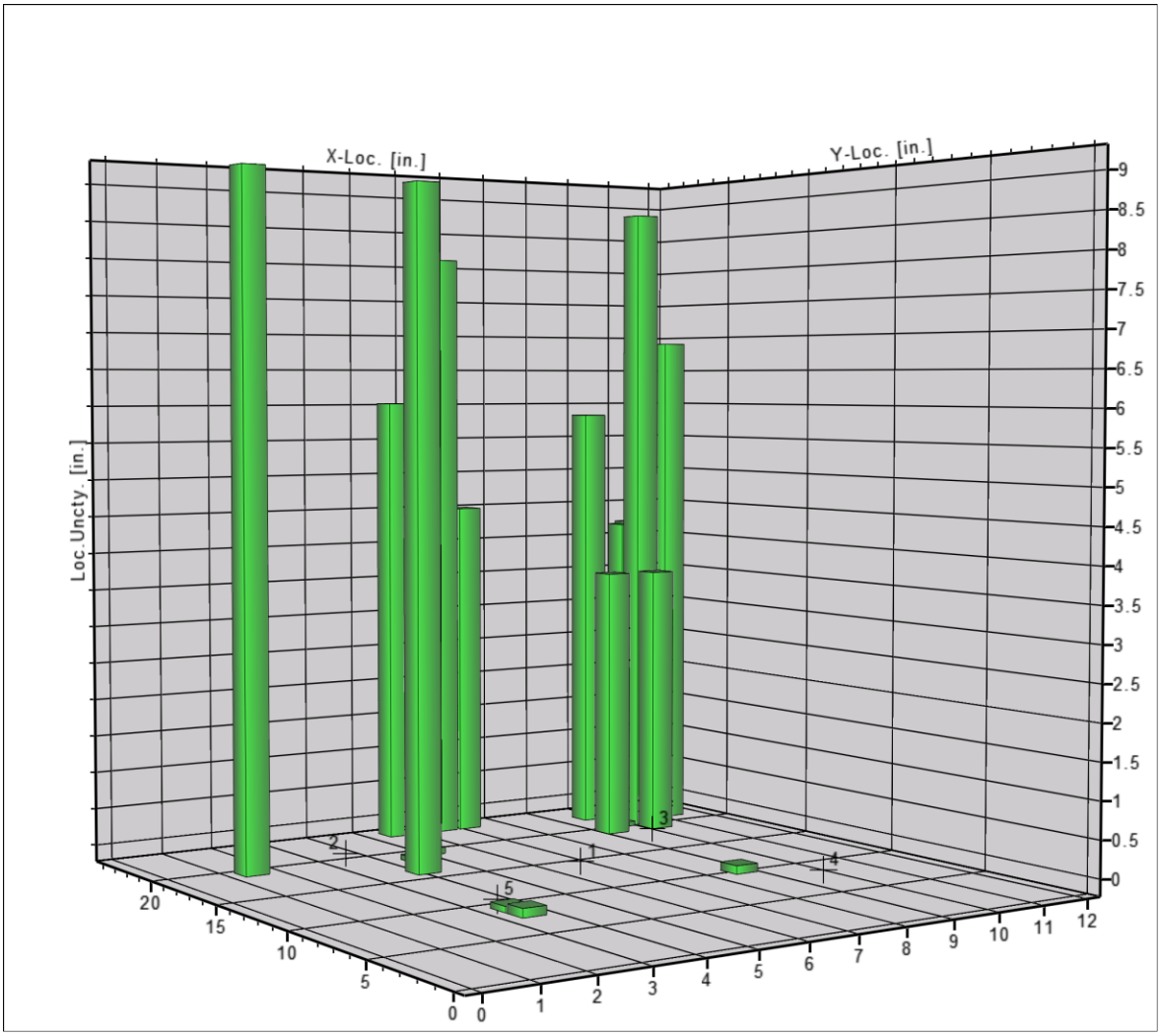

Figure 23 – Lucy results 3D representation

Then a result is considered valid if and only if the following condition is satisfied:

$$|LUCY| \leq 0.3$$

The choice of the threshold for the LUCY parameter is arbitrary and has to be defined by the user in such a way the wrong results are filtered without discarding also the right ones.

3.4.2.5 2D plot of the results

In Figure 24 are plotted the computed sources locations using 5 of the 6 available sensors:

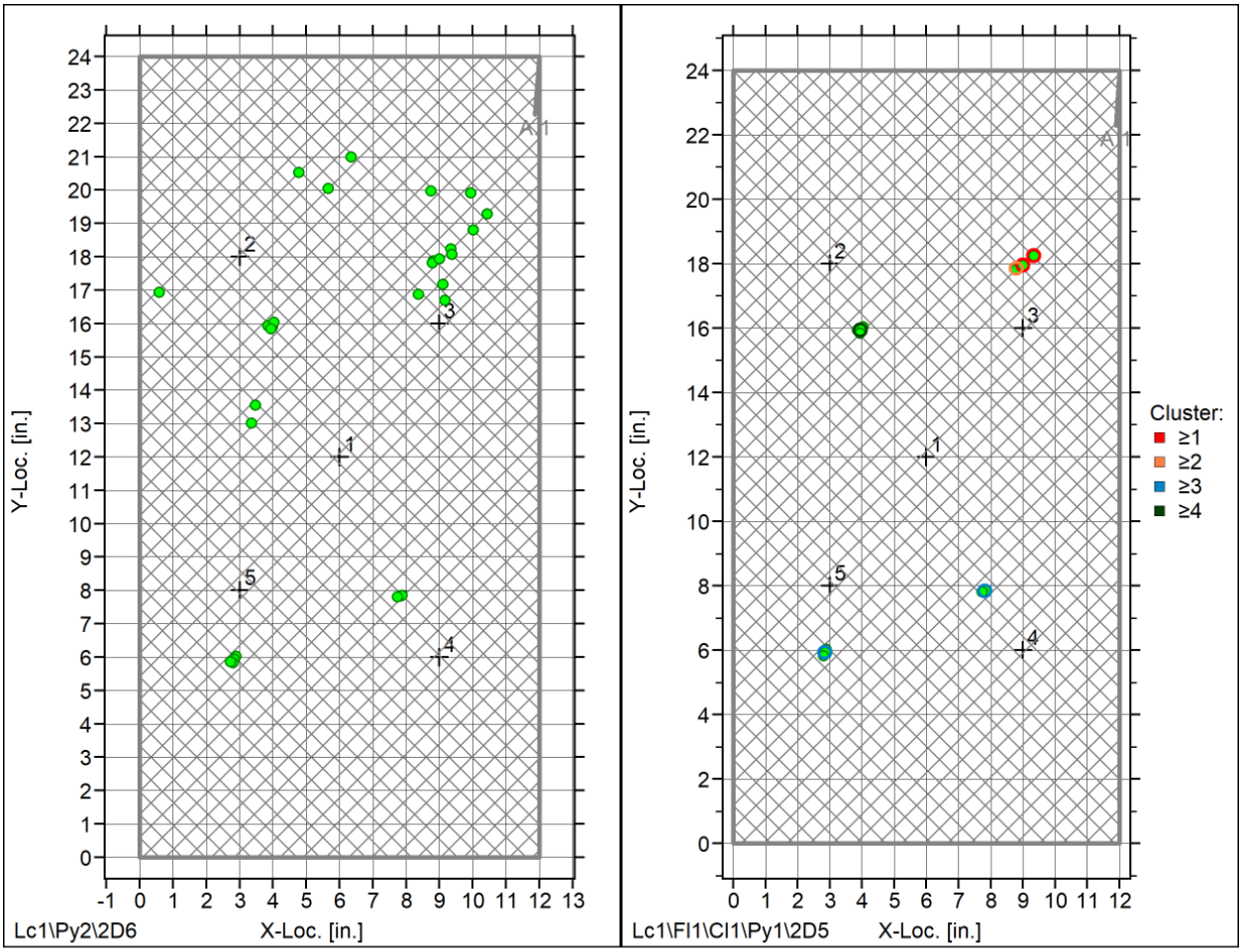

Figure 24 – Comparison between unfiltered (a) and filtered (b) results

The results are satisfactory for all the four sources even if the PLB 3 location has some uncertainty. In this case, the application of an extra sensor helps to handle this kind of problems.

Indeed, using also sensor number 6, associated to channel 8, there is a significant improvement that can be appreciated in Figure 25:

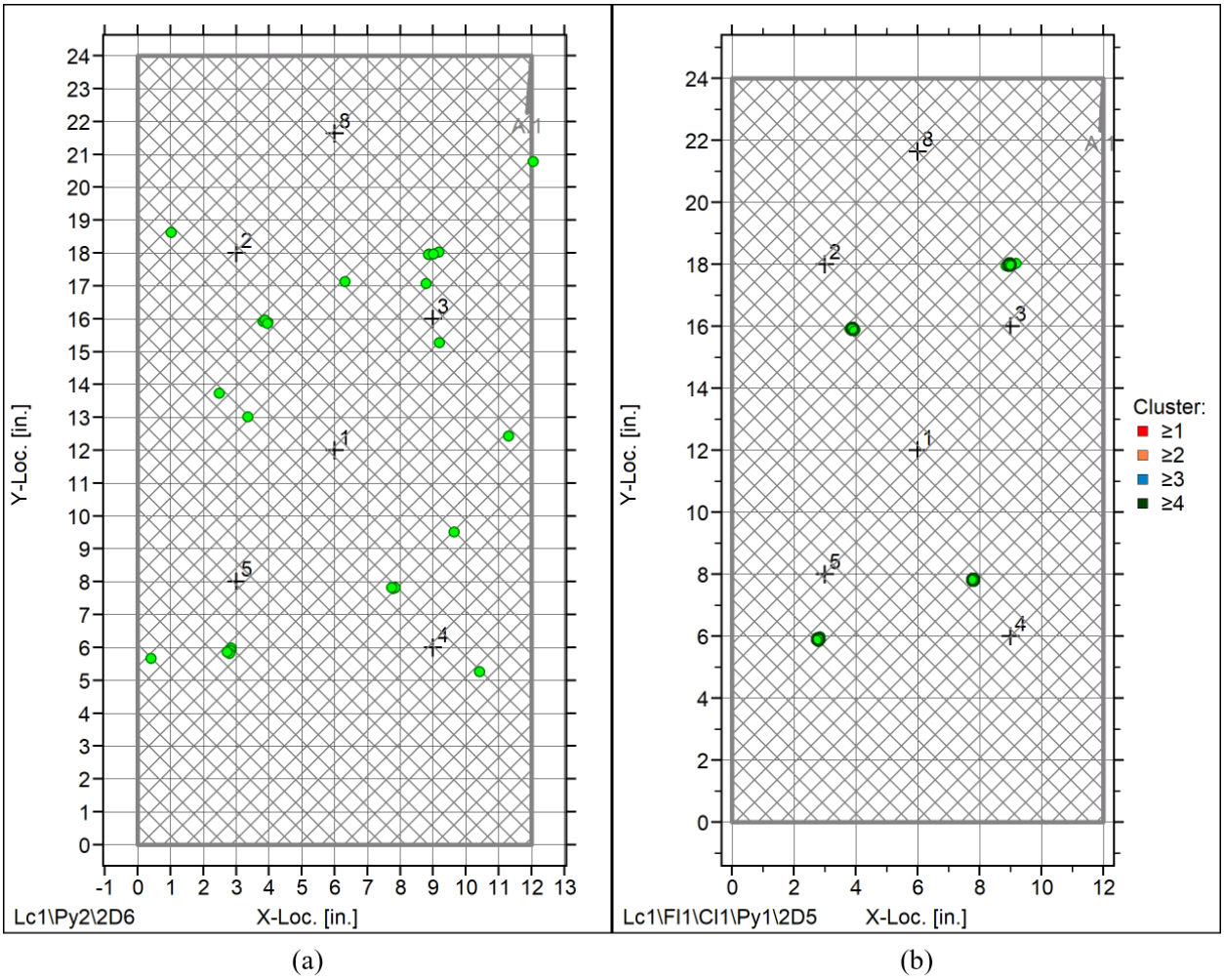

Figure 25 - Experimental results: unfiltered (a) and filtered using LUCY algorithm (b)

The extra sensor added in proximity of the region with the higher uncertainty further over constraints the problem leading to much more accurate results.

3.4.3 Localization algorithm flow chart

Thanks to the results provided by the localization algorithm it is possible to modify the previous computed speed of sound in such a way that the LUCY parameter is minimized. This leads to an iterative process that is represented in Figure 26:

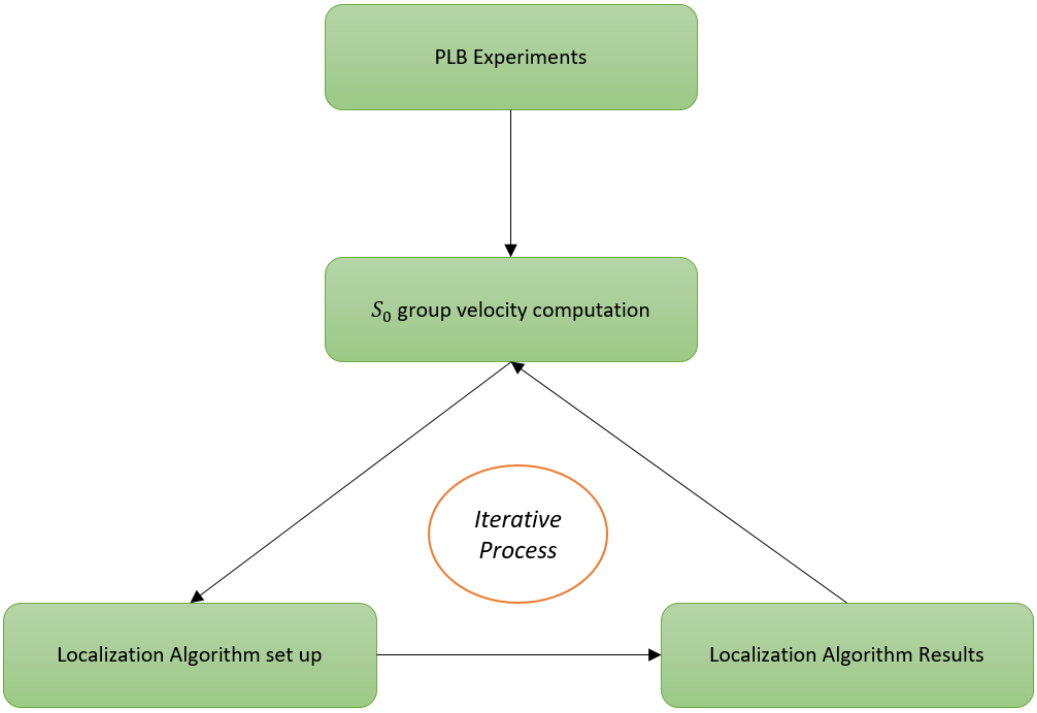

Figure 26 – Scheme regarding the calibration of the localization algorithm

At the end of this iterative process the optimized velocity value for the S_0 mode has been slightly reduced from 206.9 $in./ms$ to 206.5 $in./ms = 5245.1\ m/s$.

3.5 MEASURING ATTENUATION

Modeling attenuation is a crucial step in the Time Reversal Process. Indeed, the received signal in each sensor has to be normalized because of the different sensor sensitivity. This depends on the coupling between the sensor and the plate and on the sensor itself. Therefore, once the signal is received and normalized, it has to be rescaled according to the expected attenuation that is a function of the distance from the source previously computed by means of the localization algorithm describe in section 3.4.

3.5.1 Mathematical formulation of damping for a propagating wave

It is worth to start introducing the wave equation in which damping is taken into account:

$$\phi(r,t) = A\frac{1}{\sqrt{r}}e^{-\eta r}e^{i(\omega t-\gamma r)} \tag{3.4}$$

Where r is the distance from the AE source, A is the magnitude of the signal, ω is the angular frequency, γ is the wave number and η is the damping coefficient that has to be estimated experimentally [21]. From Equation (3.4) it is possible to observe two different sources of damping: geometric spreading, $1/\sqrt{r}$, and structural damping, $e^{-\eta r}$. The first one, is simply a consequence of the wave propagation and therefore does not require any particular expedient in order to be implemented in a numerical model. The latter represents a dissipative phenomenon and changes in every material according to the different mechanical properties. Its implementation in a numerical code requires the knowledge of the η parameter. The assessment of the damping coefficient is not an easy task especially because in many low dissipative materials such as metals, the structural damping is somehow hidden behind the geometric spreading. This is true especially in the so called “near field” where the geometrical damping is dominant.

3.5.2 Assessment of the damping coefficient

In order to assess the damping coefficient η, several PLB experiments were performed progressively increasing the distance from a defined piezoelectric sensor. Another choice could have been to perform a single PLB experiment and recording the emitted signal from several piezoelectric sensors at different distances. This possibility has the drawback of dealing with the changing in the sensitivity between the different sensors. This can be due for instance to not

properly identical coupling between the different sensors and the plate. For this reason, it has been decided to use the first approach with a fixed sensor and a moving location for the PLB tests. Moreover, to minimize the variability between the different PLB experiments, three experiments for each location have been performed in order to take as reference the average of the recorded signals. The layout of the experimental set-up is represented in Figure 27:

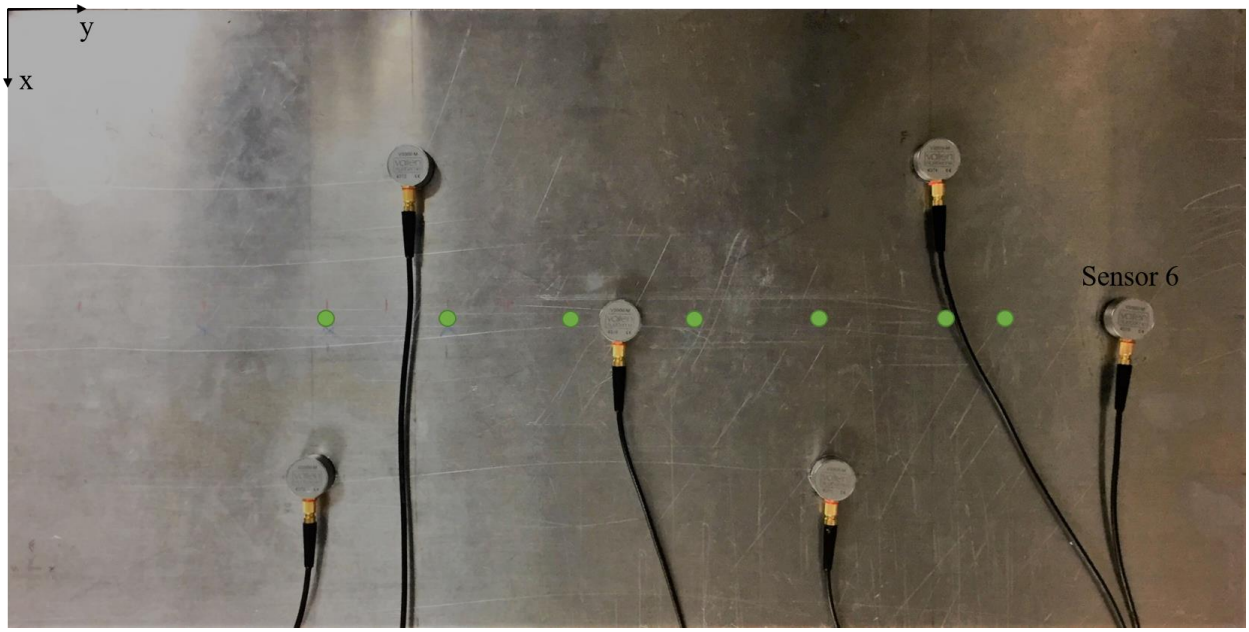

Figure 27 – Experimental layout with the PLB (green dots)

As a reference for the amplitude estimation, only the S_0 mode has been considered. The reason lies in the fact that it is very complicated to choose in an objective way the amplitude of the A_0 mode. Figure 28 shows the same three experiments previously shown in Figure 14 trying to recognize and highlight the different modes. As anticipated, the S_0 is relatively easy to identify while the selection of the A_0 is challenging.

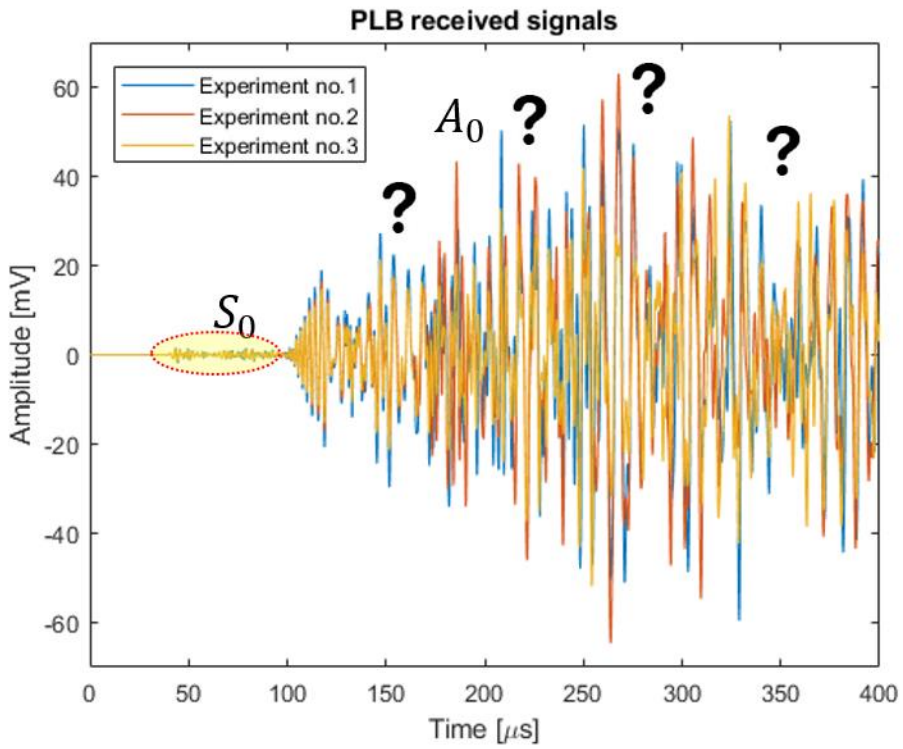

Figure 28 – Mode recognition in the received PLB signals

This is due to the dispersion effect affecting the A_0 mode that arises when more than one frequency is present in the system. It is reported in literature that the A_0 mode attenuation cannot be studied looking at the amplitude, but rather using energy considerations due to dispersion induced attenuation effects [21]. Therefore, it has been decided to study the attenuation effect considering as reference the maximum peak of the S_0 mode. Then, through a Matlab™ code, the different amplitude values with respect the distance from the PLB source were plotted in Figure 29. Moreover, in the same figure are also plotted three functions representing the geometrical spreading, the structural damping and the envelope of Equation (3.4). The value of A and η have been obtained with a trial and error procedure, choosing their values in such a way the curve fitting with the wave equation (denoted as Analytical in Figure 29) was optimal, leading to $A = 1.2$ and $\eta = 2.6$.

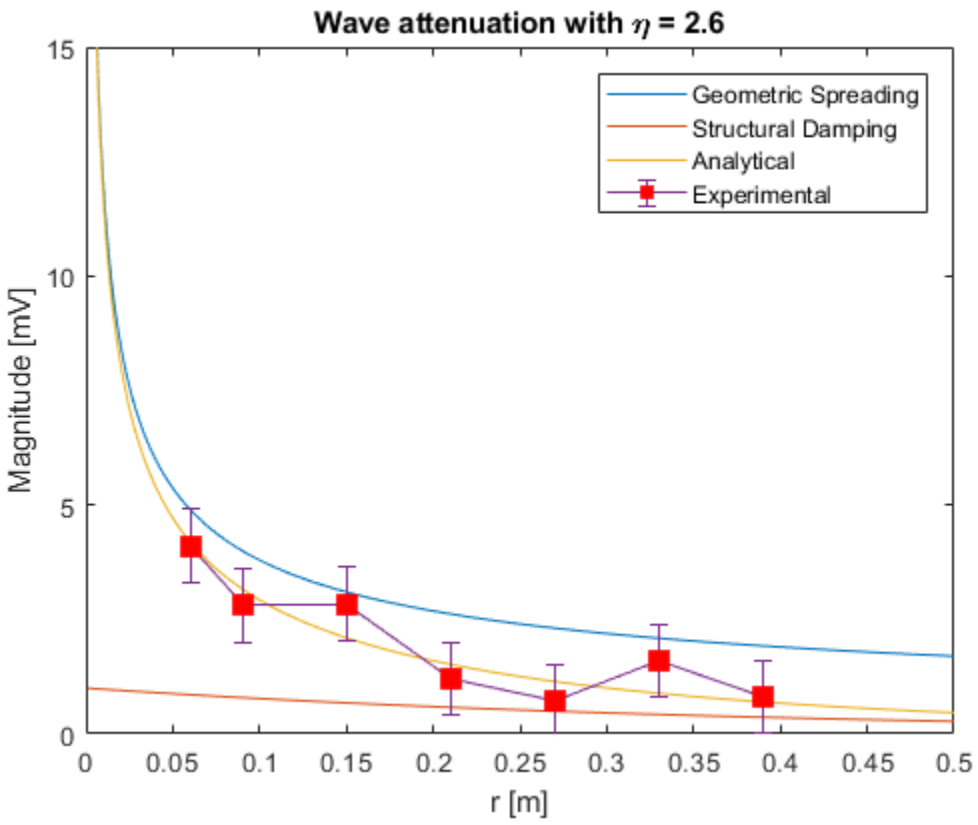

Figure 29 – Experimental received signals at different distances

CHAPTER 4

4 FEM MODELING METHODOLOGY

This chapter introduces the numerical model developed in ABAQUS CAE™ making use of the implicit solver. The different steps of the applied methodology and the techniques used are described and discussed.

4.1 SELECTED SOLVER: ABAQUS/STANDARD

As anticipated in the first paragraph of this chapter, the implicit solver, Abaqus/Standard, was selected to carry out the numerical simulations. It is a well-known fact that in an implicit dynamic analysis there is not any stability restriction affecting the time increment. Therefore, in such kind of analysis, the time step is governed only by accuracy considerations. On the other hand, explicit solvers are typically conditionally stable and must satisfy stability constraints. Since they do not require to invert the stiffness and global mass matrices at each time increment, may be convenient in certain kind of problems to use such methods albeit their time increment is expected to be smaller compared to implicit solvers. In particular, for low model size complexity, implicit solvers are expected to perform better while, when the degrees of freedom of the model grow above a certain threshold, the explicit solvers show a consistent computational cost saving with respect the implicit solvers, which have to deal with the inversion of huge matrices [22].

Nevertheless, the reason of such choice does not lay on stability requirements and neither on computational cost considerations. Abaqus/Standard allows the user to model piezoelectric elements which are fundamental in this analysis. On the other hand, Abaqus/Explicit cannot do the same and would require particular implementations in the software to be utilized for such aim. For this reason, even if in the literature there are many studies about Lamb waves propagation using explicit solvers (without modeling the piezoelectric material and therefore using simple point loads to mimic their action on the structure), Abaqus/Standard has been selected.

4.2 MACHINE USED

The numerical simulations were performed in a Window 10 workstation with 2 Intel® Xeon® CPU E5-2620 v3 (12 cores and 24 logical) running at 2.40 GHz with 128 Gb or RAM.

4.3 MODEL DESCRIPTION

4.3.1 Plate and extra boundaries

The plate was modeled reproducing rigorously the specimen dimensions given in paragraph 3.1.2. Moreover, extra boundaries, surrounding the plate, were added in the numerical setup. Those will be addressed in paragraph 4.6 and, in this first phase of the numerical model development, they do not show any special property.

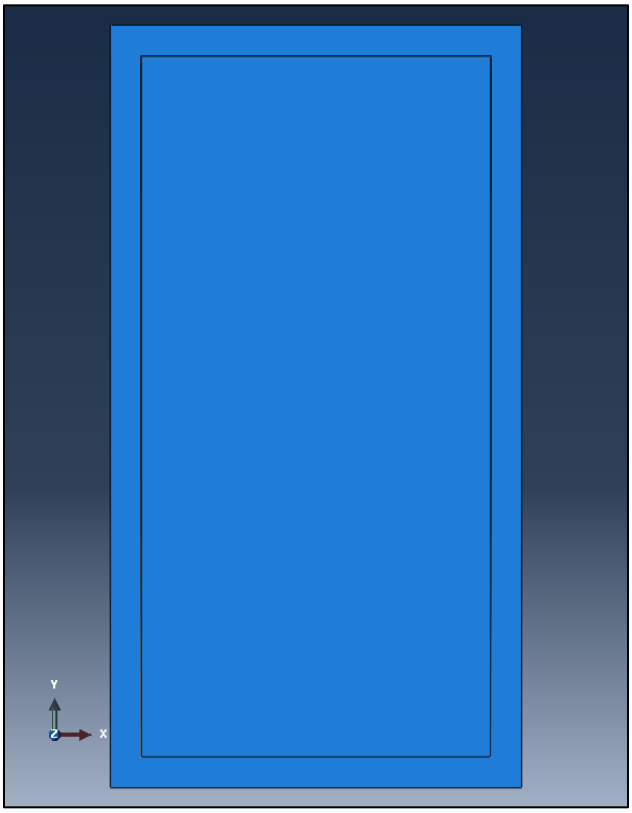

Figure 30 – Specimen designed in ABAQUS CAE™ with extra boundaries

4.3.2 Piezoelectric sensors

The transducers were modeled as cylinders made by piezoelectric elements. The VS900-M datasheet, available in Vallen Systeme website [23], provides the dimensions of the transducer, but only the inner part of the sensor without the surrounding stainless-steel case was considered in the numerical model. Figure 31 shows the meshed part of a piezoelectric sensor in ABAQUS CAE™ with a diameter of 6.5 mm and a height of 0.25 mm.

When defining the material properties for piezoelectric elements, ABAQUS CAE™ requires specifying the dielectric and the material's piezoelectric stress coefficient matrices. Those values were chosen according to reference [24].

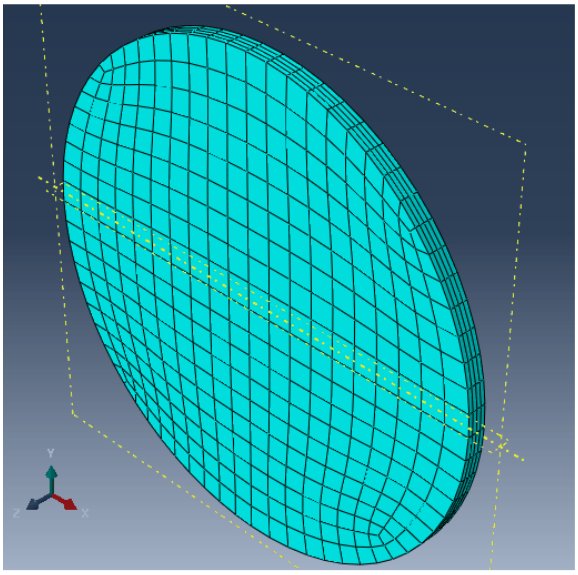

Figure 31 – Meshed piezoelectric sensor

4.3.3 Boundary Conditions

The numerical model requires two different types of boundary conditions: mechanical and electrical. Both are needed to properly simulate propagating Lamb waves. All the six degrees of freedom of the structure were constrained in order to avoid any free body motion. Those mechanical boundaries conditions were applied only at the corners of the structure, in order to avoid edge reflections. All the piezoelectric elements were fixed to the structure using a “tie

constraint" available in ABAQUS CAE™, connecting the upper plate surface (master surface) with the bottom sensors surface (slave surface).

Electric potential boundary conditions were used at every piezoelectric sensor. As a matter of facts, every transducer must be grounded in order to measure a voltage difference. This was accomplished by applying a zero-voltage boundary condition at the bottom surface of the different piezoelectric sensors. When a transducer was used as an actuator, an electric potential boundary condition with the corresponding voltage amplitude was applied in its upper surface.

4.4 STABILITY CONSIDERATIONS

The convergence of the numerical model is strictly related to the spatial and temporal resolution used in the simulation. In order to avoid instability issues the mesh must have elements sufficiently small such that it is possible to resolve the propagating wave from a spatial point of view [25]. In the performed simulations the element size has been chosen in accordance to reference [26], placing a minimum of 15 nodes for the smallest wavelength present in the simulation:

$$L_e \leq \frac{\lambda_{\min}}{15} \tag{4.1}$$

Moreover, has been noticed in several simulations that a minimum number of 4 elements through the thickness direction is required to avoid anomalies in the wave propagation.

On the other hand, the time step is a function of the maximum frequency of the problem as shown in the equation below [27]:

$$\Delta t = \frac{1}{20 f_{max}} \tag{4.2}$$

4.5 DAMPING MODELING

Modeling damping phenomena related to Lamb wave propagation is an ongoing challenge in the AE community. ABAQUS CAE™ offers the possibility to use the Rayleigh damping model. This model considers the damping matrix, [C], as a linear combination of the mass, [M], and stiffness, [K], matrices as outlined in Equation (4.3):

$$[C] = \alpha[M] + \beta[K] \tag{4.3}$$

Gresil and Giurgiutiu demonstrated how the coefficients α and β can be chosen in order to obtain the desired exponential decay [21]. This concept is summarized in the following Equation (4.4):

$$\frac{1}{2}(\alpha + \beta\omega^2) = \eta c_0 \tag{4.4}$$

Where ω is the wave angular frequency, c_0 is the wave speed and η is the damping coefficient experimentally derived in paragraph 3.5.2. The proposed methodology requires two parameters, ω and c_0. Therefore, the Rayleigh model is suitable for narrowband signals, as Hanning window functions, and for a specific Lamb wave mode, A_0 or S_0 for instance. In this study, the challenge is to model a PLB signal characterized by a wide spectrum range and multimode wave packets. Referring to Figure 16, it is possible to affirm that, even if the frequency components of a PLB test range within 0-800 kHz for our setup, there is not a significant amount of energy in frequencies higher than 400 kHz, with a clear peak at 130 kHz. Hence, the angular frequency required in Equation (4.4) was considered equal to the main spectrum component of 130 kHz. The other issue is the choice of the right wave speed, c_0. In theory, the two fundamental modes A_0 and S_0 present in our frequency range require different α and β coefficients since they have different group velocities. At this point, it is worth to ask if a Rayleigh damping based model it is the best choice to predict Lamb wave attenuation. This topic is still under investigation in the AE community and there is no clear answer yet. In this study, it was decided to use as reference the group velocity related to the S_0 fundamental mode, $c_0 = 5245.1$, previously derived at the end of section 3.4. The choice was devised considering that the damping coefficient, η, derived experimentally, was also related to the S_0 attenuation. As such, it is now possible to enter this value in Equation (4.4) and plot all the possible combinations of α and β. Figure 32 shows on a semi-log graph the positive

values of the mass and stiffness damping coefficients because the ABAQUS CAE™ numerical model accepts only positive numbers.

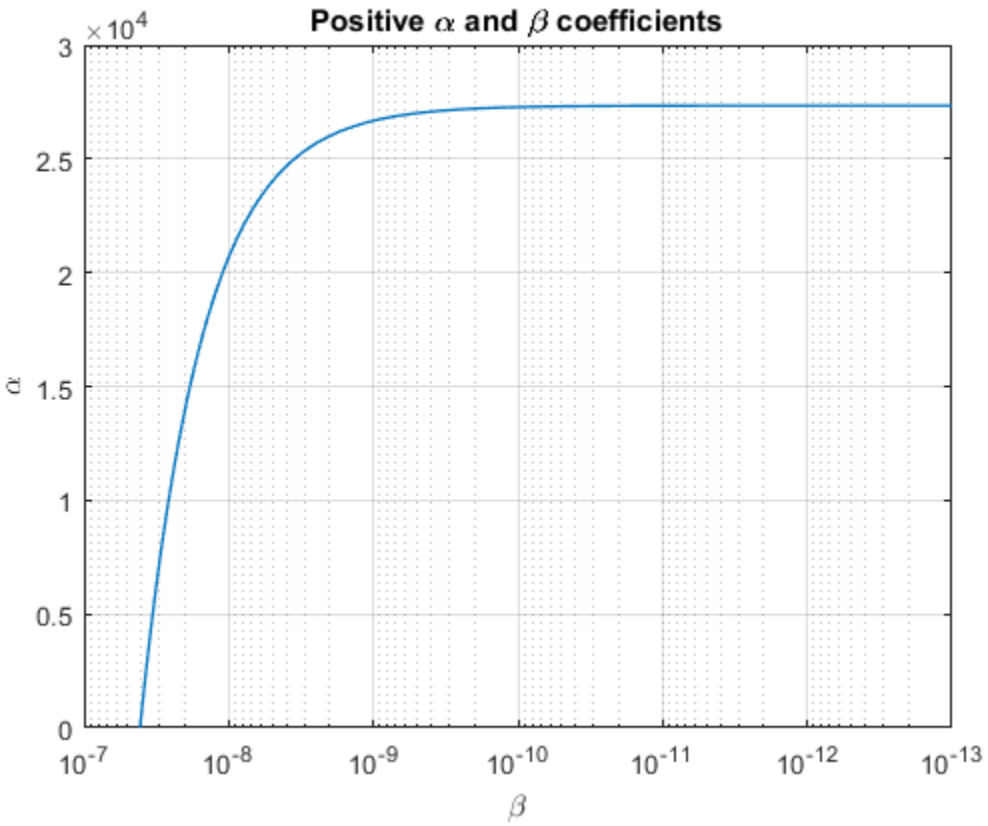

Figure 32 – Plot of the possible α and β values to implement in the numerical model

It was decided to take the minimum stiffness damping coefficient value, hence $\beta \cong 0$ and the corresponding mass damping coefficient leading to $\alpha \cong 27500$. The reason of keeping the value of β as low as possible is linked to stability considerations. As a matter of fact, a high value of β can potentially reduce the stable time increment, as found in [22]. The obtained coefficient were then used in a numerical simulation in which the attenuation of an Hanning window of 130 kHz – main PLB frequency – was assessed using a series of piezoelectric sensors placed in a row, as reported by Figure 33. The progressive increase of the distance from the central actuator is outlined in Table 4.

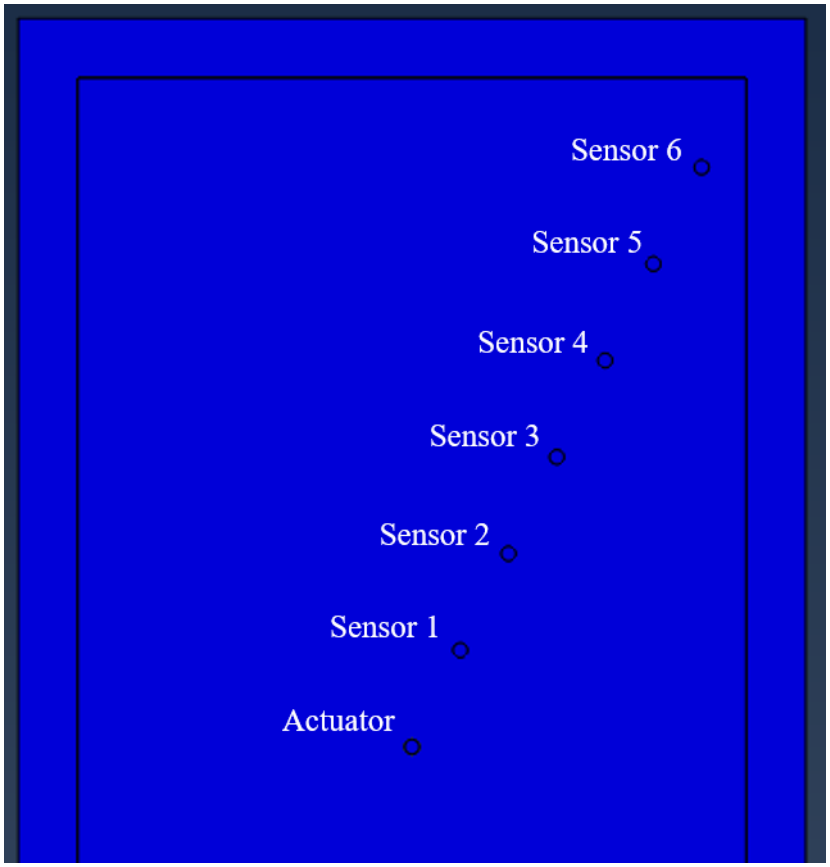

Figure 33 – Upper half model top view: damping simulation layout.

The relative distance between the piezoelectric sensors is always 49.2 mm. It is not recommended to further reduce this distance in order to avoid interaction effects between the piezoelectric sensors. As such, it was reported by Hamstad et al. [28], that the following condition must be satisfied:

$$D/s \geq 7 \tag{4.5}$$

Where D is distance from the source location or from another piezoelectric transducer in the case of interaction phenomena, and s symbolizes the source size. Applying Equation (4.5), using as source size the dimension of the VS900-M piezoelectric sensor, $s \cong 7$ mm, one obtains the proposed value of 49.2 mm. It was verified that for the used D value, no interaction phenomena occurred.

Table 4 – Sensor relative distance from the central actuator in the damping simulation

Sensor	Distance from the Actuator [mm]
1	49.2
2	98.4
3	147.6
4	196.8
5	246.0
6	295.2

A preliminary analysis was performed running a simulation without any damping in order to assess the consistency of the model. According to the theory, the Lamb waves decay should follow the geometric spreading curve. This kind of damping is simply associated with the fact that the energy injected in the system is spreading in a wider area of the plate, causing as a consequence, a decrease in the amplitude that is proportional to the inverse of square root of the distance from the AE source, $1/\sqrt{r}$. In this simulation an actuation voltage of 10 V was set. Figure 34 confirms the expected results.

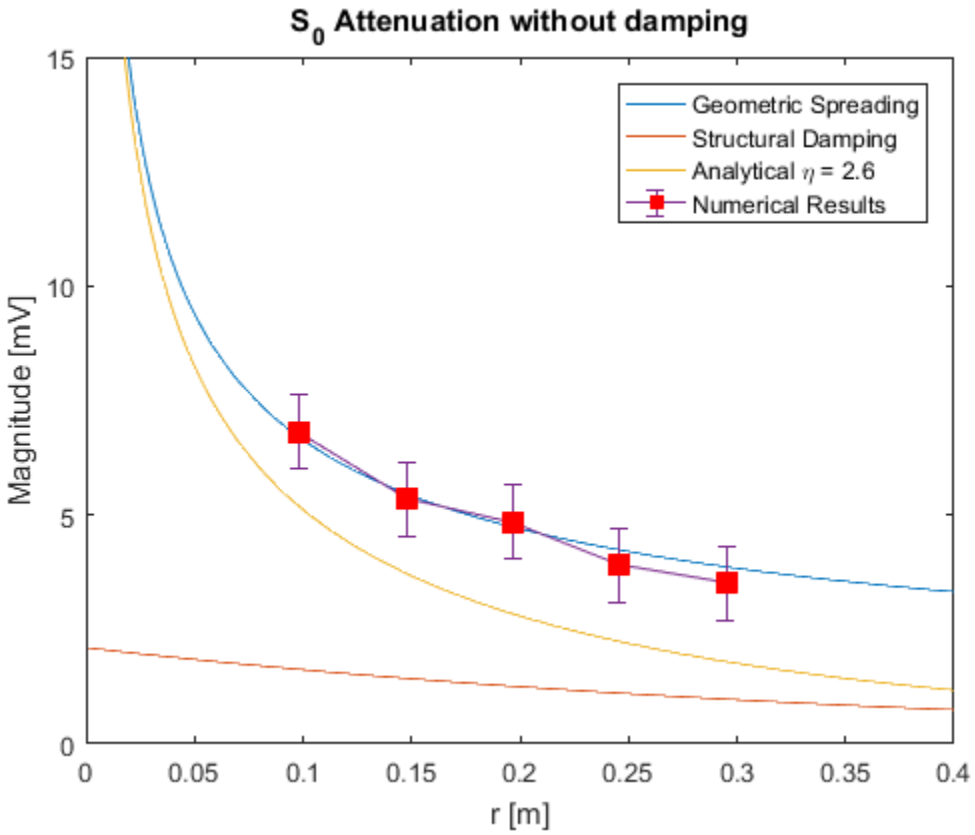

Figure 34 – Simulation results: $\alpha = 0$ and $\beta = 0$

One may wonder why only five data points are present in the plot. Indeed, the layout shown in Figure 33 makes use of six piezoelectric sensors and an actuator. The reason is that at 49.2 mm the S_0 wave packet is still mixed with the A_0 mode, making impossible the assessment of its amplitude, as outlined by Figure 35 in correspondence of the orange dashed line.

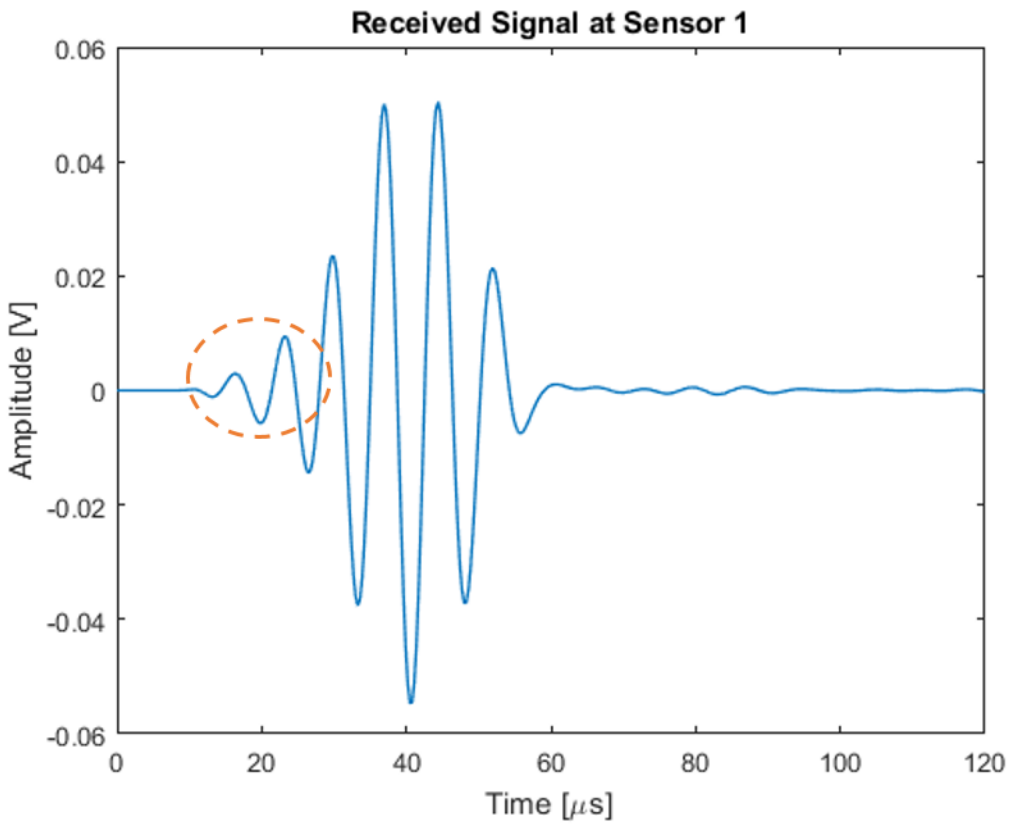

Figure 35 – Example of S_0 and A_0 mixed waves packets received at Sensor 1.

On the contrary, increasing the distance from the central actuator, the symmetric S_0 has enough time to separate from the antisymmetric A_0 mode, allowing the user to read easily the its relative amplitude.

As a second step, the previously computed damping coefficient were implemented in the numerical model. Preliminary results showed that the wave packet was overdamped by the numerical model with respect an exponential decay characterized by $\eta = 2.6$. Therefore, a trial and error procedure was used in a iterative process that converged to $\alpha = 20000$ and $\beta = 0$. Figure 36 shows that for those values of α and β the numerical model causes a damping of the wave packet according an exponential law with $\eta = 2.6$, matching the behavior of the wave in the experimental results.

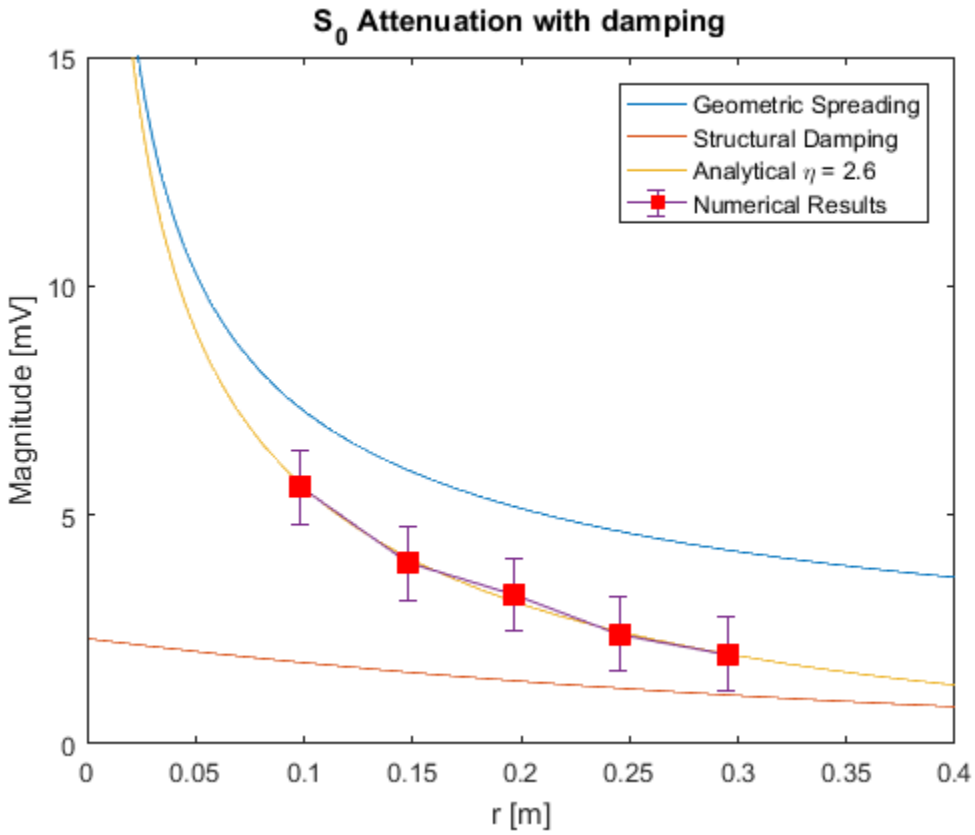

Figure 36 – Simulation results: $\alpha = 20000$ and $\beta = 0$

Therefore, in the following part of this study, the wave attenuation has been modeled according to those values of the stiffness and mass proportional damping coefficients.

4.6 NON-REFLECTIVE BOUNDARIES (NRB)

In this section, the problem of building absorbing boundaries in the numerical problem is addressed. The stability requirements, represented by Equation (4.1) and Equation (4.2), may impose a high number of elements in the meshed part and a small time step. Researches and engineers try to optimize the model by refining the mesh only in the areas of interest leaving a coarse mesh quality elsewhere. In this study, the geometry is relatively simple, being just a flat plate, but the number of elements in the model can arise due to the stability constraint which can make unpractical any numerical simulation, especially if the problems contains Lamb waves at high frequencies. Moreover, if the simulated AE signal is long enough, and usually this is the case, reflections coming from the boundaries will interfere with the signal itself, compromising the quality of the emitted signal and complicating the analysis of the recordings in the different

sensors. The simplest solution would be to increase the plate dimensions. Consequently, the reflections will take more time to bounce back towards the sensors and their amplitude at that moment will be low enough to be considered negligible. Nevertheless, this solution is not feasible. Indeed, increasing the size of the model implies a proportional increase in the element number and, consequently, of the computational cost. This drawback can be avoided using the so-called "non-reflective boundaries" (NRB) [29]. A wide literature review was carried out in order to decide the best approach for this purpose. All the methodologies have in common the idea to absorb the elastic waves hitting the boundaries but using different strategies.

In the next paragraphs, different techniques are proposed explaining their features and implementation. Finally, numerical results are shown, and the most effective method is selected. This allows the user to concentrate the computational effort only around the desired location, leading to a more efficient numerical model.

4.6.1 Infinite elements

The method was proposed for the first time by Lysmer and Kuhlemeyer [30], and is available in Abaqus CAE™ as "infinite elements". Despite that, the infinite element property cannot be selected by the user directly inside the Abaqus CAE™ environment. Therefore, a methodology has been developed through the implementation of a Matlab™ code. The infinite element boundaries were shaped to surround the plate edges as is reported in Figure 37 (a). The mesh configuration plays a crucial role for the proper implementation of the infinite elements. The number of the elements through the thickness is not significant while the element orientation is fundamental. The geometry was partitioned in four regions (North, East, South, West) and the cells were assigned a "stack direction" in such a way all the elements were pointing outward with respect the centre of the plate, as it is highlighted in Figure 37 (b).

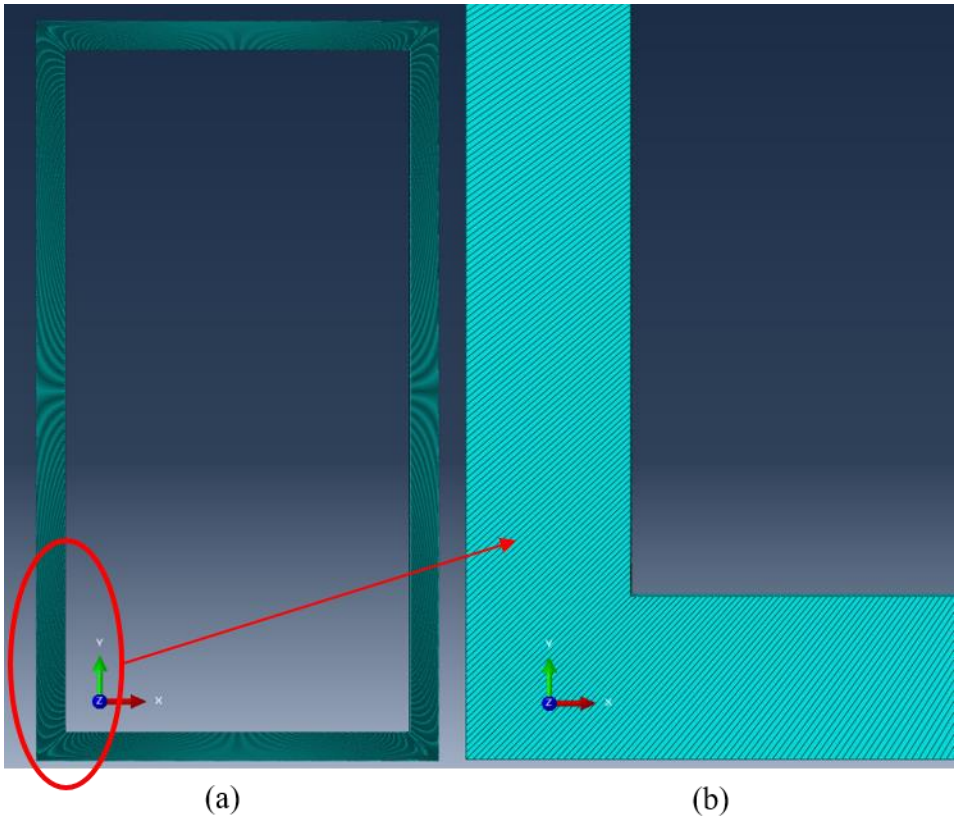

Figure 37 – Infinite elements geometry configuration (a), zoom on the south-west corner (b)

The generated input file was then modified through a Matlab™ code to assign the infinite element property to the regions of interest. This is done substituting the string "AC3D8" into with "CIN3D8" in the input file[3]. Importing the modified input file in Abaqus CAE™ the new geometry shows the infinite boundaries as shown in Figure 38.

[3] The acronym "AC3D8" stands for "acoustic elements" that were used temporarily to build the model since the input file cannot be created if the mesh elements have not any property assigned.

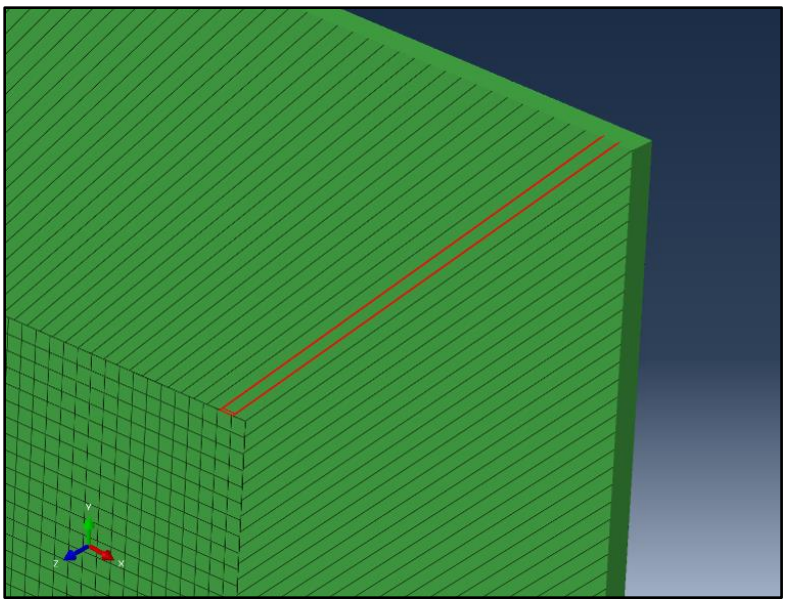

Figure 38 – Infinite boundaries

The method is relatively simple to implement but numerical results showed that it is not capable to absorb effectively all the reflections coming from the boundaries [31].

4.6.2 Rayleigh damping and dashpot elements

Other attempts were performed using the concepts of Rayleigh damping (the same used to model wave attenuation) and dashpots elements. Both aim to absorb the incident wave using a dissipating region around the plate edges.

In the first case, the material is assigned values for the mass and stiffness damping coefficients, α and β respectively. The wave shows an exponential decay proportional to the given values of α and β, but reflections occur at the interface between the plate and the absorbing region edges due to the abrupt change in acoustic impedance. For this reason, even if the increasing of the damping coefficients induces a faster exponential decay, a tradeoff must be found in order to avoid high impedance mismatches at the interface between the two materials. Nevertheless, the numerical results shown in section 4.6.4 demonstrated that the remaining reflections coming from the boundaries were not negligible.

The second method tries to dissipate energy connecting the mesh nodes at the plate boundaries to dashpots that are grounded. This technique requires assigning specific direction and damping coefficient to the dashpots [32]. Potentially this method is effective and relatively simple to apply.

Nevertheless, the mesh size is strictly related to the number of dashpots because they are connected to each node at the boundary. Thus, refining the mesh quality would highly affect the absorbing region performances even if the previously assigned dashpot parameters (direction and damping coefficients) remain unaltered. As a result, the implementation of dashpots as absorbing elements is challenging and needs to be optimized by means of further studies that are outside the objective of this thesis.

4.6.3 Stiffness Reduction Method (SRM)

The SRM has been developed by Pettit et al. in an attempt of providing better performances with respect the absorbing techniques based on the damping Rayleigh model. More precisely, it can be considered the evolution of the Absorbing Layers using Increasing Damping (ALID) [29]. In the ALID method, the impedance mismatching issues are compensated by a smooth changing in the material properties going outward with respect the centre of the plate. It has been reported that some β coefficient values can produce numerical instability and for this reason, its value it is kept constant while the value of α changes [33]. The SRM makes use of the same concept but adds another degree of freedom (DoF) to the problem. As such, not only the proportional mass damping coefficient, α, but also the Young's Modulus, E, is changing [34]. The width of the SRM region surrounding the plate edges should be at least 1.5 λ_{inc}, where λ_{inc} is the incident wave length. Since the S_0 and the A_0 have different wave lengths, using a conservative approach the larger one between the two was taken as reference, which is to say the S_0 wavelength. Figure 39 shows the absorbing region divided in *n* layers, each one with a different value of α and E.

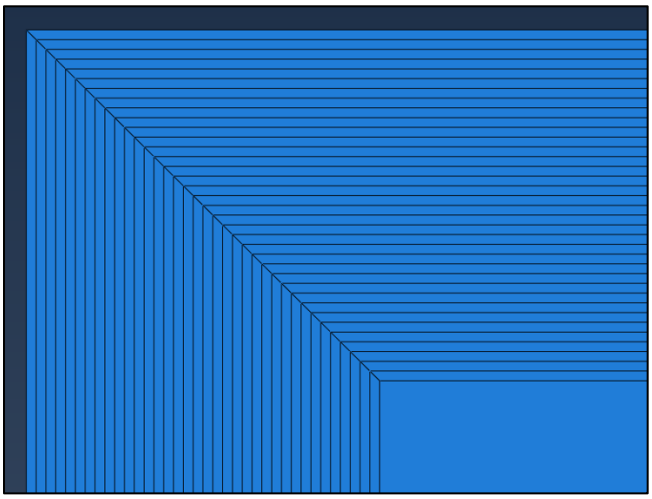

Figure 39 – SRM geometry layout with n=36

The proportional mass damping coefficient, α, changes according to Equation (4.6):

$$\alpha(x) = \alpha_0 + \alpha_{max} X(x)^p \tag{4.6}$$

Where *x* is an integer corresponding to the layer number starting from the plate edges, $x = 0$, to the end of the SRM region, $x = n$. $X(x)$ is a polynomial function of p order with the following boundary conditions: $X(0) = 0$ and $X(n) = 1$. The parameter α_0 represents the mass proportional damping coefficient used to model wave attenuation in the plate, while α_{max} is chosen with a trial and error procedure starting with $\alpha_{\max} = \omega$ as initial guess value, where ω is the angular wave frequency of the incident wave. In the trial and error procedure α_{max} is progressively increased because the higher it is, and the more amount of energy can be absorbed by the boundaries. Nevertheless, there is also an upper limit since an exaggerated value of α_{max} could cause acoustic impedance mismatches resulting in wave reflection.

On the other hand, the Young's Modulus, E, follows the law expressed by Equation (4.7):

$$E(x) = E_0 e^{-\sigma(x) k_{inc} x} \tag{4.7}$$

Where E_0 is the original value of the Young's Modulus in the plate, k_{inc} the is the incident wave number of the mode with the bigger amplitude[4] and $\sigma(x)$ is the function described in Equation (4.8):

$$\sigma(x) = \sigma_{\max} X(x)^p \tag{4.8}$$

Finally, the term $\sigma_{\max}$ has been taken with a trial and error procedure such as the ratio $E(n)/E(0) = 0.01$, which is to say that $\sigma_{\max}$ is taken in such a way that the Young's Modulus in the last layer of the SRM region reaches the 1% of its initial value. As an example, it is reported in Figure 40 the evolution of the α and E in the SRM region tuned for 50 kHz.

[4] Here, the A_0 mode has been taken as reference because at 50 kHz its amplitude is much higher compared to the S_0 mode.

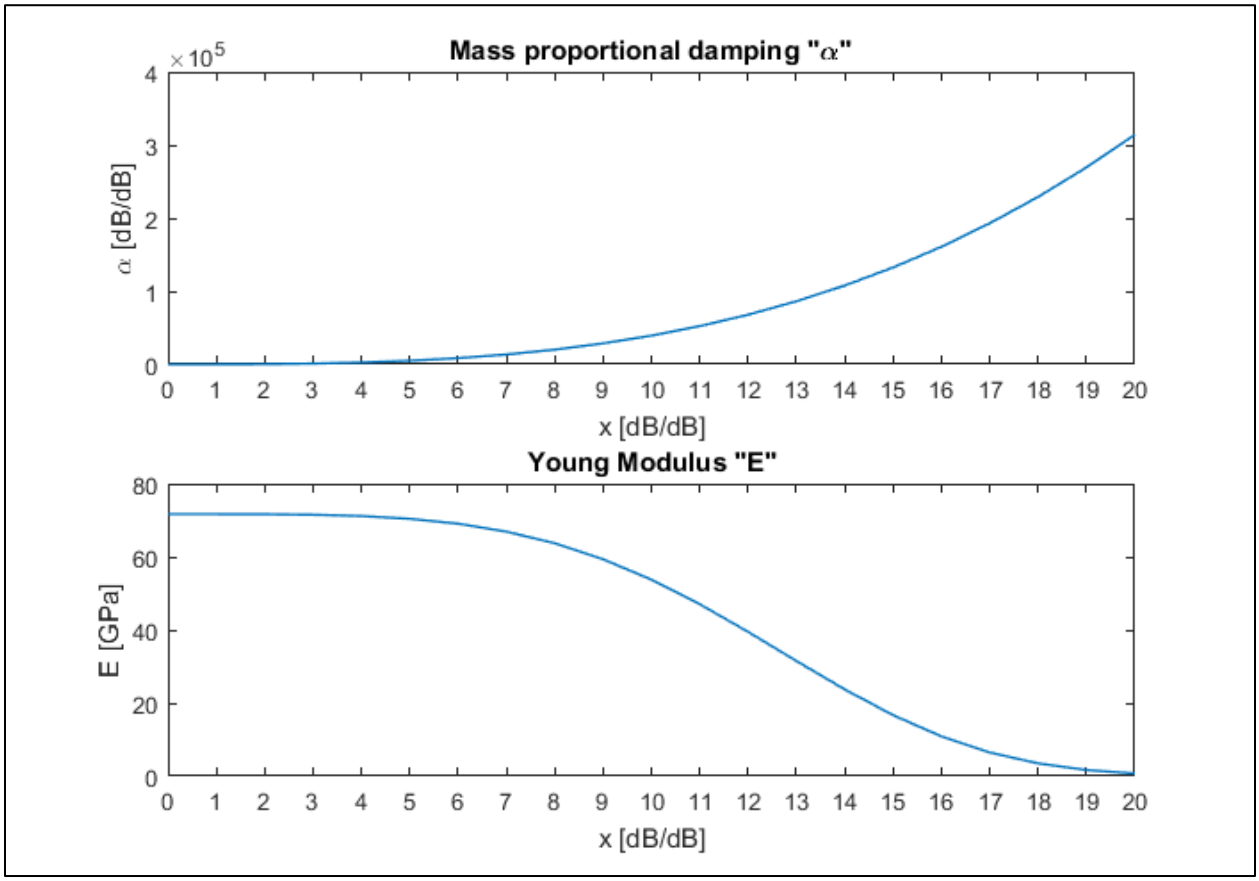

Figure 40 – Evolution of the α and E values from the plate edges to the end of the SRM region

Table 5 – Parameters used in the SRM region tuned for a 50 kHz signal

n	p	$\boldsymbol{\alpha_0}$	$\boldsymbol{\alpha_{max}}$	$\boldsymbol{E_0}$	$\boldsymbol{k_{inc}}$	$\boldsymbol{\sigma_{max}}$
20	3	0	$3.14 \cdot 10^5$	$71.7\ GPa$	$2.33 \cdot 10^3$	$1.98 \cdot 10^{-3}$

4.6.4 Methods performance

The choice of running four different simulation using a relatively low frequency of 50 kHz is related to the stability requirements. The same comparison could have been done at other frequencies, however the higher the frequency, the smaller is the mesh elements size and the time

step, leading to a consistent increase in the computational cost of the simulation. The sensor layout resembles the one used in the experimental setup, even if some changes are present. The frame of reference is positioned as shown in Figure 9 and the list of the new sensors coordinates is given by Table 6. Sensor 1 has been used as an actuator, while two extra transducers were positioned in the plate centerline (sensors 6 and 7) with the aim to gather further data useful in this phase of the study.

Table 6 – Sensor layout in the development of the absorbing boundaries numerical model

General	Coordinates [mm]		Coordinates [in.]	
Sensor	X	Y	X	Y
1	152.4	304.8	6	12
2	76.2	457.2	3	18
3	228.6	406.4	9	16
4	228.6	152.4	9	6
5	76.2	203.2	3	8
6	76.2	304.8	3	12
7	228.6	304.8	9	12

Table 1 can be taken as a reference for the sensors coordinates Figure 41 gives a first indication about the different methods performance. The top view shows clearly that the Infinite Element method, Figure 41 (b), does not absorb effectively the wave packets at the plate edges. The result is similar to the normal boundaries case, Figure 41 (a) and therefore is not satisfactory. On the other hand, the other two methods, show improved performance as shown in Figure 41 (c-d). Figure 42 shows the signal recorded at Sensor 2 in the four simulations. The red dashed lines represent the interval in which the received signal falls after the recording of the main wave packet, represented by a 5-cycle Hanning window at 50 kHz. The SRM Figure 41 (d) shows better performance than the simulation in which a constant proportional mass damping coefficient was used as shown in Figure 41 (c), with just the 3% of residual reflected waves against the 22% respectively.

Considering the aforementioned numerical results, the SRM was used in the subsequent part of this study.

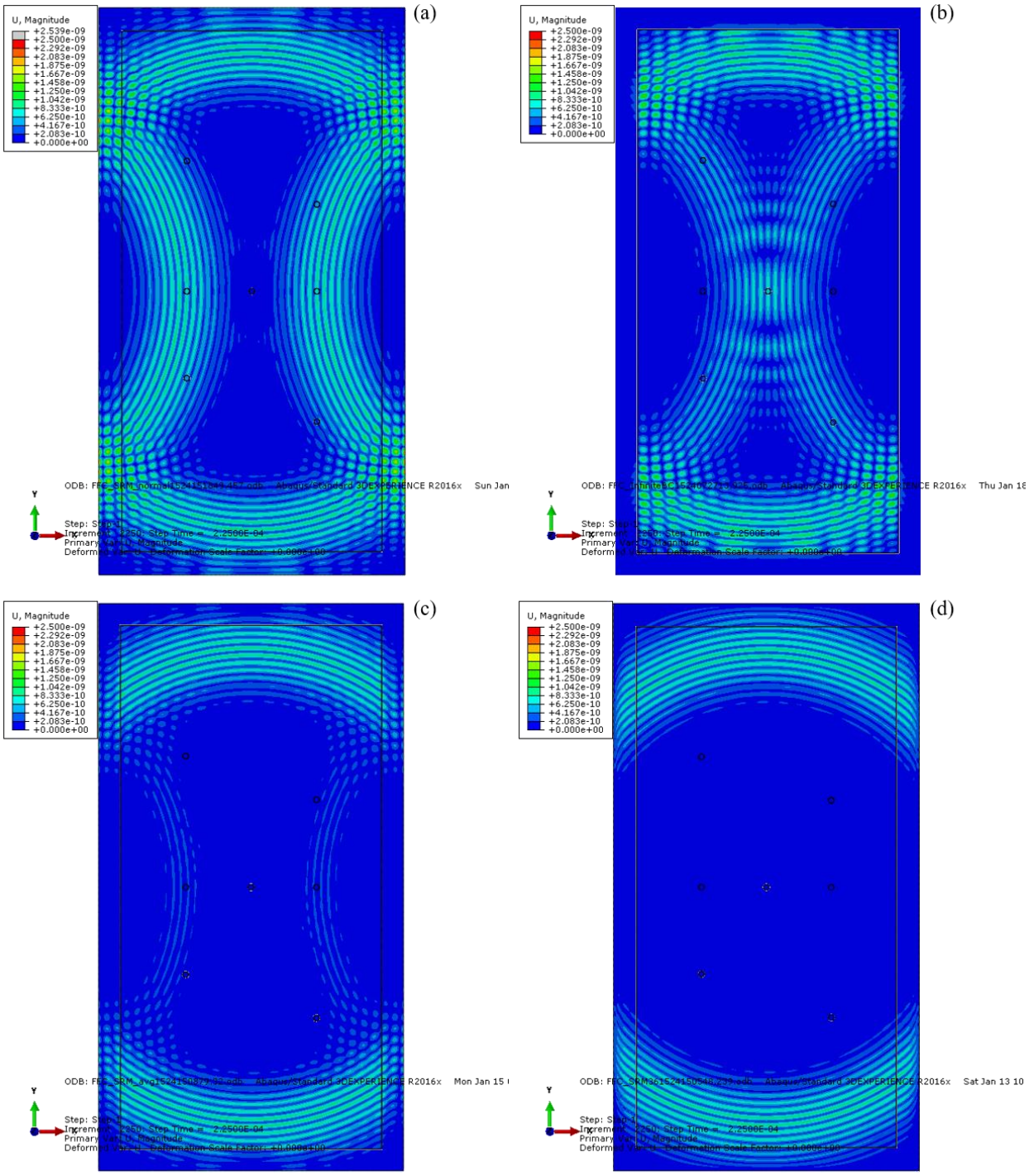

Figure 41 – Methods performance comparison - top view: Normal boundaries (a), Infinite Elements (b), Constant Rayleigh damping (c) and SRM boundaries (d).

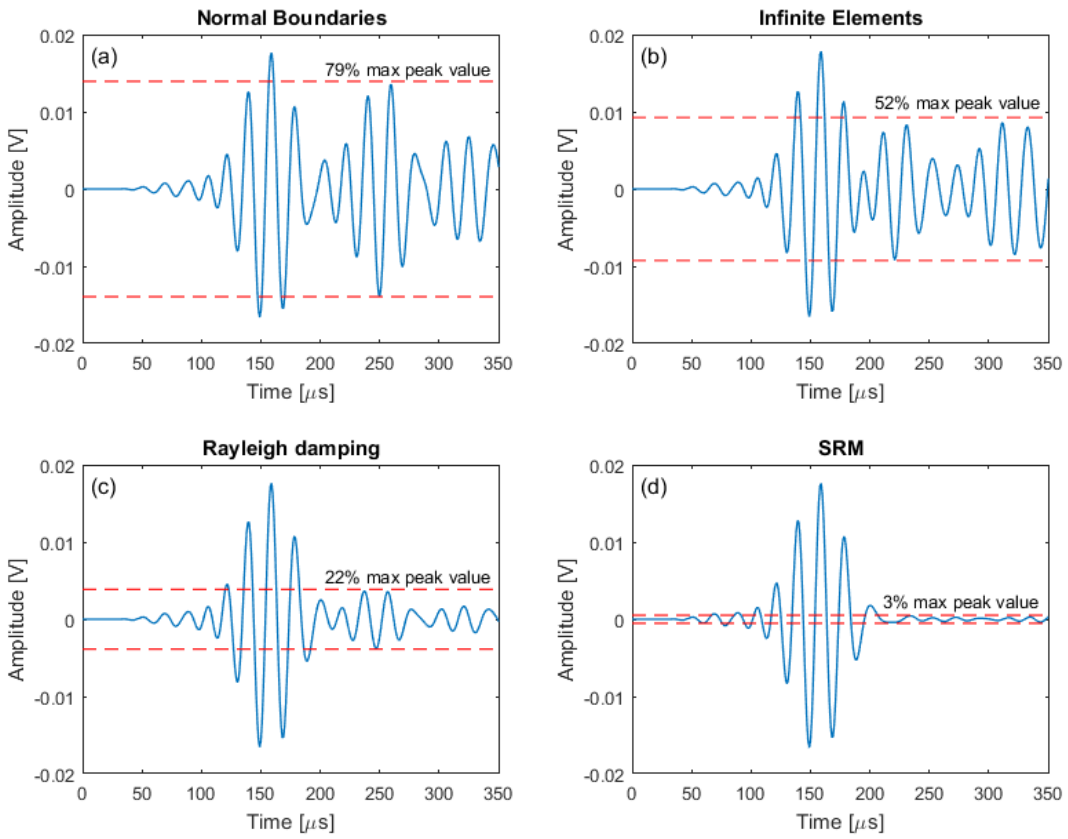

Figure 42 – Methods performance comparison - recorded signal at sensor 2: Normal boundaries (a), Infinite Elements (b), Constant Rayleigh damping (c) and SRM boundaries (d).

4.7 REDUCED MODEL SIZE

The implementation of absorbing boundaries opens the possibility to build a reduced model. This allows the user to refine the mesh and to decrease the time step without losing computational accuracy. Figure 43 represents the new configuration layout that was used in subsequent sections of this study. The area delimited by the dashed red line in the experimental setup, represented in Figure 43 (a), has the same area of the dashed red area in the numerical model Figure 43 (c). The sensors are placed according to Figure 43 (b). Sensor 5 in Figure 43 (c) has the same coordinates of the PLB test location in Figure 43 (a). The experimental setup makes use of Plasticine in order

to avoid undesired reflections coming from the boundaries while the numerical model uses the SRM developed in paragraph 4.6.3.

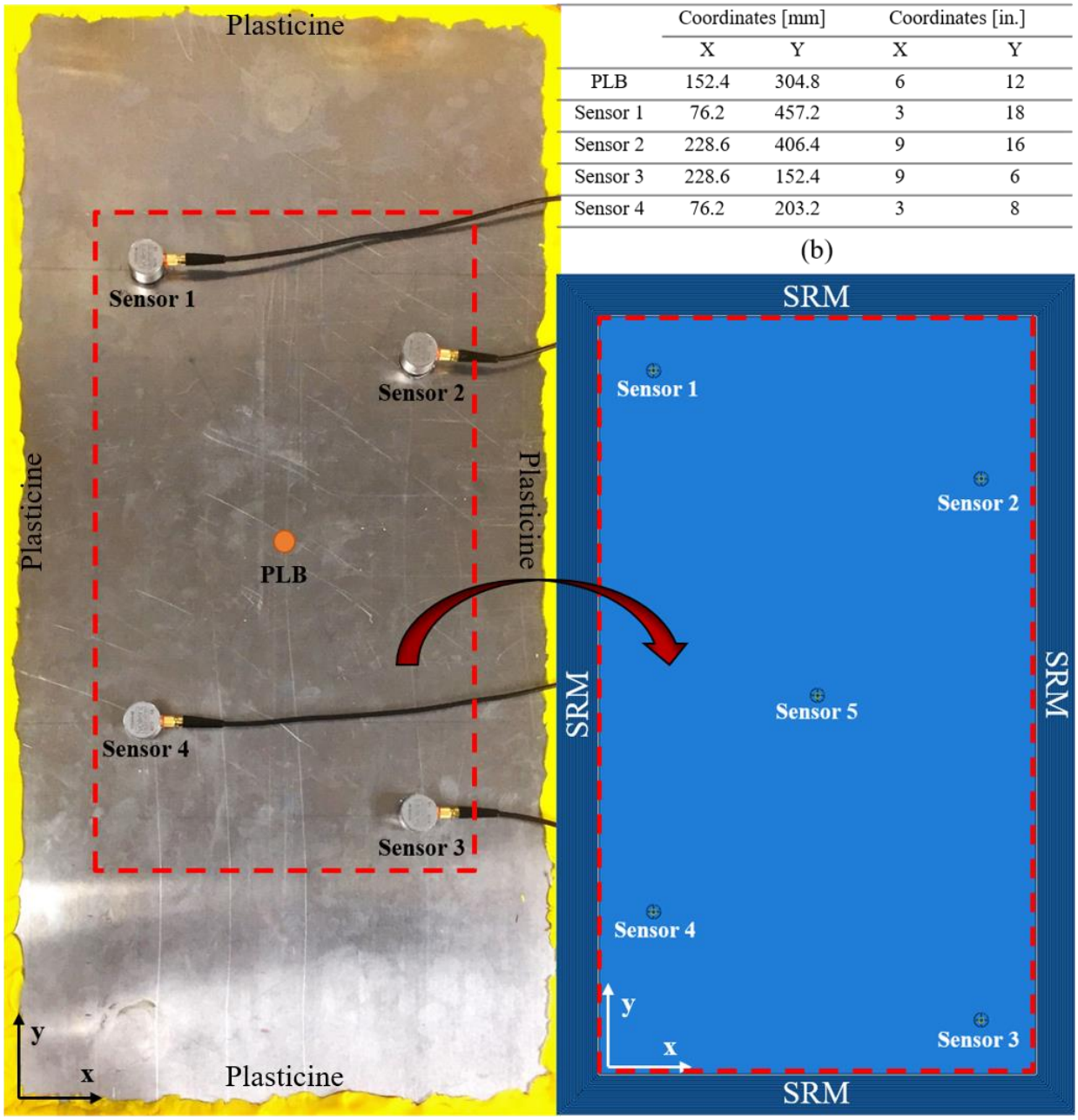

	Coordinates [mm]		Coordinates [in.]	
	X	Y	X	Y
PLB	152.4	304.8	6	12
Sensor 1	76.2	457.2	3	18
Sensor 2	228.6	406.4	9	16
Sensor 3	228.6	152.4	9	6
Sensor 4	76.2	203.2	3	8

(b)

Figure 43 - Sensor layout (a) experimental setup, (b) location, and (c) numerical setup.

4.8 SPEED OF SOUND WAVE ANALYSIS

The speed of sound is one of the crucial parameters in the Time Reversal process that will be addressed in Chapter 5. Therefore, the numerical model must show the right speed of the different modes in order to be considered representative of the experimental layout. However, this task hides difficulties related to determination of the TOA.

4.8.1 Determining the Time of Arrival

An ongoing challenge in the AE community is to find a methodology to determine the TOA of a wave mode in a clear and objective manner. Some researches use as reference the threshold of a certain value. Indeed, this is also the criterion used by the Vallen Systeme. Others refer to the maximum peak contained in the wave packet in an attempt to be more accurate. Nevertheless, those entire techniques leave margin for interpretations, especially if the signal is complicated, made by the superposition of more modes. This is common in the AE field, due to boundary reflections or the scattering due flaws inside the material. Even in simple geometries, as the flat plate considered in this project, it's not straightforward to determine with high accuracy the TOA if the sensor is located close to the AE source. Indeed, for short distances the symmetric and antisymmetric modes do not have enough time to develop, as previously mentioned and shown in Figure 35.

For the aforementioned reasons, there is the need for a new mathematical tool capable of detecting the arriving wave packet in an objective way.

4.8.2 The Phase Analysis technique

This section introduces the so-called "Phase Analysis technique". The author would like to thank the PhD candidate Maria Barroso Romero from Delft University of Technology for sharing her knowledge about this interesting topic. Without her precious support, this part of the research project would not have been possible.

This method aims at detecting the TOA of an incident wave packet analyzing the shift in the phase of its corresponding analytic signal. It seems worth to introduce a formal definition: a signal characterized by only positive frequency components is referred to as *analytic signal* [35].

Analytic signals are commonly held in the field of signal processing as tools for simplify mathematical operations. Every real valued signal, $x_r(t)$, as for example the one generated by a

piezoelectric transducer, has its corresponding analytic signal, $x_a(t)$, that can be expressed according to Equation (4.9) as:

$$x_a(t) = x_r(t) + jx_{HT}(t) \tag{4.9}$$

Where "j" is the imaginary unit and "$x_{HT}(t)$" denotes the Hilbert Transform applied to the original real signal as shown in Equation (4.10):

$$x_{HT}(t) = H[x_r(t)] \tag{4.10}$$

It can be demonstrated that $x_a(t)$ has no negative frequencies but this result is obtained without any loss of information because of the Hermitian symmetry property that characterizes the spectrum of real valued functions [36].Without providing further details, that would be outside the purposes of this thesis, it is possible to affirm that the envelope and the phase of the real signal, $x_r(t)$, can be computed by means of the magnitude and the argument of the analytic signal as stated by Equation (4.11) and Equation (4.12) respectively:

$$|x_a(t)| = \sqrt{x_r(t)^2 + x_{HT}(t)^2} \tag{4.11}$$

$$\phi = \frac{x_{HT}(t)}{x_r(t)} \tag{4.12}$$

The idea is to make use of the argument of the analytic signal as tool for the determination of the TOA. In particular, a discontinuity in the phase value is an indicator of the approaching wave packet that is characterized by a constant change in phase proportional to its central frequency.

4.8.3 Measuring the S_0 and A_0 group velocities

The dispersion curves, provided by the Vallen Systeme and shown in Figure 19, indicate that for a frequency of 130 kHz the S_0 and the A_0 modes are characterized by the group velocities outlined in Table 7:

Table 7 – Group Velocities at 130 kHz according to the analytical model

	S_0	A_0
c_g [m/s]	5341	2325

The phase analysis technique has been applied to measure the group velocities in a numerical simulation in which an Hanning window of 130 kHz was injected by Sensor 5 in the reduced size model with a maximum positive value of 10V. The SRM absorbing boundaries were tuned accordingly for 130 kHz. It has been decided to take as reference only the signals received at Sensor 1 and Sensor 2 since, for symmetry considerations, they have the same time of arrivals of Sensor 3 and Sensor 4.

In Figure 44 the received signal at Sensor 1 with its corresponding envelope is shown. A first estimation of the time of arrivals can be appraised considering the plot of Figure 44 leading to the values in Table 8:

Table 8 – TOA of the S_0 and A_0 modes at Sensor 1

	S_0	A_0
TOA [µs]	33	70

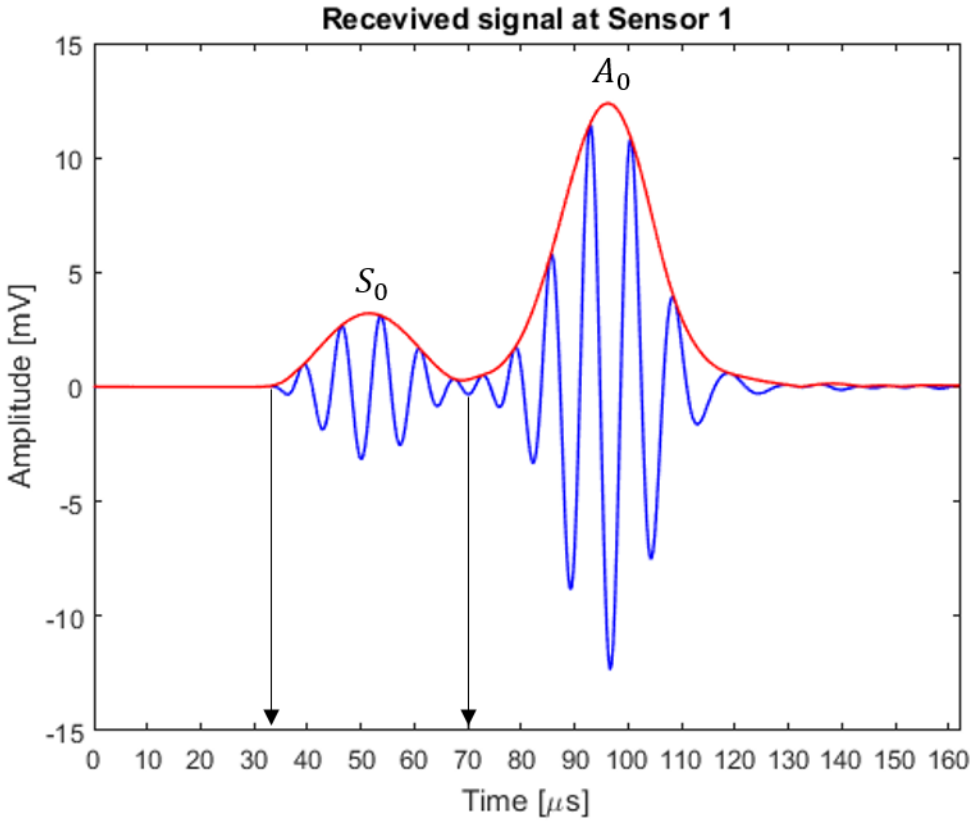

Figure 44 – Received signal at Sensor 1 with its envelope

Nevertheless, the choice it is still somehow arbitrary especially about the A_0 mode, which is affected by the last portion of the S_0 wave packet.

The situation is even more complicated looking at the signal received at Sensor 2, as depicted in Figure 45. The reason lies in the fact that Sensor 2 is closer to the actuator with respect Sensor 1 and, consequently, the two modes are still mixed. Therefore, only the S_0 TOA can be evaluated, as reported in Table 9:

Table 9 – TOA of the S_0 and A_0 modes at Sensor 2

	S_0	A_0
TOA [μs]	26	NaN

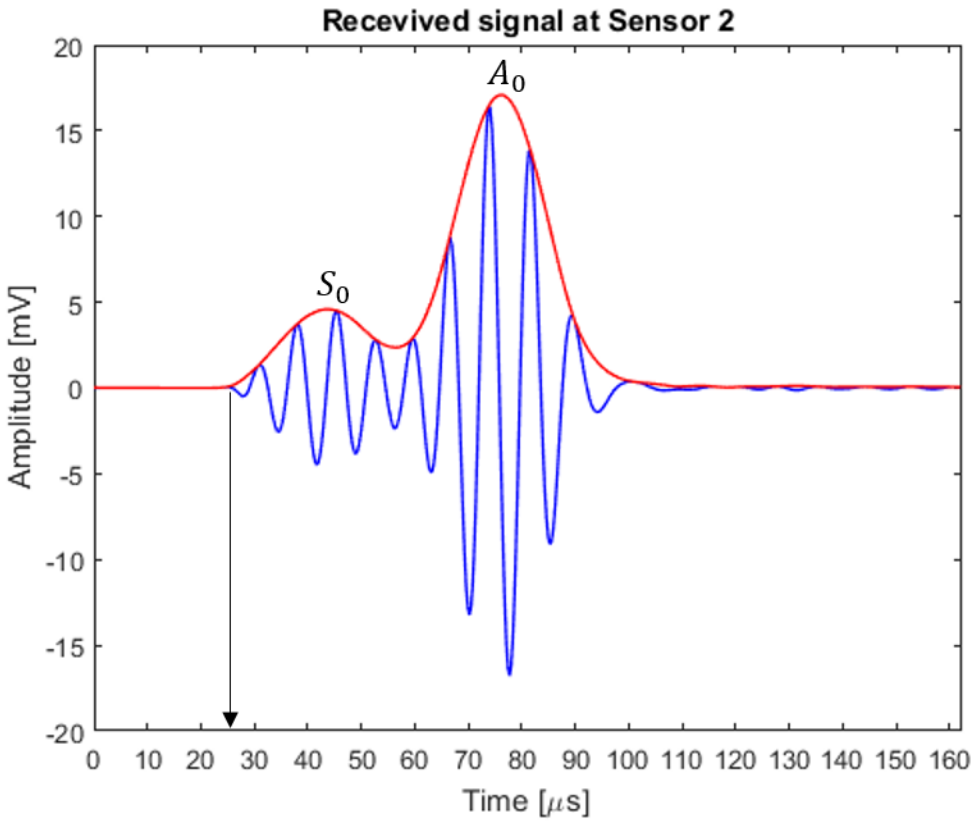

Figure 45 – Received signal at Sensor 2 with its envelope

The phase analysis technique is crucial at this point in order to clarify in an objective way the TOA.

In Figure 46 are plotted the unwrapped phase[5], ϕ_{uw}, of the received signal at Sensor 1, and the so-called "instantaneous frequency", $f_{inst}(t)$, which can be obtained taking the derivative of the unwrapped phase with respect time and dividing by 2π, as reported in Equation (4.13):

$$f_{inst}(t) = \frac{1}{2\pi}\left(\frac{d\phi_{uw}}{dt}\right) \tag{4.13}$$

A first change in phase is registered around 32 μs (Point A Figure 46), and this represents the TOA related to the symmetric mode. The A_0 can be recognized looking at the "little bump" present in the instantaneous phase, highlighted by the dotted red circle (Point B Figure 46).

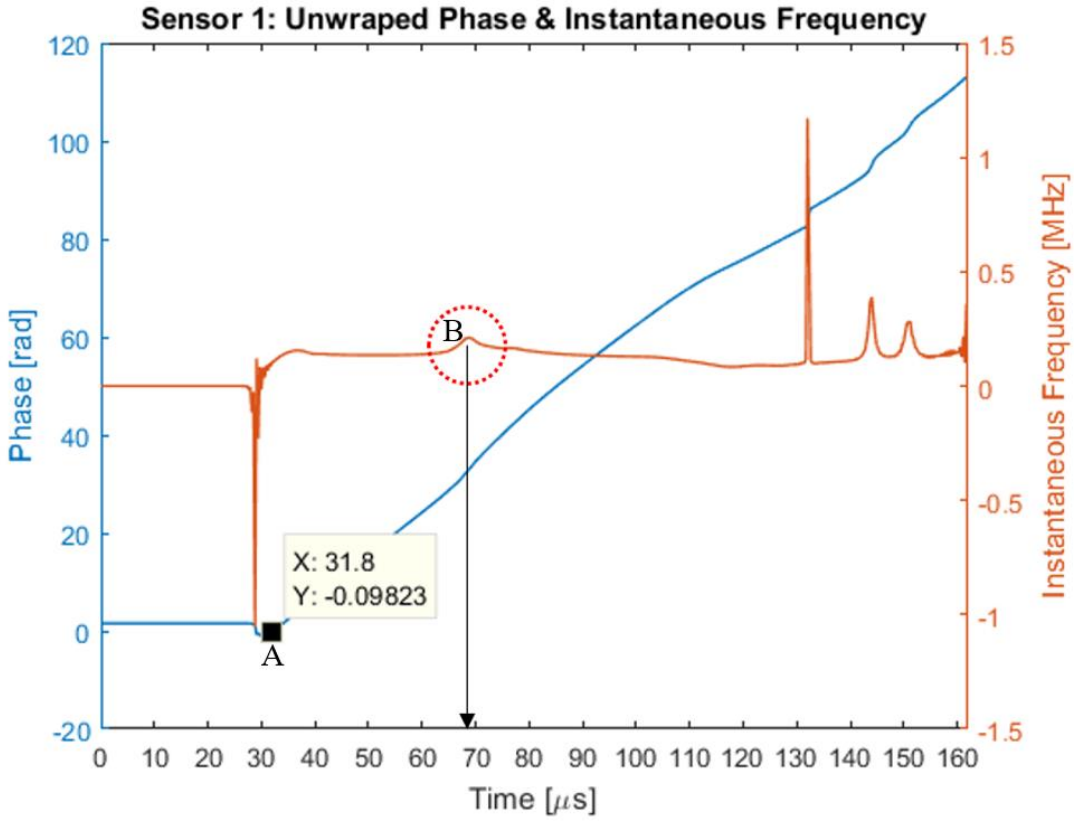

Figure 46 – Phase shift analysis of signal received at Sensor 1

[5] The unwrapping operation is performed by a Matlab™ command that substitutes phase values bigger than π with their 2π complement.

Analogously, Figure 47 shows the same kind of plot related to the wave signal recorded at Sensor 2. This kind of analysis is powerful but has to be used carefully. The S_0 mode for instance is easier to recognize by means of the phase plot because when the wave packet is approaching the instantaneous frequency is very sensitive. Indeed, it shows a deep-down peak when the symmetric mode which has not arrived yet or, more precisely, when a displacement of a negligible order of magnitude is present. Therefore, in this case, a correct analysis is done looking at the first instant in which the unwrapped phase graph shows a constant increasing rate, right after the instantaneous frequency down peak (Point C Figure 47). On the other hand, the antisymmetric mode is hard to detect by means of the change in slope of the phase plot and is convenient to use as reference the relative peak of the instantaneous frequency (Point D Figure 47).

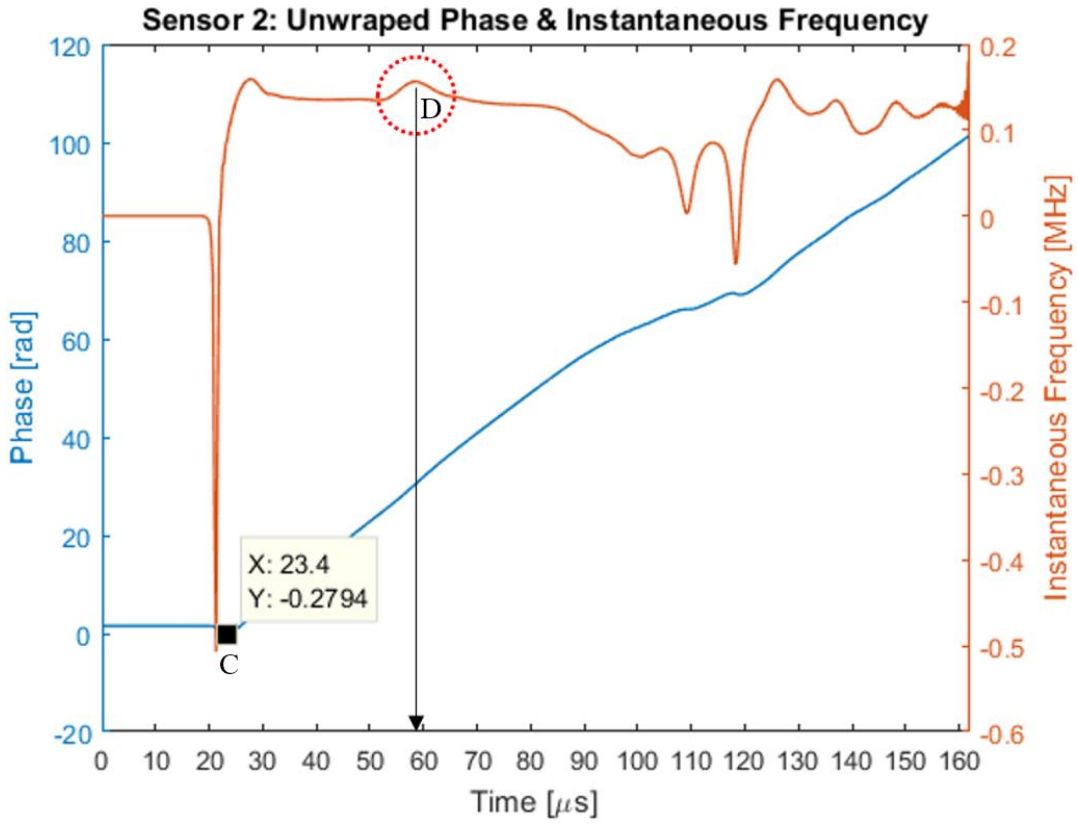

Figure 47 – Phase shift analysis of signal received at Sensor 2

Table 10 shows the collected data using the proposed methodology:

Table 10 – TOA of the symmetric and antisymmetric modes

Sensor	Mode	TOA [μs]	d [mm]	cg [m/s]
1	S_0	31.8	170.4	5358
	A_0	68.7	170.4	2480
2	S_0	23.4	127	5427
	A_0	59.1	127	2149

In Table 11 is carried out a comparison between the modes group velocities computed by means of the analytical model, represented by the dispersion curves (Figure 19) already discussed in paragraph 3.4.1.1, and the developed numerical model. The S_0 and A_0 group velocities are given by averaging the results recorded at Sensor 1 and Sensor 2.

Table 11 – Speed of sound analysis: computed group velocities

	Experimental		Analytical model		Numerical model	
	S_0	A_0	S_0	A_0	S_0	A_0
$\mathbf{c_g}$ [m/s]	5245	NaN	5341	2325	5393	2315

Finally, Table 12 compares the group velocities computed in the numerical model with respect to the analytical and experimental results reporting the corresponding relative errors.

Table 12 – Speed of sound analysis: relative error

% Error	Analytical model		Experimental	
	S_0	A_0	S_0	A_0
Numerical model	0.97	-0.45	2.82	NaN

The results are promising, with a nice matching, below the 1% relative error, between the numerical simulation and the theoretical approach. The comparison with the experimental data is possible only referring to the S_0. The relative error is below the 3%, demonstrating once again the consistency of the developed numerical model. This little discrepancy can be justified considering

that in the experiments a PLB test was used instead of an Hanning window function. The spectra of the two signals are similar, since for our setup the PLB has the same main frequency of an Hanning window at 130 kHz, but not identical. This highlights the issues that arise when researchers try to correlate the numerical world with the experimental one. The goal of this project is to find a representative signal of a PLB test in order to be finally able to compare, in the proper way, experimental with numerical data.

CHAPTER 5

5 TIME REVERSAL METHOD

In the specific case of a central frequency signal, Time Reversal (TR) has been used to reconstruct the original emission. R.K. Ing and M. Fink studied for the first time the behavior of time-reversed Lamb waves in the context of Non-Destructive Testing (NDT). Their research highlighted the capability of the TR method to automatically compensate for the dispersive nature of Lamb waves [37]. Further studies emphasized the potential of time reversal of acoustic waves for the production of a statistical damage classifier capable of identifying delamination in composite plates without any available baseline data [38].

In 2003, CH Wang et al., addressed the problem of the TR process between two piezoelectric transducers using a generic signal [39]. A theoretical approach, based on the Mindlin plate theory [40], was developed introducing the time reversal operator. It was shown that the time reversal operator is frequency dependent. If the signal spectrum is not uniformly scaled, the reconstruction of the original excitation is compromised. So far, the TR approach has been only used with narrowband waveforms in order to lessen the frequency dependency [41].

5.1 APPLICATION TO A NARROWBAND SIGNAL (HANNING WINDOW)

As a first step, it was decided to apply the TR technique to a Hanning window function, in order to verify the effectiveness of the proposed methodology. In particular, the signal used for the speed of sound computation in paragraph 4.8.3 has been time-reversed and reconstructed in the central actuator. The adopted scheme is shown in Figure 48. The TR methodology is applied to all the four sensors but, for the sake of simplicity, Figure 48 shows only the process related to the PZT 2. The sensors layout is the same outlined in Figure 43, where the word Sensor is replaced with the acronym PZT and Sensor 5 is indicated as PZT A.

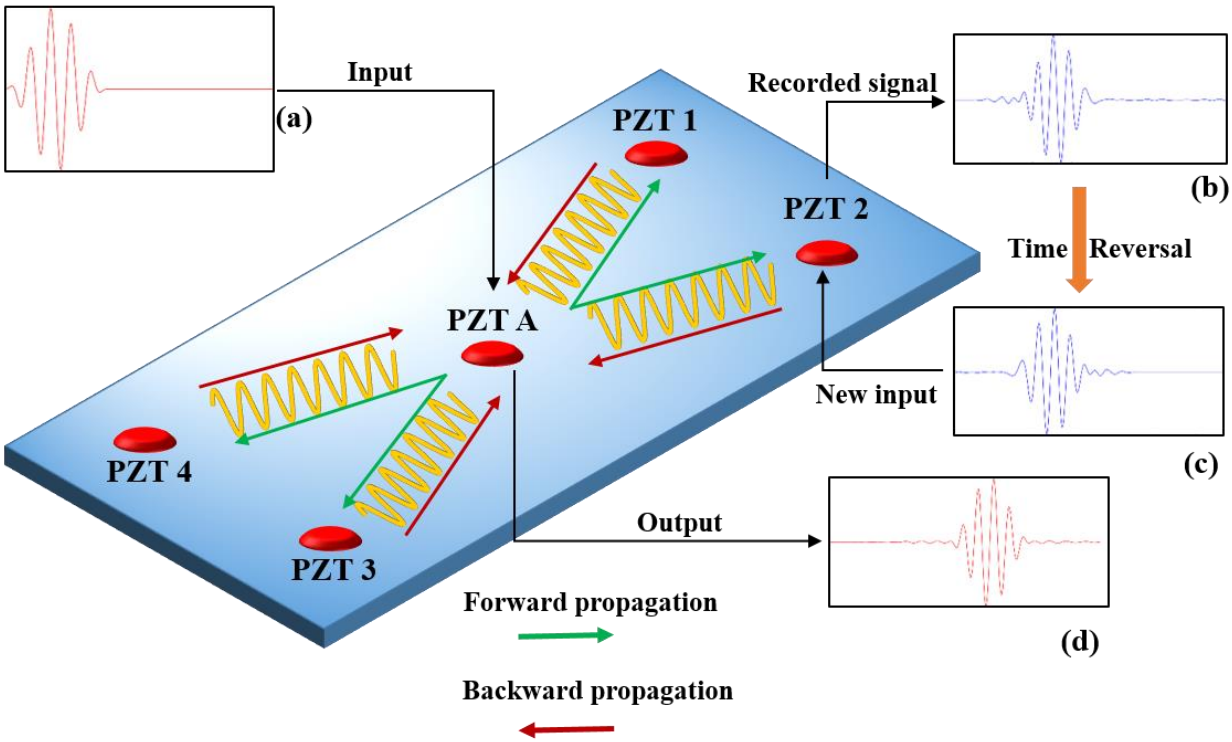

Figure 48 – Time Reversal schematic applied to a narrowband signal

The 5 cycles Hanning window function is transmitted in the Aluminum plate Figure 48 (a), recorded in the four piezoelectric sensors (b), time-reversed (c) and reconstructed at PZT A (d).

The results of the simulation are presented in Figure 49, where the steps from (a) to (d) coincide with the ones shown in Figure 48. Steps (e) and (f) are used in order to compare the reconstructed signal with the original one at step (a). More precisely, in (e) the reconstructed signal is time-reversed and in (f) is plotted against the original one.

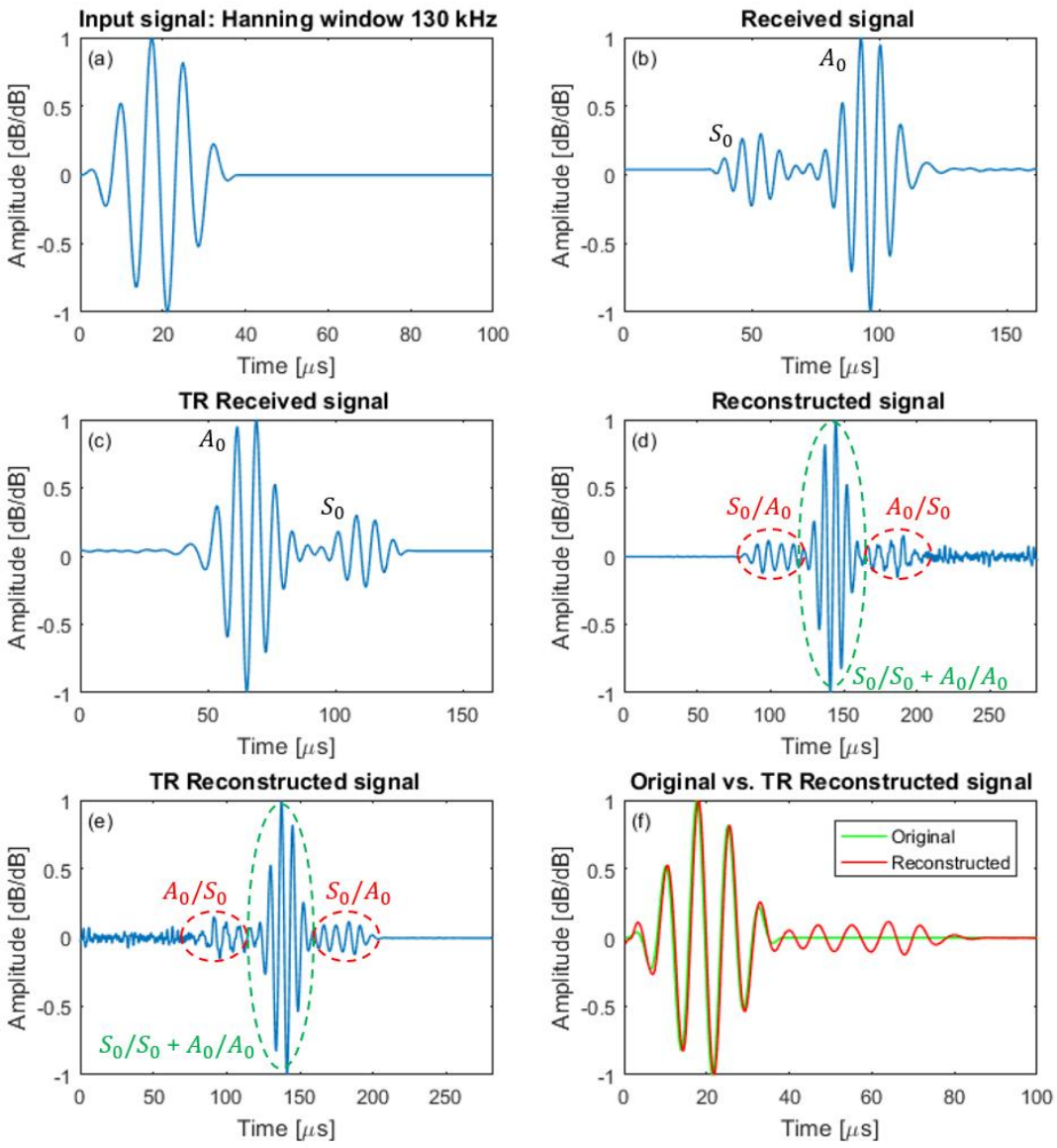

Figure 49 – TR process applied to a 130 kHz Hanning window (PZT A – PZT 1 were taken as reference)

A preliminary discussion regarding the mode decomposition phenomenon is required to explain the extra wave packets around the reconstructed signal at step (d). H.W. Park et al. addressed this topic in reference considering the Time Reversal process applied between two piezoelectric transducers [42]. The same concept can be applied between PZT A and PZT 1. It was decided to use as reference the PZT 1, and not the PZT 2 as in the schematic of Figure 48, because it is farther from PZT A and therefore this choice allows the S_0 mode to separate enough from the A_0, providing

a clear picture of the phenomenon. Nevertheless, this example can be applied also for the other three sensors, without losing of generality.

In the first step (a), the symmetric and antisymmetric modes are coexisting simultaneously in the original wave packet. In Figure 49 (b), the received signal shows the S_0 arriving first, followed by the A_0. This phenomenon comes from the theory of Lamb wave generation. Every time a wave is generated, an S_0 and an A_0 are produced at the same time. Even if there are specific frequencies in which it is possible to excite mainly one mode [43], it is still not possible to produce one mode alone, without the generation of other modes at the same time. Therefore, applying the Time Reversal process to Lamb waves is much more complicated with respect other fields, such as submarines and gallstones localization [44], due to mode decomposition. Thus, when moving from step (c) to step (d), the A_0 packet is transmitted back first and it generates an S_0 and an A_0. Analogously, when the S_0 mode is sent back towards PZT A, it produces again an S_0 and an A_0 modes. As a matter of fact, in Figure 49 (d) or (e), the script S_0/A_0 designates the S_0 mode generated by the A_0 and vice versa with A_0/S_0. The central segment of the wave packet, made by the sum of S_0/S_0 (S_0 mode generated by the S_0) and A_0/A_0 (A_0 mode generated by the A_0) can be considered a scaled version of the original signal and, therefore, is the that is representative of the initial AE source [42]. It is interesting to note that, normalizing the signals, it is possible to fully reconstruct the original emitted wave shape, as reported in Figure 49 (f). Normalization is also useful to compare numerical results with experimental data, affected by sensor sensitivity.

The original signal and the time-reversed signal reconstructed at PZT A where put in phase with respect to each other using a cross-correlation function in Matlab™. Figure 50 shows the cross-correlation function between the original signal at step (a) and the one in step (e) of the previous Figure 49. The time corresponding to the peak of this function has been used to shift the two signals such as they were in phase. Moreover, the peak value is an indicator of the similarity between the two signals. In this case, the correlation coefficient reached a value of 0.97, that is an important achievement considering that it reaches the value of 1 when two signals are identical.

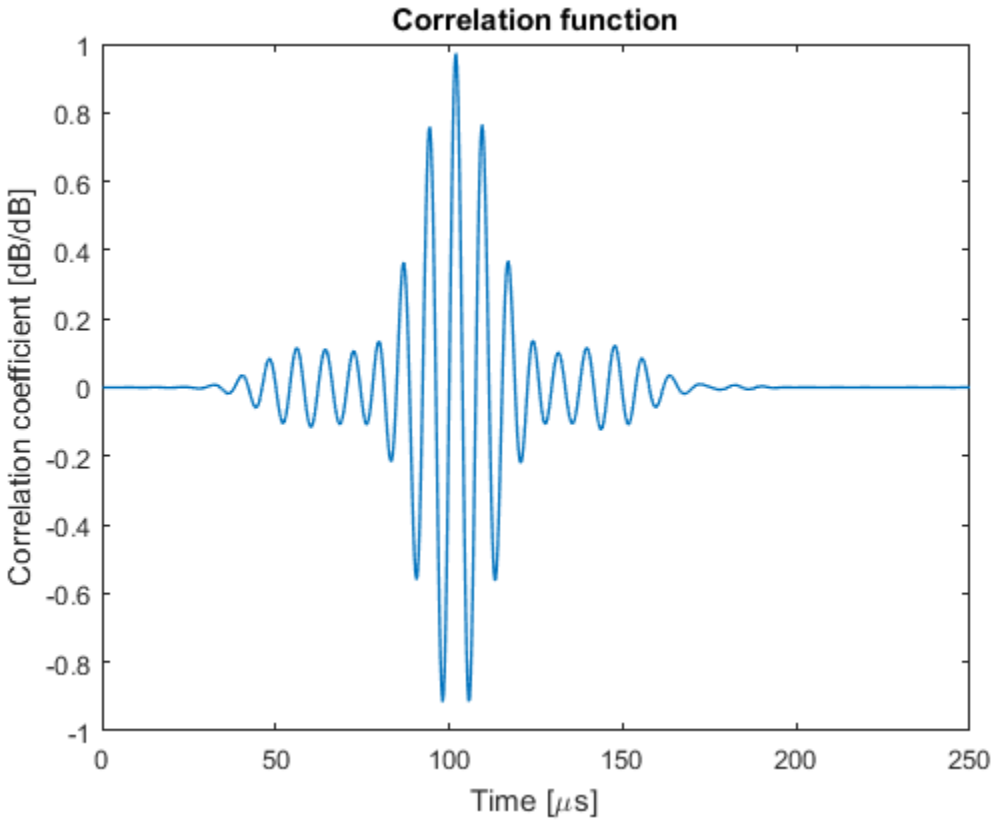

Figure 50 – Cross correlation function between the original and the reconstructed signals

Finally, it is presented in Figure 51 the top view of the TR process regarding the aforementioned simulation with six frames equally spaced in time (every 15 μs). The sequence shows how the wave packets converge simultaneously at the central actuator with a high level of accuracy in addition to the SRM boundaries preventing undesired reflections.

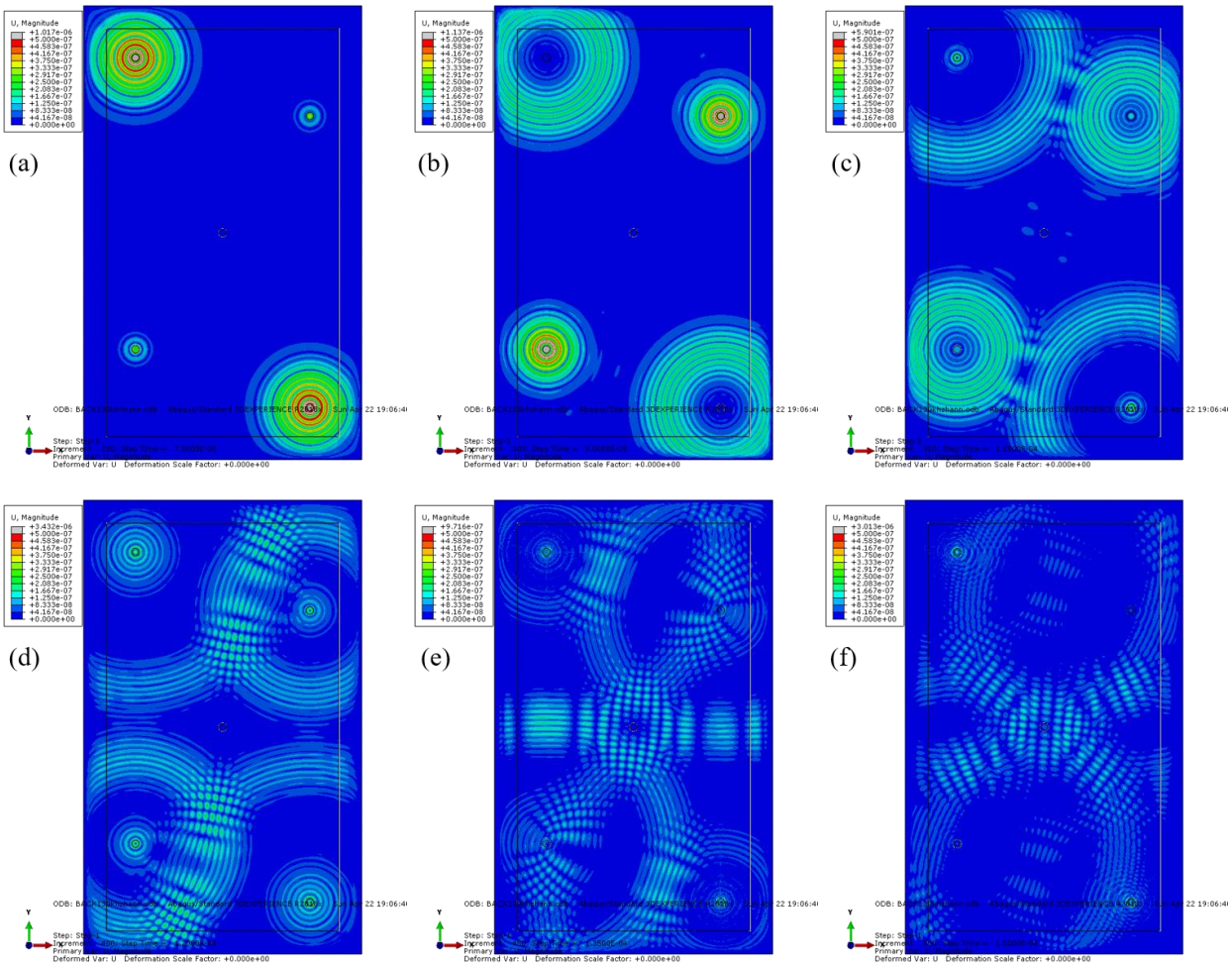

Figure 51 – Top view at different frames of the Time Reversal process

The challenge, at this point of the study, was to apply the same methodology to a broadband signal. Indeed, in the real world, AE generated by crack growth or other failure mechanisms of interest are broadband signals. In particular, the goal was to be able to successfully reconstruct a PLB signal, easy to replicate experimentally, and representative of a real AE at the same time.

5.2 METHODOLOGY FOR THE DERIVATION OF THE TRANSFER FUNCTION

As stated in the introduction section of Chapter 5, is not possible to reconstruct the original emitted source when the Time Reversal method is applied to signals with multiple frequency components. This issue, connected with the TR process, significantly limited the spreading of this technique in the AE community. In this thesis, the use of a transfer function, which is representative of the

plate-sensor system that accounts for frequency dependency, is considered. The methodology followed in this study is outlined in Figure 52. The scheme is the same of Figure 48 but in this case the input is a band-limited with noise (BLWN) function. By definition, a BLWN signal has the energy uniformly distributed in all the frequency range inside the considered band. Therefore, studying the change in the spectrum of the BLWN signal can give important insights about the modulation of the different frequency components.

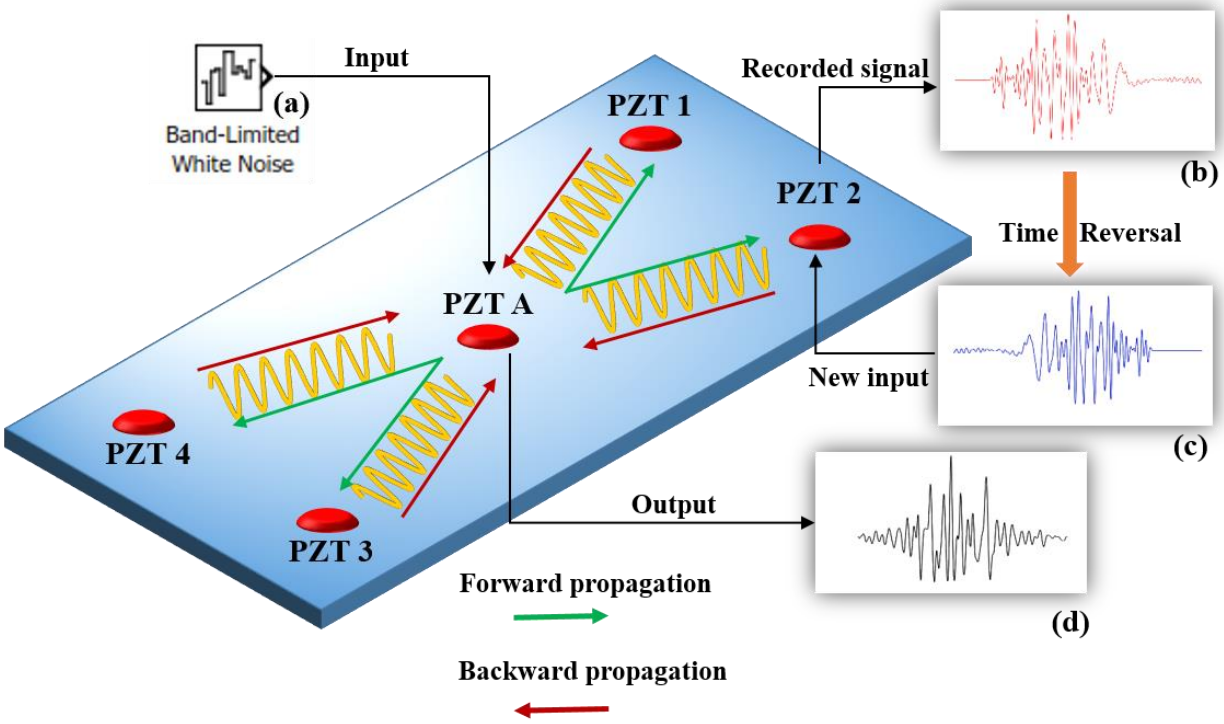

Figure 52 – Methodology used to derive the transfer function

The derivation of the transfer function, described in Figure 52, is performed by: (a) generating a band-limited white noise signal from the central actuator – Lead Zirconate Titanate (PZT) A, (b) recording it at the four sensors (PZT 1 to 4), (c) time reversing it at all four sensors and sending it back again toward the actuator, and (d) reconstruction of the original signal at PZT A. The frequency spectra of the original band-limited white noise signal, Figure 52 (a), and the time-reversed version of the output, Figure 52 (b), are compared using Fourier transforms. Consequently, the system transfer function is obtained by means of the ratio between the original and the time-reversed spectra. This transfer function provides information on which frequencies

of the signals are amplified and which are decreased for the specific structure/sensor configuration during the TR process.

Assuming a mechanical-electro-efficiency close to one, implying a perfect reversibility of the TR process, the voltage response at sensor PZT 2, $V_2(t)$, produced by the injected band-limited white noise signal at PZT A, $V(t)$, is given by Equation (5.1):

$$V_2(t) = IFFT\left(\hat{V}(\omega) \cdot G(\omega)\right) \tag{5.1}$$

Where, the IFFT symbolizes the Inverse Fast Fourier Transform operation, $\hat{V}(\omega)$ is the input signal represented in the frequency domain, and the term $G(\omega)$ represents a frequency dependent transfer function for the forward propagation from the central actuator to PZT 2, as shown in Figure 52 (b) [45]. A similar voltage function can be derived for PZT 1, 3, and 4. As a follow on step, the recorded signal in the time domain is time-reversed, hence obtaining $V_2(T-t)$, as shown in Figure 52 (c). This operation is equivalent to taking the complex conjugate of the Fourier transform of the signal in the frequency domain [41], as described by Equation (5.2):

$$V_2(T-t) = IFFT\left(\hat{V}^*(\omega) \cdot G^*(\omega)\right) \tag{5.2}$$

Where the superscript (*) represents a complex conjugate. The reversed signal becomes the new voltage input applied at sensor PZT 2, and re-transmitted back to the PZT A. The output of PZT A is then represented by Equation (5.3), where $G(\omega)$ is assumed to be directional independent.

$$V_A(t) = IFFT\left(\hat{V}^*(\omega) \cdot G^*(\omega) \cdot G(\omega)\right) \tag{5.3}$$

The original input $V(t)$, applied to the system at the central actuator, must be equal to the time-reversed signal obtained in Equation (5.3), as shown by Equation (5.4), where $V_A(T-t)$ represents the time-reversed signal at PZT A:

$$V(t) = V_A(T-t) = IFFT\left(\hat{V}(\omega) \cdot G^*(\omega) \cdot G(\omega)\right) \tag{5.4}$$

In the case of a Hanning-windowed signal, characterized by a single frequency, the product $G^*(\omega) \cdot G(\omega)$, shown in Equation (5.4), becomes a constant and therefore the reconstructed signal is a scaled version of the original signal. However, in this study the Hsu-Nielsen source analyzed is a broadband signal. Therefore, the product $G^*(\omega) \cdot G(\omega)$ is unknown and the reconstructed signal will be a distorted version of the original one, since each frequency component is scaled at different magnitudes.

The system transfer function, given by the product $G^*(\omega) \cdot G(\omega)$, is computed through a numerical simulation, in which the original input signal $V(t)$ is a known band-limited white noise that has its energy evenly distributed along the considered range of frequencies. Applying the Fourier transform to both sides of Equation (5.4), one obtains:

$$\hat{V}_A{}^*(\omega) = \hat{V}(\omega) \cdot G^*(\omega) \cdot G(\omega) \tag{5.5}$$

The time reversal operator $G^*(\omega) \cdot G(\omega)$ can be obtained by means of the ratio between the spectrum of the reconstructed and time-reversed (TR) signal at the central transducer $\hat{V}_A{}^*(\omega)$, and the spectrum of the original band-limited white noise signal $\hat{V}(\omega)$, leading to:

$$G^*(\omega) \cdot G(\omega) = \frac{\hat{V}_A{}^*(\omega)}{\hat{V}(\omega)} \tag{5.6}$$

The same transfer function can be obtained from different independent simulation and is valid for that particular sensor configuration and plate specimen.

In the case of a broadband signal to be determined, as the PLB as input function, the term $V(t)$ is replaced by the unknown signal $V_{PLB}(t)$ and $\hat{V}_A{}^*(\omega)$ becomes the TR response to the PLB. This translates into a time-domain voltage signal of the PLB as:

$$V_{PLB}(t) = IFFT\left(\frac{\hat{V}_A{}^*(\omega)}{G^*(\omega) \cdot G(\omega)}\right) \tag{5.7}$$

Where now the product $G^*(\omega) \cdot G(\omega)$, the transfer function for the given layout, is a known term.

The proposed methodology can be applied for the reconstruction of broadband signals and, consequently, for the characterization of the PLB signal. In the next paragraph, details and results regarding the derivation of the time reversal operator and the reconstruction of a broadband signal will be given.

5.3 BAND-LIMITED WHITE NOISE SIGNAL SIMULATION

The white noise was generated using a Matlab™ code with a mean value $\mu = 0$ and a standard deviation $\sigma = 0.1$. The signal length was of 50 μs and was normalized within the interval [-1,1]. In the experimental setup, the PLB spectrum was found to have the most of its energy in the range from 50 kHz to 400 kHz. Therefore, a 6th-order Butterworth low-pass filter of 400 kHz was applied to the previously generated white noise. The BLWN signal was then imposed as an electric potential boundary condition at the top surface of PZT A, with a maximum positive value of 10 V.

Using the methodology developed in paragraph 5.2, the system transfer function $G^*(\omega) \cdot G(\omega)$ was derived. The obtained vector was interpolated in Matlab™ using a 7th-order polynomial function. Figure 53 shows the interpolated function in the range of interest up to 400 kHz. As seen in the same figure, the frequency ranges of the system that appear amplified (above 1), and appear reduced (below 1), are indicated by the crossing of the dashed red line in correspondence of 1.

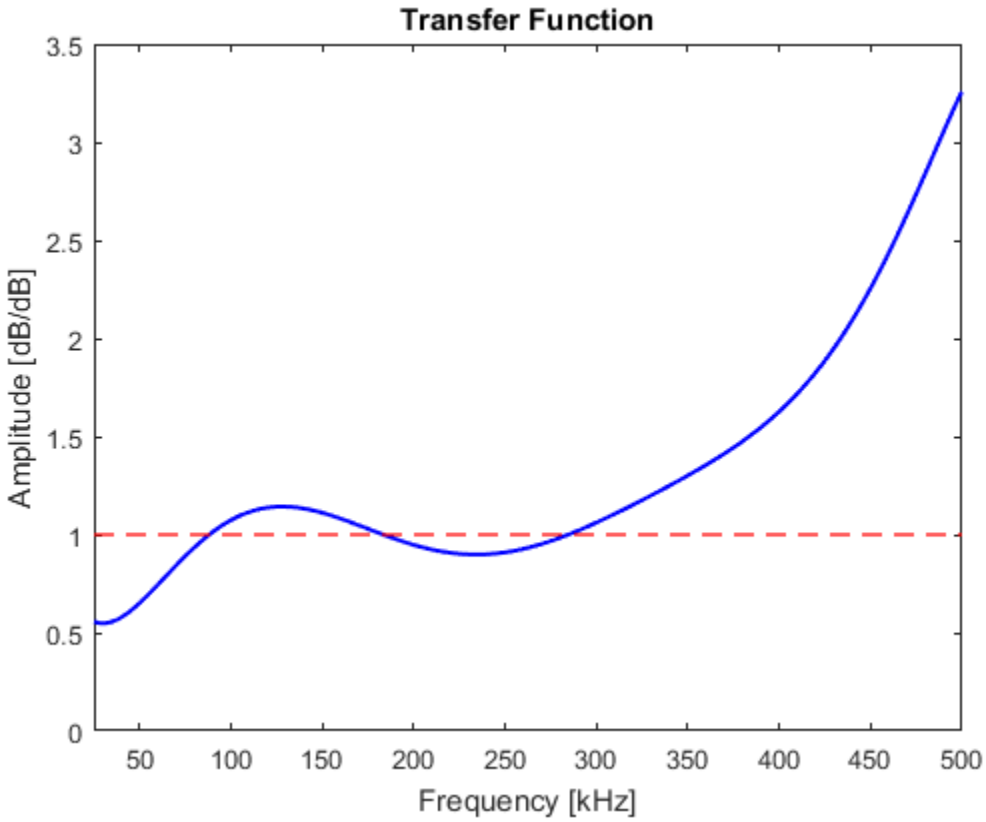

Figure 53 – System transfer function in the frequency range of 0-400 kHz

5.3.1 SRM applied to a broadband signal

The absorbing boundaries were tuned for a specific frequency of 130 kHz using the methodology applied in paragraph 4.6.3. Their performance with broadband signals has not been investigated in the literature yet. Nevertheless, in the BLWN signal simulation, the amount of reflections coming from the boundaries was found negligible, without compromising the derivation of the system transfer function. In Figure 54 it is reported the so-called spectrogram of the received signal at PZT 2, representing the power spectral density at different frequencies. Before 20 µs, no energy is present because the wave packet has not arrived at PZT 2. In the range between 20 µs and 120 µs, the BLWN signal is recorded. Is interesting to observe that, even if the BLWN signal has its energy in the range 0-400 kHz, PZT 2 is registering a significant amount of energy at higher frequencies. This can be explained considering the system transfer function in Figure 53. As such, frequency components higher than 300 kHz are significantly amplified. In the range 120-140 µs the wave

packet fully passed through the transducer. Finally, from 140 µs to the end of the simulations, reflections coming from the boundaries reach the sensor. As previously said, the amount of energy contained in the Lamb waves reflected from the edges is relatively low. This demonstrates that even if the SRM needs to be tuned for a specific frequency, it has sufficiently good performances even in the case of a broadband signal.

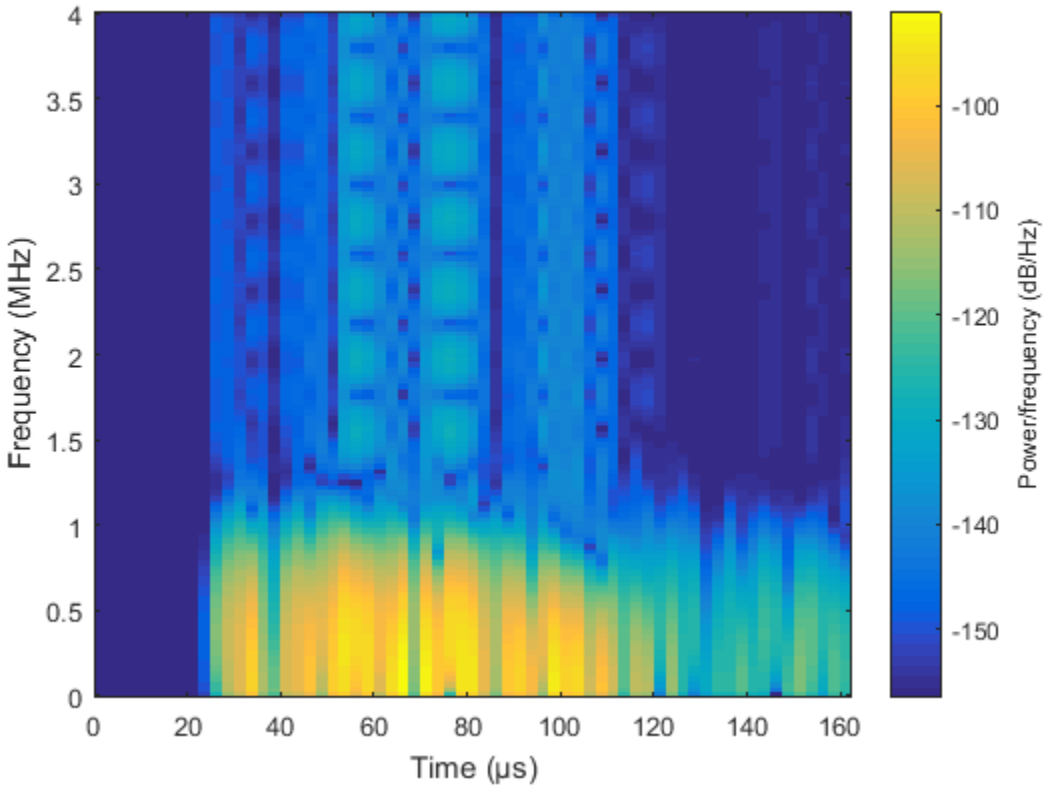

Figure 54 – Spectrogram of the received BLWN signal at PZT 2

5.4 BROADBAND SIGNAL SIMULATION

In this part of the research project, the aim was to reconstruct, with a sufficient level of accuracy, a broadband signal making use of the previously derived transfer function (see Figure 53). Figure 55, shows the spectrum of the AE to be reproduced, with frequency components in the range 0-400 kHz.

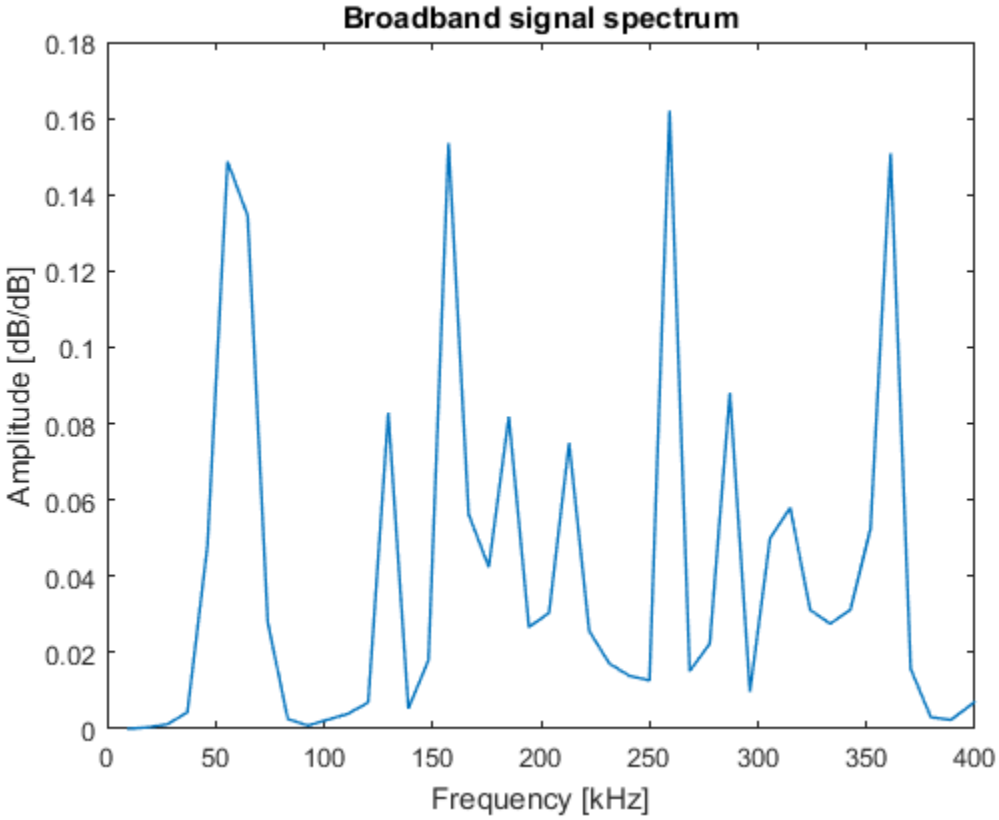

Figure 55 – Broadband signal spectrum

The procedure is the same described in the scheme of Figure 48 but with one more step after (d). Hence, the signal transfer function, $G^*(\omega)G(\omega)$, is applied to the time-reversed version of the reconstructed signal at step (d), in the frequency domain. The broadband signal is derived according to Equation (5.7), where the term $V_{PLB}(t)$ is replaced by $V_{BB}(t)$, symbolizing a time-domain voltage signal representative of the original broadband emission.

The results are shown in Figure 56, that compares the original signal with reconstructed one before (a), and after (b), the application of the derived transfer function. From a first analysis, it is possible to appreciate the effectiveness of the proposed methodology, with a significant improvement of the reconstructed signal moving from Figure 56 (a) to Figure 56 (b). Moreover, this result is also confirmed by the correlation coefficient, denoted in the same figure as "r". It is possible to make two important observations. First, even without the transfer function application, the reconstructed signal is not completely different with respect the original one. As such, they have many features

even if the reconstruction cannot reach high levels of accuracy. Secondly, using the proposed methodology, it is possible to compensate the distortion of the different frequency components.

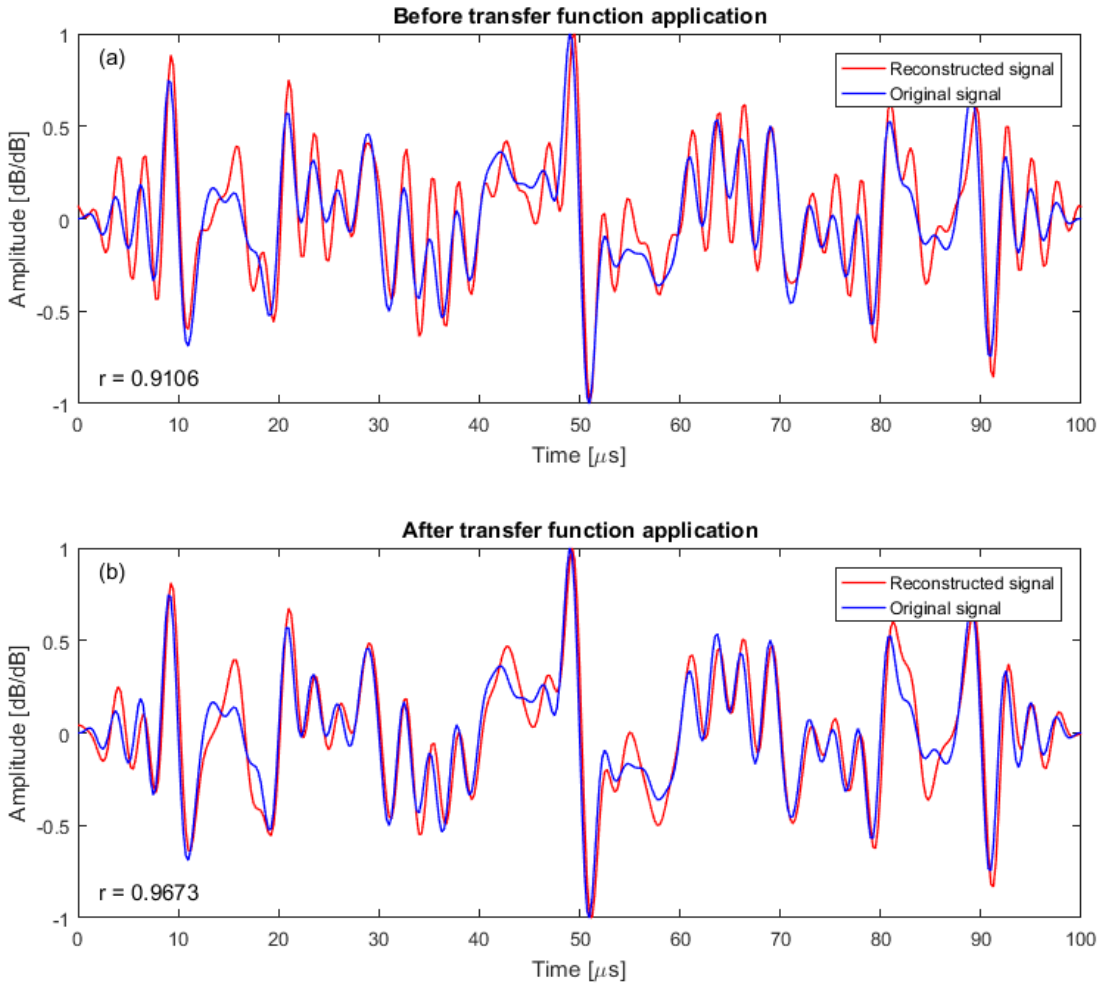

Figure 56 – TR process applied to a broadband signal with the use of the transfer function

CHAPTER 6

6 RECONSTRUCTION OF THE PLB SIGNAL

The Time Reversal method has been applied for the reconstruction of a broadband signals by means of numerical simulations. The consistency of the model has been verified in section 4.8. Chapter 6 aims to apply the same technique to reconstruct a real Pencil Lead Break emission.

6.1 THE EXPERIMENT

The used experimental layout is the one represented by Figure 43 (a). In order to obtain a representative PLB signal, ten tests were performed at the same location, referring to the coordinates given by Figure 43 (b). Moreover, the same pencil lead (0.3 mm – 2H) and angle with respect to the plate (45 deg) were used. In Figure 57, the signals recorded at PZT 2 are plotted together. The results confirm the repeatability of the Hsu-Nielsen AE source. Indeed, the signals show similar amplitudes and features.

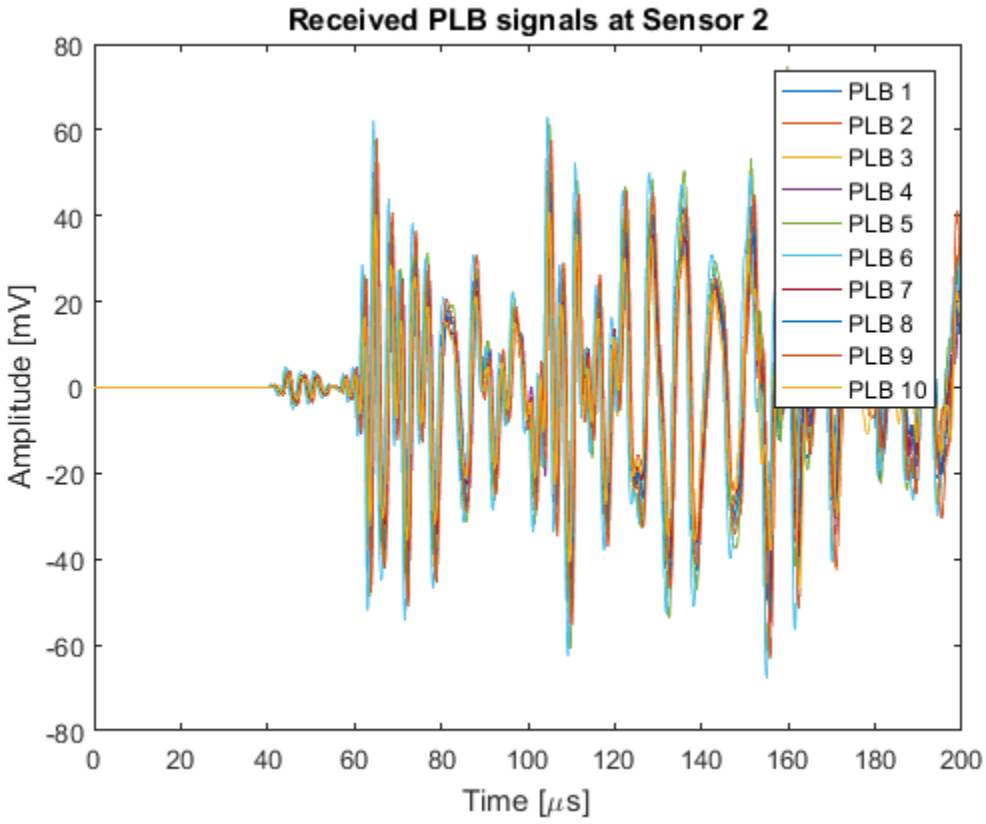

Figure 57 – PLB emissions recorded by PZT 2

Nevertheless, some of them are not perfectly in phase with respect each other as shown in the zoom view of Figure 58.

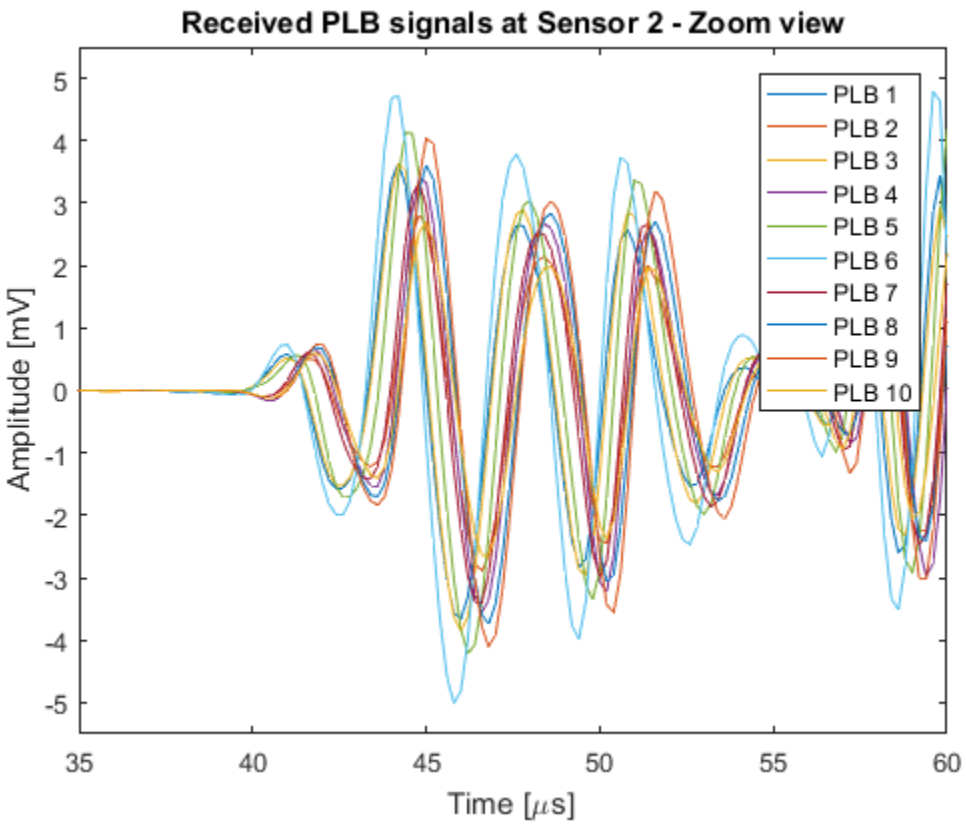

Figure 58 – Zoom in the S_0 mode wave packet

For this reason, averaging those ten experiments produced a partial loss of information. Therefore, it was decided to consider the three most in-phase signals at every sensor and use their average as a reference. This phase represents the second step of the TR process, corresponding to Figure 59 (b). The location of the AE source in this case was known and has been chosen at the center of the plate to simplify the problem for this study. Anyway, the same procedure can be applied even for unknown locations, exploiting the localization algorithm of the Vallen Systeme developed in section 3.4. The signal vectors were normalized to make the results independent with respect to the different sensors sensitivity. With the knowledge of the distance, *r*, from the emitted source, it was possible to rescale the received signals according to Equation (3.4). Successively, they were truncated due to multimode effects (seen in section 5.1), considering only the central guided waveforms, flipped in time and rescaled to take into account the wave attenuation according to Equation (3.4). Finally, the signal is sent back to the PLB source location, given by the localization algorithm (known in this case of study), where now it is positioned at piezoelectric sensor (PZT A) in order to record the arriving time-reversed signal.

Figure 59 clarifies and summarizes the aforementioned technique, which can be considered a hybrid application (experimental-numerical) of the TR process. It is important to emphasize that the forward propagation is purely experimental, while, on the other hand, the backward propagation of the TR method is accomplished through the computational FE method.

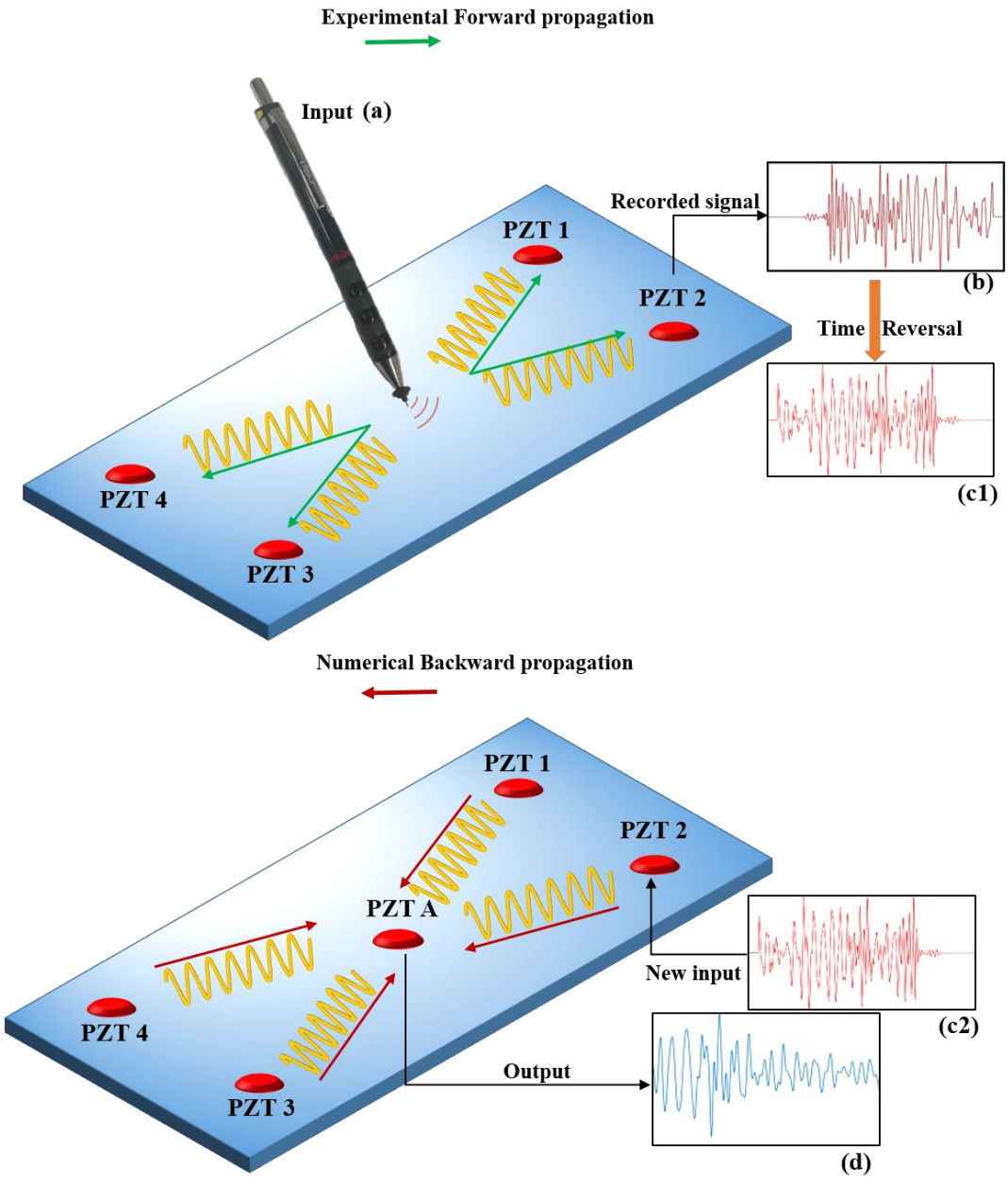

Figure 59 – Hybrid TR process applied to a PLB acoustic emission

6.1.1 The chosen signal window

In the case of a purely numerical TR method, the waveform lengths were known in advance, and chosen by the user. Their length was no longer than 100 μs, allowing to time-reverse the full signal without a prohibitive computational cost. On the other hand, when dealing with the reconstruction of a real PLB signal, the waveform length and shape is unknown. Moreover, the absorbing properties of the plate edges covered with Plasticine, are not ideal, leading to residual unavoidable reflections bouncing back towards the piezoelectric transducers. The recorded signals at the four sensors in the experiment were too long to be completely time-reversed in a numerical simulation. Therefore, the challenge was to find a methodology to cut the signal at the right point, without any loss of information. The last part of the recorded signal could be due to residual reflections interacting between each other or could be really the last part of the PLB.

In literature, there is not any available answer regarding this problem yet. Anyway, several insights related to the length of a PLB signal can be derived looking at simpler waveforms. Referring to Figure 44 in section 4.8.3, it is possible to infer that the length of the S_0 waveform is about 37 μs, while the A_0 wave packet is about 60 μs long. Therefore, for a five cycle Hanning window function with a central frequency of 130 kHz, the ratio, χ, between the length of the A_0 and S_0 waveforms is about:

$$\chi = \frac{A_0}{S_0} \approx \frac{60\ \mu s}{37\ \mu s} \approx 1.62 \tag{6.1}$$

Therefore, assuming an analogous behavior, since also the central frequency of a PLB signal can be considered approximately 130 kHz, the end of the PLB signal can be determined considering the TOA of the A_0 mode, TOA_{A_0}, and adding a time interval equal to the length of the S_0 wave packet, L_{S_0}, multiplied by the previously determined ratio, χ. This translates to the following equation:

$$PLB_{end} = TOA_{A_0} + \chi L_{S_0} \tag{6.2}$$

Figure 58 shows that the L_{S_0} value is about 15 μs, while TOA_{A_0} can be considered around 57 μs. Those evaluations require an expert user and sometimes are arbitrary. The technique developed in section 4.8.2 works with simple waveforms but not with broadband signals where the different frequency components complicate the phase analysis plot. Anyhow, in this case the S_0 was well

separated from the A_0 wave packet, allowing a good evaluation even looking just at the time domain. Applying Equation (6.2) one obtains:

$$PLB_{end} = 57\ \mu s + 1.62 \cdot 15\ \mu s = 81.3\ \mu s$$

Since this method is somehow empirical, without an analytical proof, it was decided to apply a safety factor of 2.5, leading to a time window of about 200 μs. In the following paragraph 6.2, the experimental data will be time-reversed (only the first 200 μs) in the numerical model and, after the application of the transfer function, the PLB signal will be derived.

6.2 RECONSTRUCTED PLB SIGNAL

The Pencil Lead Break signal is derived time reversing the output (d), in Figure 59, and applying subsequently the system transfer function, $G^*(\omega)G(\omega)$, with same methodology used in paragraph 5.4 for the reconstruction of a generic broadband signal. In other words, the obtained result can be considered as the electric potential boundary condition that has to be applied in the upper surface of the piezoelectric actuator in the numerical model in order to produce the same AE generated by a PLB experiment. As a matter of fact, the last sentence simply translates the meaning of Equation (5.7). The result of the reconstructed PLB signal is shown in Figure 60. The light blue line represents the time-reversed version of the output (d), in Figure 59, while the orange colored line symbolizes the same signal but after the application of the system transfer function. Therefore, the "Modified signal" in Figure 60 represents the sought PLB signal.

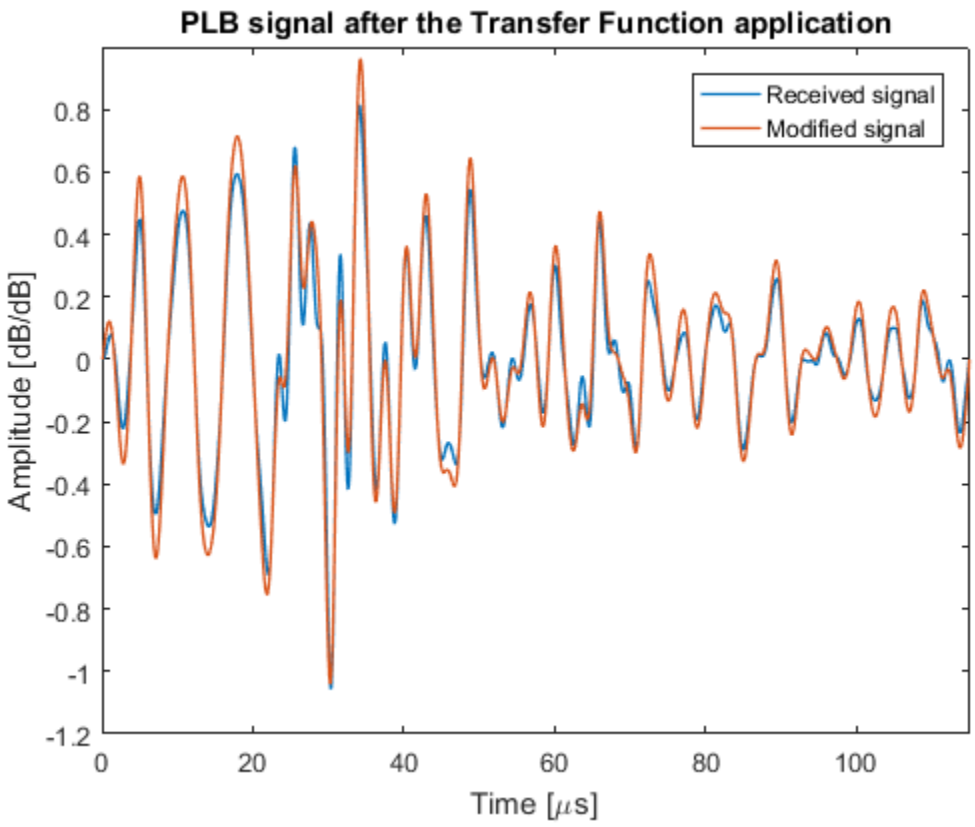

Figure 60 – Comparison between the PLB signal before and after the application of the transfer function

It is curious to notice that the application of the time reversal operator in this case does not change significantly the shape of the presumed "PLB signal", especially if compared with the remarkable improvement obtained applying the transfer function for the reconstruction of the broadband signal in section 5.4. This result could be associated with the fact that most of the energy for a PLB had a main central frequency of 130 kHz for this setup. Hence, the derived PLB acoustic emission is behaving, from a certain point of view, as a narrow band signal. The term $G^*(\omega)G(\omega)$, if the frequency variable, ω, is fixed, becomes close to a constant function and simply scales the received signal without altering its shape.

6.3 COMPARISON WITH INITIAL RECORDED SIGNAL

To proof the consistency of the obtained result, the reconstructed PLB AE has been used as input for another numerical simulation at the central actuator. Then, the results have been compared with

the received signals at the four piezoelectric sensors generated by the real PLB acoustic emission. For the sake of brevity, in Figure 61 it is reported just one of the four possible comparisons. The received signals at PZT 4 are analogous but at the same time, discrepancies are present.

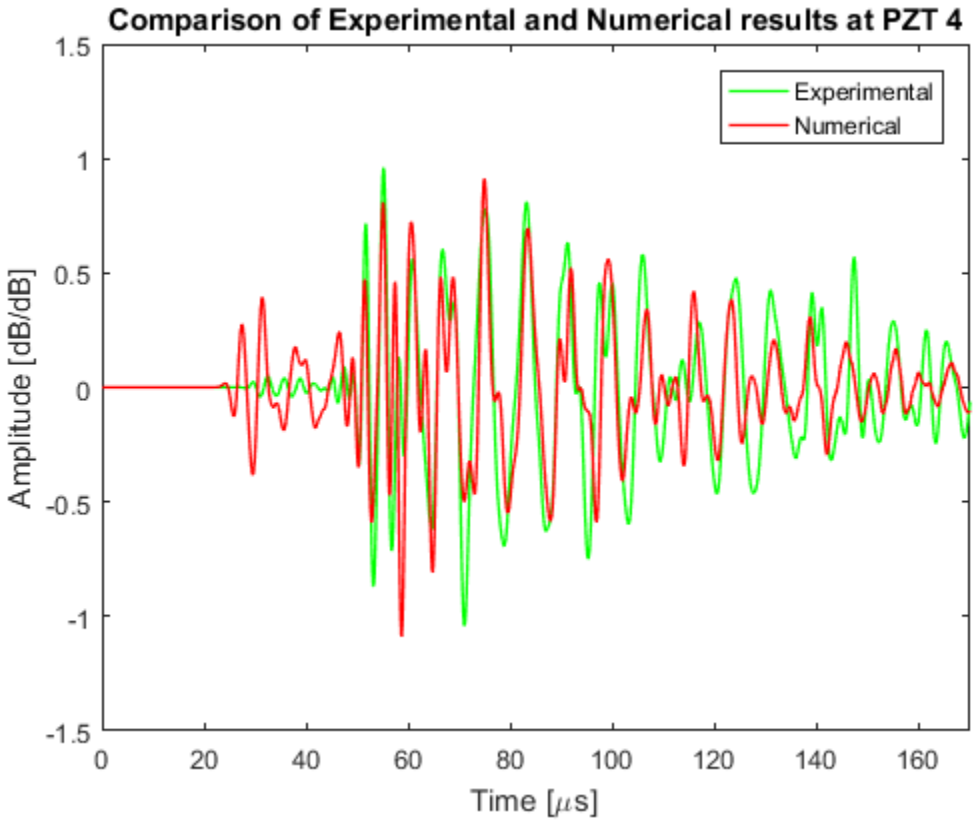

Figure 61 - Received signals at PZT 4: Experimental vs. Numerical

The exponential decay of the A_0 was modeled with acceptable accuracy, demonstrating the effectiveness of the applied Rayleigh damping model discussed in section 4.5, despite of the all the hypothesis made. Moreover, the two signals demonstrate to be in-phase with respect each other. The main difference is related to the S_0 wave packet, much higher in the numerical model than in the experimental results. In Chapter 7, the obtained results are thoroughly discussed and analyzed, leading to conclusions and future research activities to be performed.

CHAPTER 7

7 DISCUSSION AND CONCLUSIONS

Identifying the reason of such discrepancy is challenging and further studies need to be carried out. A possible reason could be associated to the non-perfect modelling of the Lamb wave propagation. Indeed, even a tiny variation could cause a shift in phase causing a badly reconstructed signal at the end of the time reversal process. On the other hand, the successful reconstruction of various broadband signals demonstrates that the proposed methodology is consistent. Indeed, the TR process requires identical conditions in the forward and backward propagations. A purely numerical TR process assures this requirement, even if the model is not perfect. On the contrary, time reversing signals generated by real AE inside the FEM model causes a discrepancy and the applied transfer function is no more the one that represents the interaction between the propagating waves and the structure. Nevertheless, this result is somehow promising, and could be used as a first attempt in the representation of a PLB signal. This opens the possibility to implement the found signal as an input in numerical simulation for the calibration of localization algorithms. So far this has been done just experimentally and this study proposes to approach the same problem from a numerical point of view. On the other hand, this is not the only possible application. Indeed, it was decided to analyze a PLB signal because is a common experiment in the AE community, but also because it can be considered a broadband signal representative of real acoustic emissions. Therefore, being able to reproduce a PLB acoustic emission means being able to reproduce and locate signals generated by different failure mechanisms such as crack growth, delamination and so on. Therefore, the proposed methodology, possibly with the aid of machine learning algorithms, could potentially allow the production of numerically assisted probability of detection curves required by flight authorities for the certification of different kind of aerospace structures.

7.1 FUTURE RESEARCH ACTIVITY

In this research activity, the blue path of the scheme represented in Figure 62 has been followed. Moreover, a hybrid approach (experimental and numerical) was used for the reconstruction of an AE representative of a PLB signal, showing promising results and wide margins for improvement. In future studies, the intention is to follow the green path, associated with an experimental application of the TR method. Therefore, with the same methodology, but this time experimental and not numerical, will be derived the system transfer function, required to apply the TR to a real AE that is typically a broadband signal.

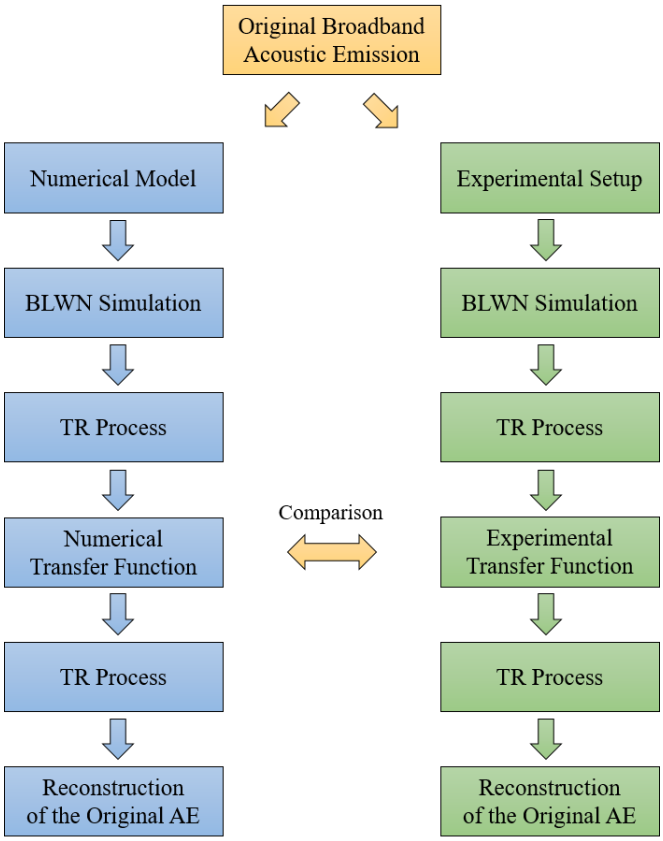

Figure 62 – Current and future methodology

BIBLIOGRAPHY

[1] Charles R. Farrar, Keith Worden, "An introduction to structural health monitoring," *Philosophical Transactions of the Royal Society A Mathematical Physical and Engineering Sciences,* vol. 365, no. 1851, p. 303–315, 2007.

[2] R. Yan, X. Chen, S.C. Mukhopadhyay, Structural Health Monitoring: An Advanced Signal Processing Perspective, Springer, 2017.

[3] Charles R. Farrar, Keith Worden, Structural Health Monitoring: A Machine Learning Perspective, John Wiley & Sons, 2013.

[4] Daniel Balageas, Claus-Peter Fritzen, Alfredo Güemes, Structural Health Monitoring, ISTE, 2006.

[5] FAR Final Rule, Federal Register: October 5, 1978 (Volume 43, Number 194), 14 CFR Part 25 (Docket No. 16280; Amendment No. 25–45).

[6] G. J. McNulty, Quality, Reliability and Maintenance 2004, John Wiley & Sons, 2004.

[7] W. Sikorski, Acoustic Emission Research and Applications, IntechOpen, 2013.

[8] M. Martinez, G. Li, D. Backman, A. Oudovikine, N. Bellinger, "Crack Detection on Composite and Metallic Aerospace Structures," in *4th European Workshop on Structural Health Monitoring*, Cracow, Poland, 2008.

[9] P. Cawley, R. D. Adams, "The Location of Defects in Structures From Measurements of Natural Frequencies," *The Journal of Strain Analysis for Engineering Design,* vol. 14, no. 2, pp. 49-57, 1979.

[10] Wieslaw Ostachowicz, Pawel Kudela, Marek Krawczuk, Arkadiusz Zak, Guided Waves in Structures for SHM: The Time-Domain Spectral Element Method, John Wiley & Sons, 2012.

[11] K. Worden, "Rayleigh and Lamb Waves - Basic Principles," *Strain,* vol. 37, no. 4, pp. 167-172, 2001.

[12] H. Lamb, "On Waves ivn an Elastic Plate," *Proceedings of the Royal Society,* vol. 93, no. 648, 1917.

[13] J. Rose, Ultrasonic Guided Waves in Solid Media, Cambridge University Press, 2014.

[14] C. Sbarufatti, G. Manson, K. Worden, "A numerically-enhanced machine learning approach to damage diagnonis using Lamb wave sensing network," *Journal of Sound and Vibration,* vol. 333, pp. 4499-4525, 2014.

[15] Y. Zhao, F. Li, P. Cao, Y. Liu, J. Zhang, S. Fu, J. Zhang, N. Hu, "Generation mechanism of nonlinear ultrasonic Lamb waves in thin plates with randomly distributed micro-cracks," *Ultrasonics,* vol. 79, pp. 60-67, 2017.

[16] D. W. Greve, J. J. Neumann, J. H. Nieuwenhuis, I. J. Oppenheim, N. L. Tyson, "Use of Lamb waves to monitor plates: experiments and simulations," in *SPIE Smart Structures and Materials + Nondestructive Evaluation and Health Monitoring*, San Diego, California, United States, 2005.

[17] D. Aljets, A. Chong, S. Wilcox, K. Holford, "Acoustic emission source location on large plate-like structures using a local triangular sensor array," *Mechanical Systems and Signal Processing,* vol. 30, p. 91–102, 2012.

[18] Vallen-Systeme GmbH, *AMSY-6 Operation Manual,* Icking: Vallen-Systeme GmbH, 2017.

[19] ASTM E-976, *Standard Guide for Determining the Reproducibility of Acoustic Emission Sensor Response,* ASTM International.

[20] M. Hamstad, "Acoustic emission signals generated by monopole (pencil-lead break) versus dipole sources: finite element modeling and experiments," *Journal of Acoustic Emissions,* vol. 25, pp. 92-106, 2007.

[21] Matthieu Gresil, Victor Giurgiutiu, "Prediction of attenuated guided waves propagation in carbon fiber composites using Rayleigh damping model," *Journal of Intelligent Material Systems and Structures,* vol. 26, no. 16, p. 2151–2169, 2015.

[22] Abaqus CAE User's Guide, "https://www.3ds.com/," [Online].

[23] Vallen Systeme GmbH, "AE–Sensor Data Sheet: VS900-M," [Online]. Available: http://www.vallen.de/?id=118. [Accessed 2018].

[24] M. Martinez, "Finite Element Model of Structures with Piezoelectric Elements," 2006.

[25] Friedrich Moser, Laurence J. Jacobs, Jianmin Qu, "Modeling elastic wave propagation in waveguides with the finite element," *NDT&E International,* vol. 32, pp. 225-234, 1999.

[26] MY Bhuiyan, J Bao, B Poddar and V Giurgiutiu, "Toward identifying crack-length-related resonances in acoustic emission waveforms for structural health monitoring applications," *Structural Health Monitoring,* pp. 1-9, 2017.

[27] M. Gresil, V. Giurgiutiu, Y. Shen and B. Poddar, "Guidelines for Using the Finite Element Method for Modeling Guided Lamb Wave Propagation in SHM Processes," in *6th European Workshop on Structural Health Monitoring*, Dresden, 2012.

[28] Hamstad MA, O'Gallagher A and Gary J, "Modeling of buried monopole and dipole sources of acoustic emission with a finite element technique," *Journal of Acouslic Emission,* vol. 17, p. 97–110, 1999.

[29] Y. Shen, V. Giurgiutiu, "Effective non-reflective boundary for Lamb waves: Theory, finite element implementation, and applications," *Wave Motion,* vol. 58, p. 22–41, 2015.

[30] J. Lysmer, R.L. Kuhlemeyer, "Finite dynamic model for infinite media," *Journal of the Engineering Mechanics Division,* pp. 859-877, 1969.

[31] G.R. Liu, S.S.Q. Jerry, "A non-reflecting boundary for analyzing wave propagation using the !nite element method," *Finite Elements in Analysis and Design,* vol. 39, pp. 403-417, 2003.

[32] S.M.H. Hosseini, S. Duczek, U. Gabbert, "Non-reflecting boundary condition for Lamb wave propagation problems in honeycomb and CFRP plates using dashpot elements," *Composites: Part B,* vol. 54, pp. 1-10, 2013.

[33] P. Rajagopal, M. Drozdz, E.A. Skelton, M.J.S. Lowe, R.V. Craster, "On the use of absorbing layers to simulate the propagation of elastic waves in unbounded isotropic media using commercially available Finite Element packages," *NDT&E International,* vol. 51, pp. 30-40, 2012.

[34] J.R. Pettit, A. Walker, P. Cawley, M.J.S. Lowe, "A Stiffness Reduction Method for efficient absorption of waves at boundaries for use in commercial Finite Element codes," *Ultrasonics,* vol. 54, p. 1868–1879, 2014.

[35] Julius O. Smith III, Mathematics of the Discrete Fourier Transform (DFT) with Audio Applications, BookSurge Publishing, 2007.

[36] T. Bülow, G. Sommer, "A Novel Approach to the 2D Analytic Signal," in *International Conference on Computer Analysis of Images and Patterns*, 2003.

[37] RK Ing, M Fink, "Time-Reversed Lamb Waves," *IEEE Trans. Ultrason. Ferroelectr. Freq. Control,* vol. 45, pp. 1032-1043, 1998.

[38] H Sohn, HW Park, KH Law, CR Farrar, "Combination of a time reversal process and a consecutive outlier analysis for baseline-free damage diagnosis," *J. Intel. Mater. Smart Struct.,* vol. 18, no. 4, p. 335–346, 2007.

[39] CH Wang, JT Rose, FK Chang,, "A Computerized Time-reversal Method for Structural Health Monitoring," in *Proceedings of SPIE Conference on Smart Structures and NDE*, San Diego, CA, USA, 2003.

[40] JT Rose, CH Wang,, "Mindlin plate theory for damage detection I, source solutions," *J. Acoust. Soc. Am.,* vol. 116, no. 1, p. 154–171, 2004.

[41] HW Park, H Sohn, KH Law, CR Farrar, "Time reversal active sensing for health monitoring of a composite plate," *J. Sound and Vibration,* vol. 302, pp. 50-66, 2007.

[42] H.W. Park, S.B. Kim, H. Sohn, "Understanding a time reversal process in Lamb wave propagation," *Wave Motion,* vol. 46, pp. 451-467, 2009.

[43] V. Giurgiutiu, "Lamb Wave Generation with Piezoelectric Wafer Active Sensors for Structural Health Monitoring," in *8th Annual International Symposium on NDE for Health Monitoring and Diagnostics*, San Diego, CA, 2002.

[44] M. Fink, "Time Reversed Acoustics," *Physics Today,* vol. 50, no. 3, pp. 34-40, 1997.

[45] B Xu, V Giurgiutiu, "Single Mode Tuning Effects on Lamb Wave Time Reversal with Piezoelectric Wafer Active Sensors for Structural Health Monitoring," *J. Nondestructive Evaluation,* vol. 26, pp. 123-134, 2007.